Water-Soluble Conjugated Polymers Composites for Chemo-/Biosensing

Hongbo Yuan

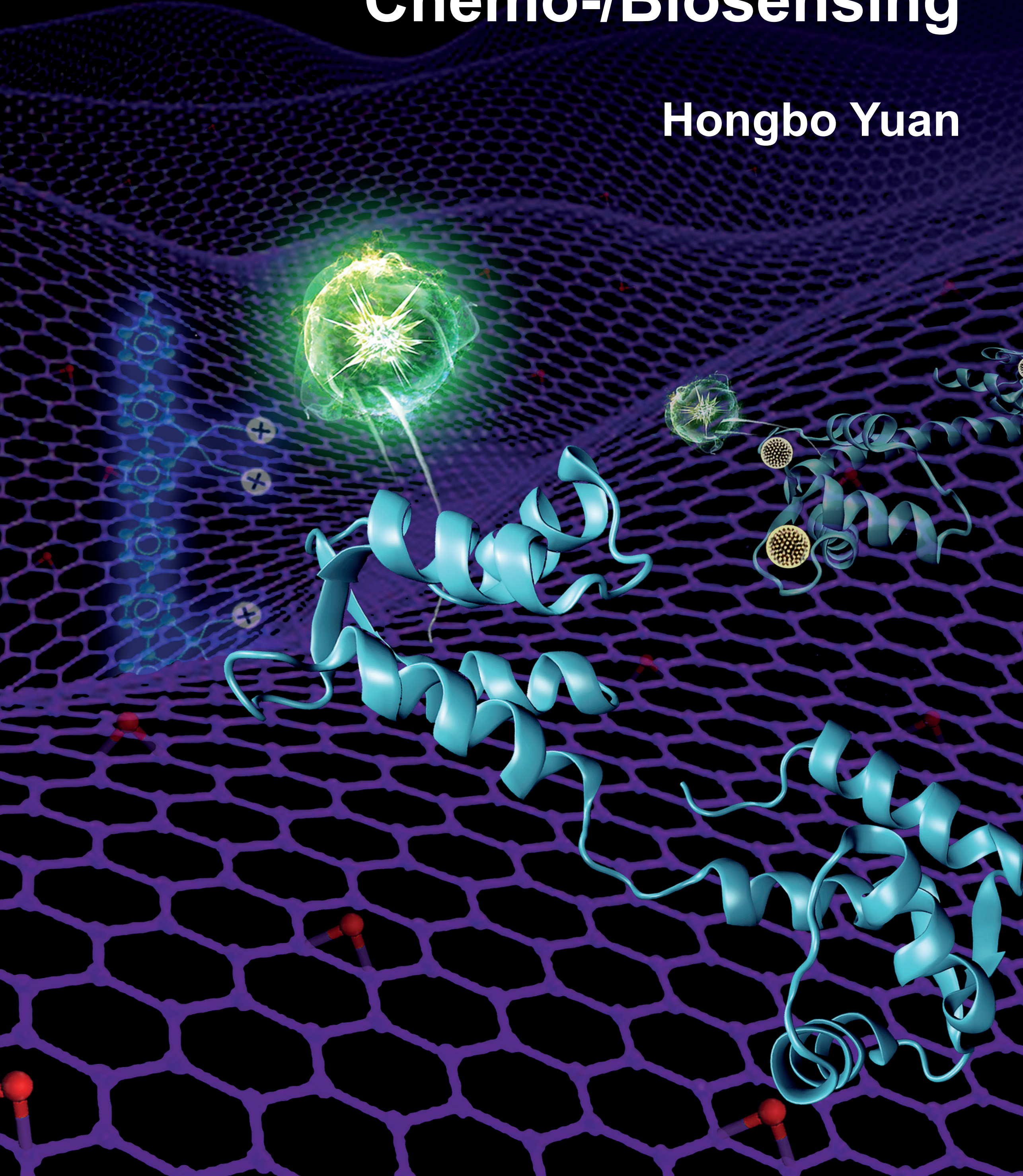

Water-Soluble Conjugated Polymers Composites for Chemo-/Biosensing

Hongbo Yuan

ISBN/EAN 9789462958098

Lay-out and print by: ProefschriftMaken // www.proefschriftmaken.nl

Water-Soluble Conjugated Polymers Composites for Chemo-/Biosensing

Proefschrift

ter verkrijging van de graad van doctor
aan de Radboud Universiteit Nijmegen
op gezag van de rector magnificus prof. dr. J.H.J.M. van Krieken,
volgens besluit van het college van decanen
in het openbaar te verdedigen op maandag 5 februari 2018
om 14.30 uur precies

door
Hongbo Yuan
geboren op 10 juli 1988
Henan, China

Promotoren: Prof. dr. A.E. Rowan
Prof. dr. Y. Zhan (Hebei University of Technology, China)
Prof. dr. C. Xing (Hebei University of Technology, China)

Copromotor: Dr. P.H.J. Kouwer

Manuscriptcommissie:
Prof. dr. R.J.M. Nolte
Prof. dr. J. Hofkens (KU Leuven, België)
Prof. dr. J. Qing (Hebei University of Technology, China)

Paranimfen:
Kaizheng Liu
Paula de Almeida

Table of Contents

Abstract

Owing to the large π-conjugated polymer backbones, delocalized electronic structure and good compatibility with aqueous environments, water-soluble conjugated polymers (WCPs) have been extensively applied in chemo- and biosensing, imaging, diseases diagnosis and therapy. The objective of this thesis is to fabricate composite materials based on WCPs and to study their properties and applications in sensory technologies.

Chapter 2 discusses a simple, label-free and highly sensitive strategy for the visualized detection of conformational changes of calmodulin bound to target peptide (CaM-M13) based on the flexible polymer backbone of the water-soluble conjugated polythiophene derivative (PMNT). The conformational changes of CaM-M13 from the closed to the compact form upon binding with Ca^{2+} are visual with naked-eye by turbidity changes of the samples and by color changes of the fluorescence of the aqueous medium. The detection limit of CaM is as low as to 6.16 pmol. Due to the specific binding of Ca^{2+}, the assembly of PMNT/CaM-M13 can be used for sensing calcium as well. This platform, however, only works for the hybrid CaM-M13 protein, and also exhibits a high background signal arising from nonspecific interactions.

In order to solve the problems of Chapter 2, we designed a FRET-based hybrid probe comprising graphene oxide (GO) and the cationic conjugated poly(fluorene-*co*-phenylene) (PFP) in **Chapter 3**. The conformational changes of CaM are quantitatively monitored through the FRET ratio between PFP and the enhanced green fluorescent protein (EGFP) labeled at the N-terminus of CaM. Upon Ca^{2+}-binding, CaM/Ca^{2+} tightly interacts with GO through strong hydrophobic effects and weak electrostatic repulsion, resulting in an increased distance between PFP and EGFP, thus a much weaker FRET efficiency. Importantly, this platform can be applied not only for calmodulin but also for calmodulin binding to target peptides, which imitate the transformation *in vivo*.

In **Chapter 4**, a CO_2 responsive system is presented based on a guanidinium-pendent oligofluorene (G-OF) and a carboxylate functionalized polythiophene (PTP). This system can be applied for the “turn on” detection of CO_2 with low background signal employing the efficient fluorescence quenching of the tight aggregate of G-OF/PTP. Upon exposure to CO_2, the electrostatic repulsion between G-OF and PTP is enhanced through protonation of the side chains, leading to disaggregation and, thus, the “turn-on” of fluorescence. Moreover, the system is so sensitive that it can be effectively used to monitor the concentration changes of CO_2 in the process of plant photosynthesis.

Chapter 5 describes another CO_2-responsive material based on the signal amplification property of a polythiophene derivative (PTP) and the catalytic activity of carbonic anhydrase (CA). The self-assembly of PTP that is dominated by electrostatic and hydrophobic interactions which are triggered by CO_2, and accelerated by CA that highly efficiently inter-converts CO_2 and HCO_3^-. Furthermore, PTP/Ca^{2+} complexes are formed based on the coordination between the side chains of PTP and Ca^{2+} ions, which are employed for biomimetic CO$_2$ sequestration with fluorescence monitoring in the presence of CA.

In **Chapter 6**, we report a method to delicately tune the conformation of a polythiophene derivative (PMNT) using the helical structure of polyisocyanopeptides (PIC). PIC serves as a scaffold to trap and stretch PMNT into a highly planar and nano-aggregate conformation, resulting in a significant red shift in both UV-vis and fluorescence spectra. Interestingly, the degree of conformational change of PMNT is easily tuned by the length of PIC. The poorly defined extremities of PIC play a crucial role in the assembly, which is experimentally supported by partly denatured long PIC polymer. Considering the good biocompatibility and thermal responsive gelation properties of PIC, the PMNT/PIC hybrid material provides promising opportunities for applications in both semiconductor and biosensor fields.

Keywords: Water-soluble conjugated polymers (WCPs), Chemo-/Biosensing, Carbon dioxide (CO$_2$), Protein and macromolecular conformations

CHAPTER 1

INTRODUCTION: WATER-SOLUBLE CONJUGATED POLYMERS FOR SENSING APPLICATONS

1.1 General introduction

Conjugated polymers (CPs) are an important class of sensing and electronic materials. They display excellent light harvesting, signal amplification and tunable optoelectronic properties, which originate from the long π-electron delocalized polymer backbone.[1–4] In addition, the solubility and functionalization of CPs are easily tailored through the modifiable side chain.[5] With their low production costs and easy of processibility, CPs have been developed as ideal materials for miscellaneous emerging technologies, for example, photovoltaic devices,[6,7] light-emitting diodes (LEDs),[1] field-effect transistors (FETs),[8] detection both of chemical and biological molecules,[9,10] and disease diagnosis & therapy,[11] etc.

In this tutorial review, we mainly focus on the extensive bioapplicantions of water-soluble conjugated polymers (WCPs) which are synthesized by decorating the side chains with negatively or positively charged moieties.[12] Specific recognition moieties such as antibodies or receptors further aid in excellent biocompatibility.[13] WCPs are able to selectively recognize both of small chemical molecules (CO_2, Hg^{2+}, NO, etc.) and biomacromolecules (DNA, RNA, proteins, etc.) through intensively noncovalent interactions based on electrostatic attraction, π-π stacking, van der Waals forces, and hydrophobic effects.[14–19] Such recognition events result in changes in chain conformation of WCPs, which in turn give rise to changes in photophysical property.[20,21] WCPs-based sensors are very sensitive to minor perturbations, taking advantage of amplification by a collective response, which provides strengths when compared with small molecule counterparts.[9] In addition, WCPs have been widely used in the Förster resonance energy transfer (FRET) approaches. For example, Bazan and co-authors demonstrated that a simple and highly sensitive assay with a 25-fold higher optical amplification than that measured by commercial dye and 10 pM of detection limit for the sensing of fluorescently labeled DNA.[4] Wang's group designed a multistep FRET platform used for quantitative analysis of DNA methylation levels of seven colon cancer-related genes on the basis of energy transfer between WCPs and different fluorescent dyes.[22] Moreover, cell imaging based on WCPs is an important technique in understanding the function and mechanism of target biological species in cells.[23,24] Beyond sensing, it is found that WCPs could produce singlet oxygen ($^1O_2$) under the stimulation of light.[25–27] This property initiates a new application of WCPs in photodynamic antimicrobial chemotherapy (PACT), especially with the increasing antibiotic resistance of cells.[28,29] We will discuss the advances and design principles in sensing from small molecules to biomacromolecules, detection of bacteria and antimicrobial applications of WCPs.

1.2 Detection of gas molecules and metal ions

Sensory technologies have been drawing much attention in the entire human history. Chemosensors based on the changing of photophysical properties such as color, absorbance or fluorescence spectra are very useful and cost-effective tools for detection of various analytes.[30,31] A typical optical chemosensor recognizes a specific substrate, and amplifies the signal as much as possible. Compared to small molecule counterparts, WCPs combine the action of a great many repeat units with efficient energy and/or electron migration mechanisms.[9] As shown in **Figure 1.1**, upon binding with one quencher, the whole polymer backbone is quenched resulting in the desired amplification effect.[32]

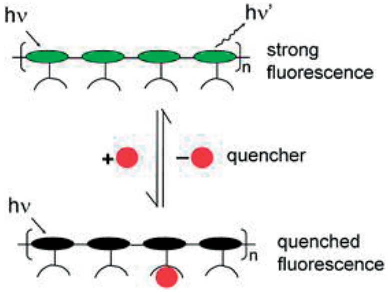

Figure 1.1. Amplified fluorescent quenching mechanism of water-soluble conjugated polymers by quenchers. Reproduced with permission.[32] Copyright 2010, Royal Society of Chemistry.

1.2.1 Gas molecule detection

The atmosphere of earth is indispensable and closely related to human health. Therefore, it is important to effectively monitor the components of air, especially for toxic constituents. Carbon dioxide (CO_2) is a trace gas which naturally distributes in the earth atmosphere and plays a significant role in the *carbon cycle*.[33] Its constantly increasing concentration as a result of fosil fuel consumption contributes immeasurably to the "greenhouse effect" and the acceleration of global warming.[34,35] Moreover, CO_2 can lead to asphyxiation when its concentration is higher than normal level. The maximum acceptable concentration has been defined between 0.5 and 3.5 %.[36] Therefore, the ability to detect the concentration of CO_2 sensitively and timely, is imperative both for human health and environmental protection. In 2013, Yoon's group developed a colorimetric and fluorescent "turn-on" carbon dioxide (CO_2) sensor based on the polydiacetylene (PDA-1, **Figure 1.2**), which was grafted with amines and imidazolium cations as CO_2 stimuli-responsive groups.[37] CO_2 reacts with alkylamines group to generate carbamic acid salts with negative charges. In the presence of triethylamine (TEA, 0.5 % v/v), carbamic acid salts partially neutralize the polymer's positive charges of imidazolium, resulting in conformational changes of polymer backbone due to a change in solvation of the side chains. The blue to red color change is readily observable by naked eye.

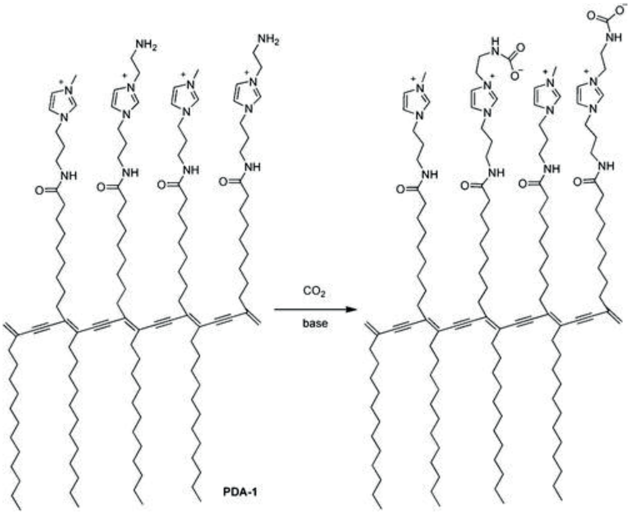

Figure 1.2. Structure of PDA-1, and the proposed origin of the CO$_2$-induced color change. Base: triethylamine. Reproduced with permission.[37] Copyright 2013, American Chemical Society.

Recently, *in situ* detection has attracted much attention due to the ability of sensing the original state of events in real-time, which is vital for detecting or even preventing accidents.[38–40] In 2017, Xing and co-authors designed a water-soluble conjugated polymer (PFBT) based on fluorene and 2,1,3-benzothia-diazole for sensing CO$_2$ *in situ* with high sensitivity and low background.[41] As shown in **Figure 1.3**, the side chains of PFBT contains two amino and four negatively charged carboxylate groups, resulting in good dispersion in aqueous solution. Due to the two different contents in repeat units, PFBT would display different photophysical properties when the energy transfers from fluorene units to 2,1,3-benzothia-diazole (BT) units. Upon introducing CO$_2$, the carboxylate and amino groups are gradually protonated, and the electrostatic repulsion between the polymers become weaker, At same point, hydrophobic interactions intensively dominate the PFBT polymers and form aggregations, resulting in an emission color shift from blue to green. Importantly, the detect limit of PFBT-based sensor can be lowered to ~400 ppm by measuring the fluorescence spectra. Moreover, PFBT films made by spraying PFBT onto a cellulose ester membrane, demonstrated a similar behavior as towards CO$_2$. As a pratical application, PFBT was used as a chemosensor to detect variation of CO$_2$ concentrations in real time caused by plants in greenhouse and monitor the plant photosynthesis and respiration upon cycling day and night *in situ*. Clear changes of CO$_2$ levels in a greenhouse were observed in time, by measuring the ratios between the emission intensity at 538 and 414 nm (I_{538} nm/I_{414} nm) which are assigned to the BT and fluorene units of the PFBT backbone, respectively (Figure 1.3c,d). In comparison to traditional analytical methodologies such as gas chromatography/mass spectrometry,[42,43] near-infrared spectroscopy[44]

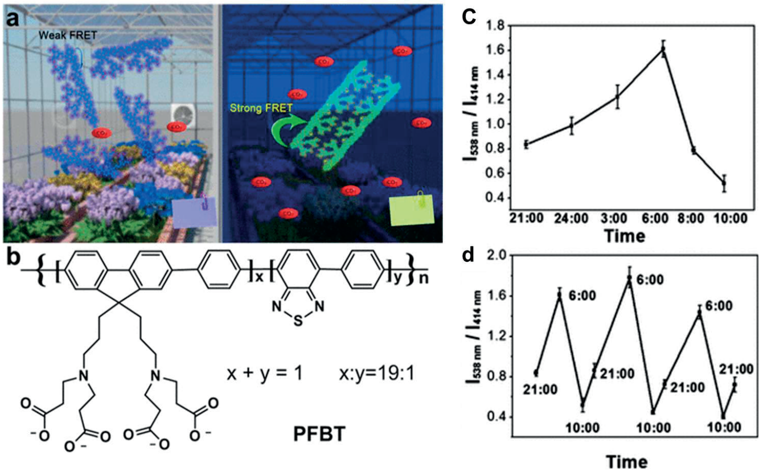

Figure 1.3. (a) Schematic representation of PFBT-based strategy for CO_2 detection in plant photosynthesis and respiration process upon cycling day and night *in situ*; (b) Chemical structure of PFBT. Emission intensity ratio of the emission intensity at 538 and 414 nm (I_{538} nm/I_{414} nm) of PFBT measured at different times in the greenhouse from 21:00 to 10:00 during 1 day and night (c), and 3 days and nights (d). Reproduced with permission.[41] Copyright 2017, American Chemical Society.

and electrochemical techniques,[45] these chemical sensors based on conjugated polymers showed some advantages including convenience, low cost, and a fast response.

Generally, sensing is based on the chemical reaction or physical bonding between the side chains of CPs and analytes.[9,46,47] However, some molecules are too inert to react with any groups in normal conditions. Inspired by nature, a second essential cofactor is introduced as an intermediate to transfer the signals from analytes to CPs. Swager and co-authors designed a ethylene sensor based on poly(phenylene ethynylene)s (PPEs) by using a copper(I) complex mimicking the mechanism of ethylene binding in plants.[48] As illustrated in **Figure 1.4** I, the triple bonds of PPEs backbone served as coordination sites for copper(I) alkyne complexes which leads to a fluorescence quenching. The fluorescence of PPEs recovers when the copper complexes bind to ethylene gas. Importantly, the detection limit can be as low as 1000 ppm in thin films which allows for monitoring the ripening of fruits and vegetables to prevent ethylene sensitive agricultural products from deterioration.

In addition, the Wang group developed a conjugated polymer/Cu^{2+} coordination complex to measure nitric oxide (NO) which is an endothelium derived relaxing factor.[49] The conjugated polyfluorene polymers are functionalized with imidazole moieties (CCP1) which served as coordination sites for Cu^{2+} ions (Figure 1.4 II). The fluorescence of CCP1 is efficiently quenched by the paramagnetic Cu^{2+} (good quencher) due to the weak N⋯Cu interactions (turn off). However, the paramagnetic Cu^{2+} ions reduce to a diamagnetic Cu^{1+}

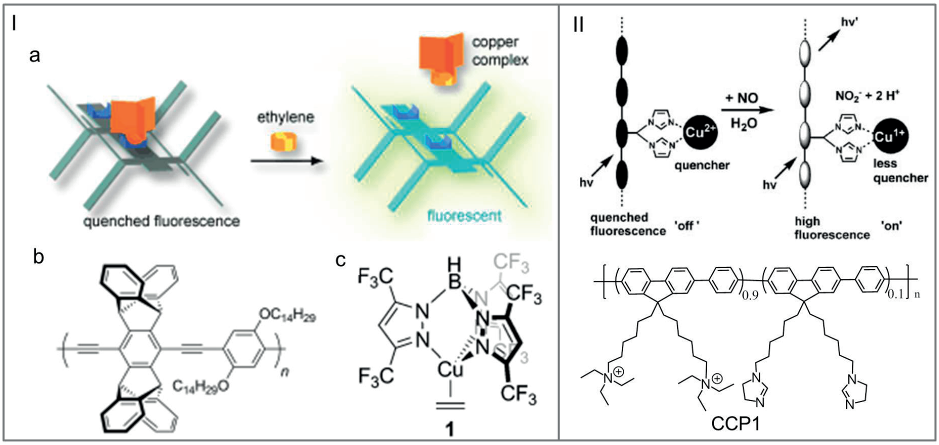

Figure 1.4. I: (a) Design of a sensory system for the detection of ethylene gas. (b) Chemical structure of poly(*p*-phenylene ethynylene)s with pentiptycene units (PPEs). (c) Complex of copper(I), a fluorinated tris(pyrazolyl)borate ligand, and ethylene employed in the sensory system. Reproduced with permission.[48] Copyright 2010, Wiley-VCH. II: Schematic representation of the NO sensor based on the fluorescence turn-on of the CCP1, and the chemical structure of CCP1. Reproduced with permission.[49] Copyright 2007, Wiley-VCH.

ions (weak quencher) induced by NO.[50] As a result, the fluorescence of polymer is significantly recovered (turn on). In short, the combination with a cofactor not only enhances the selectivity of conjugated polymers but also expands their range of applications.

1.2.2 Metal ion detection

One of the major sources of water pollution is metal ions that are discharged by industry. The accumulation of metal ions seriously affects the entire biosphere from individual species to entire ecosystems. Consequently, the detection of metal ions in water has received growing attentions because of their fatal toxicity and impact on public health.

To date, numerous sensors based on CPs for various ions have been developed. They can be categorized in three different principle design approaches. In the first approach, the responsible receptor for metal ions is located at the side chain of conjugated polymer. These sensors demonstrate an “off–on” colorimetric response when recognition events occur.[51,52] Xing’s group designed a conjugated polythiophene (PTT, **Figure 1.5**), functionalized with thymidine side chains, analogous to DNA, but now with polythiophene backbone replacing the phosphate bonds.[53] Upon introducing Cu^{2+}, PTT assembles with the Cu^{2+} ions and forms large complexes due to the specific coordination interaction between the thymidine side chain and Cu^{2+}. As a consequence, the 3d orbital of Cu^{2+} ions capture an electron from the π^* orbital of PTT in the excited state, which induces the efficient fluorescence quenching of the PTT backbones. Analogously, a series of receptors have been developed for different ions, for instance, a thiazole-containing poly(1,4-bis-(8-(4-phenylthiazole-2-thiol)-octyloxy)-benzene) (PPT, Figure 1.5) was synthesized and used to detect both iodide (I^-) and mercury (Hg^{2+}) ions in aqueous solution;[54] triazole moieties were introduced by click chemistry for Hg^{2+} ion detection;[55,56] cooperative receptors combining benzochalcogendiazole with triazole (P1 and P2, Figure 1.5) were used for nickel ion (Ni^{2+}) sensing.[57] Although these sensors are selective and rapid, the fluorescence of conjugated polymers is quenched by metal ions in most cases, which is not intuitively accepted by users and increases the probability of negative results.

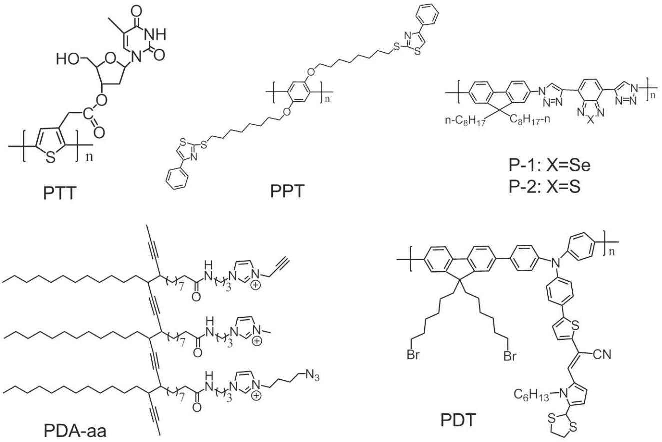

Figure 1.5. Chemical structures of PTT, PPT, *P*-1, *P*-2, PDA-aa and PDT.

In the second approach, the metal ion acts as a catalyst for a reaction that causes a conformational change in WCPs. Yoon and co-authors described a polydiacetylene (PDA-aa, Figure 1.5) grafted with azide and alkyne as reactive groups that forms vesicles in water.[58] The bivalent Cu^{2+} ions reduce to monovalent Cu^+ ions in the presence of ascorbic acid. Interestingly, the Cu^+ ions then catalyze the conjugation between azide and alkyne groups, resulting in a color transition from blue to red on account of the conformational change of the polydiacetylene backbone. Li's group reported a “turn on” mercury probe (PDT, Figure 1.5) that takes advantage of the deprotection reaction of dithioacetals promoted by Hg^{2+} ions.[59] The mercaptal groups on side chains readily convert into aldehyde groups once induced by Hg^{2+} resulting in a strong fluorescence. In comparison with the first approach, reaction-based method usually exhibits higher selectivity.

The third approach is the DNA or protein aptamer based sensor.[60] Mercury-specific oligonucleotide (MSO) contains a large number of thymine bases (T) and easily forms T–Hg^{2+}–T complexes with mercury ions in a stem-loop structure. Employing the flexible conformation of conjugated polythiophene, Wang and co-authors designed a simple “mix-and-detect”

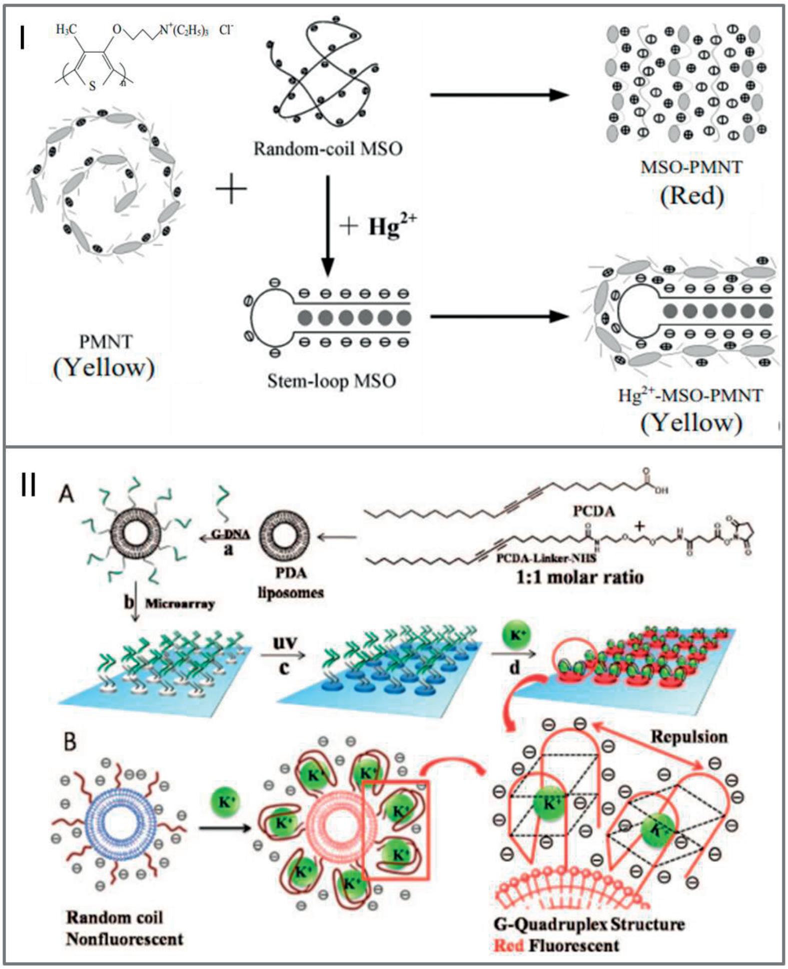

Figure 1.6. I: Schematic illustration of the optical mercury sensing mechanism based on MSO and positively charged PMNT. Reproduced with permission.[61] Copyright 2007, Wiley-VCH. II: (A) Fabrication of the PDA liposome grafted with G-rich ssDNA on surface. (B) Schematic representation of the G-quadruplex formation and the resulting steric repulsion. Reproduced with permission.[63] Copyright 2008, American Chemical Society.

platform for Hg^{2+} detection combining poly(3-(3'-*N*,*N*,*N*-triethylammonium-1'-propyloxy)-4-methyl-2,5-thiophene chloride) (PMNT) with MSO.[61] The DNA is able to impart its structure to the polythiophene backbone leading to changes in optical properties (**Figure 1.6** I). In the same way, lead ions (Pb^{2+}) are well detected using a specific sequence oligonucleotide (TBAA), which exhibits a G-quadruplex structure when assembled with Pb^{2+} ions.[62] In addition, Kim and co-authors constructed a PDA liposome for potassium (K^+) detection with very high selectivity even in the presence of Na^+.[63] As shown in Figure 1.6

II, the surface of the PDA liposome is decorated with G-rich sequence as a selective probe for K^+ ions. After introducing K^+ ions, a G-quadruplex structure is induced through intramolecular hydrogen bonding. Meanwhile, a clear color change from blue to red is observed as a result of the perturbation of the backbone of PDA induced by the steric repulsion of the bulky G-quadruplexes. In addition, the authors developed a PDA liposome microarray used for quantitative analysis of the K^+ concentration. Due to good selectivity, mild conditions and biocompatibility, these methods have promising applications in biology.

1.3 Detection of biomacromolecules

Identification and quantification of specific biomolecules are an important task in both medical and clinical research, because most of diseases have their own specific characters called "biomarker".[64,65] Traditional methods used in the clinic include electrochemistry, flow cytometry, polymerase chain reaction (PCR), and enzyme-linked immunosorbent assays (ELISA).[66] Many of them, however, require expensive instruments, sophisticated procedures and experienced users, which limit their applications. Recently, water-soluble conjugated polymers (WCPs) have been quite extensively used for biomolecule detection employing the good solubility, biocompatibility and excellent signal amplifications.[11,67]

1.3.1 Nucleic acid, DNA methylation and mutation detection

Heeger and Bazan *et al.* pioneered a platform for DNA detection based on a fluorescein (Fl) tagged peptide nucleic acid (PNA) probe (PNA-Fl) and Förster energy transfer (FRET) technique.[4,20] Leclerc and co-authors developed a conjugated polythiophene sensor for DNA without any labels; it is based on different electrostatic interactions and conformational structures between the flexible polythiophene backbone and ssDNA or dsDNA.[21,68] In addition, some hybrid conjugated polymer materials for DNA detection are reported to increase the signal to noise ratio, for example, grapheme oxide (GO) is commonly employed as a quencher due to its efficient fluorescence quenching effect.[69,70] After a few years of development, Huang's group elaborately reviewed DNA detection approaches based on conjugated polymers.[71] In brief, the main mechanisms used in these methods are classified along two lines: (1) FRET-based techniques between various cationic polyfluorene, polyarylene or polythiophene derivatives and a chromophore labeled DNA; (2) conformational changes of conjugated polymers induced by the specific structure of DNA, often cationic polythiophene derivatives are used due to their flexible backbone.

Not only the DNA sequence carries a tremendous amount of biological information, also the subtle decorations of DNA such as DNA methylation changes and mutations are crucial. The Wang group designed a pattern to cumulatively detect multiple changes of epigenetic methylation markers occurring in colon cancer, based on the combination of

PCR amplification with FRET.[22] As shown in **Figure 1.7** I, the extracted genomic DNA from tumor cells is divided into two parallel fractions. One is treated with restriction endonuclease *Hpa*II which is able to exclusively digest the non-methylated DNA due to the specific recognition on CCGG site; while the other fraction remains without treatment. Next, the undigested DNA is amplified by fluorescein-labelled dNTPs (Fl-dNTPs). Upon addition of cationic conjugated polymers (CCPs), a strong FRET signal transfers from CCPs to Fl-dNTPs which are incorporated into the DNA sequence by PCR. In contrast, there is no any FRET signal from the unmethylated DNAs digested by *Hpa*II. Finally, the methylation level, expressed as the *E-value*, is evaluated according to FRET ratios ($I_{530\ nm}/I_{424\ nm}$) with and without *Hpa*II, and the blank control samples, respectively. Based on this platform, the authors obtained both high sensitivity and accuracy for colon cancer detection (86.7 and 86.3 %) and for differential diagnosis (94 and 97.5 %), which are much higher than those determined by the single methylation detection method (41.7–65 %). Therefore, the methylation sensor based on conjugated polymers holds great promise for early detection and differential diagnosis of cancer with high sensitivity and cost effectiveness.

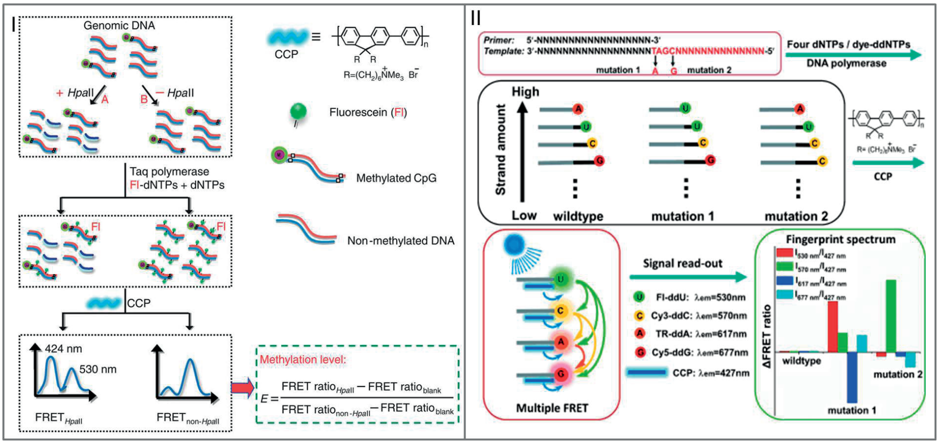

Figure 1.7. I: Schematic representation of the DNA methylation detection using PCR amplification and CCP-based FRET. *Hpa*II was used to digest the non-methylated DNA. Reproduced with permission.[22] Copyright 2012, Nature Publishing Group. II: Schematic representation of multiplex DNA mutations detection based on the FRET fingerprint technique (FFS). Reproduced with permission.[72] Copyright 2013, Wiley-VCH.

Studying and diagnosing gene mutations have attracted much attention in recent years due to the accuracy and predictability.[73] For instance, multiplex mutations in the PIK3CA (E542K, E545K, H1047R and H1047L) exhibit a high possibility in various cancers such as 27 % of glioblastomas, 25 % of gastric cancers, 8 % of breast cancers, and 4 % of lung cancers.[74] Notably, the same group developed a platform for multiplex DNA mutations detection by using a FRET fingerprint spectrum (FFS) assay based on CCPs.[72] As illustrated in Figure 1.7 II, the PCR reaction is promoted by a primer and terminated by four different dye-labeled ddNTPs (TexRed for ddATP, fluorescein for ddUTP, Cy5 for ddGTP, and Cy3 for ddCTP, respectively). However, comparing with the traditional dideoxy sequencing reaction, the concentrations of four different dye-labeled ddNTPs are much higher than the dNTPs. So, the PCR reaction prefers to stop early resulting in a high probability of short DNA sequences. For wild types, the reactions are most likely terminated by TR-ddATP; the probolity decreases with: TR-ddATP > Fl-ddUTP > Cy3-ddCTP > Cy5-ddGTP. For mutation 1, the highest possibility of DNA is terminated by Fl-ddUTP. For mutation 2, however, the Cy5-labeled DNA is replaced by Cy3-ddCTP leading to an increasing amount of Cy3. Interestingly, CCPs and the four dyes act acceptor and donor for each other and form a multistep FRET according to their absorption and emission spectra. As a consequence, the FRET fingerprint spectrum (FFS) is described by collecting and analyzing the multistep FRET spectra. Importantly, this ingenious strategy has been successfully used to analyze the multiplex mutations of both the *PIK3CA* and *KRAS* genes.

1.3.2 Protein and conformational changes of protein detection

In comparison to DNA, proteins exhibit more complicated and well-organized three-dimensional structure. Therefore, biology-based specific recognition interactions are often introduced into the detection system of the protein. As a representative example, Ho and Leclerc successfully employed a DNA aptamer (5'-GGTTGGTGTGGTTGG-3') to detect human α-thrombin based on a specific recognition event between them.[75] In the presence of thrombin, the conformation of the aptamer transform into a compact G-quadruplex structure. In this conformation, a cationic polythiophene assembles with the aptamer/thrombin complex resulting in a good dispersion and an orange color (path A in **Figure 1.8** I). However, if the protein is nonspecific such as bovine serum albumin (BSA), or the aptamer is the wrong sequence, the backbone of the polythiophene will be planarized by the single strand DNA, leading to a significant red-shift (path B in Figure 1.8 I). Notably, this assay is simple, rapid, selective and sensitive with a detection limit of 2×10^{-15} mol. Huang *et al.* further developed this strategy by using a dye-labeled split aptamer and FRET technique.[76] Compared to an intact aptamer, the split aptamers are composed of two or more DNA fragments, which endows the system with an increasing possibilities for G-quadruplex formation upon binding with thrombin.[77] A water-soluble cationic conjugated polymer (PFEP) was employed as energy donor in this system. In the absence of thrombin, a significant FRET between PFEP and dye-labeled DNA is observed due to the formation of PFEP/DNA complexes by strong electrostatic interactions. The two split aptamer fragments efficiently fold into G-quadruplex in presence of thrombin, and consequently, FRET is blocked by G-quadruplex/thrombin complex because of the large size of thrombin (Figure 1.8 II). Beyond DNA aptamers, antigen–antibody binding is a universal recognition event in biology. Thus, much effort has been devoted to explore a sensing strategy based on protein-specific signals, especially in a label-free manner. Wang *et al.* reported an optical nano-ruler for sensing proteins, utilizing the distance-dependent metal-enhanced fluorescence (MEF) effect controlled by antigen–antibody binding.[78] As shown in Figure 1.8 III, silver nanoprisms (Ag NPRs) are coated on quartz slides as metal magnifying nanostructures. Next, an interlayer film composed of polyethyleneimine (PEI) and poly(acrylic acid) (PAA) is employed to conjugate with antibodies. The MEF effect between the Ag NPRs and the conjugated polymer ((poly[9,9′-bis(6,6′-(*N*,*N*,*N*-trimethylammonium)fluorene-2,7-ylenevinylene-*co*-alt-2,5-dicyano-1,4-phenylene] (PFVCN) used in this work), is tuned by antigen–antibody recognition events.

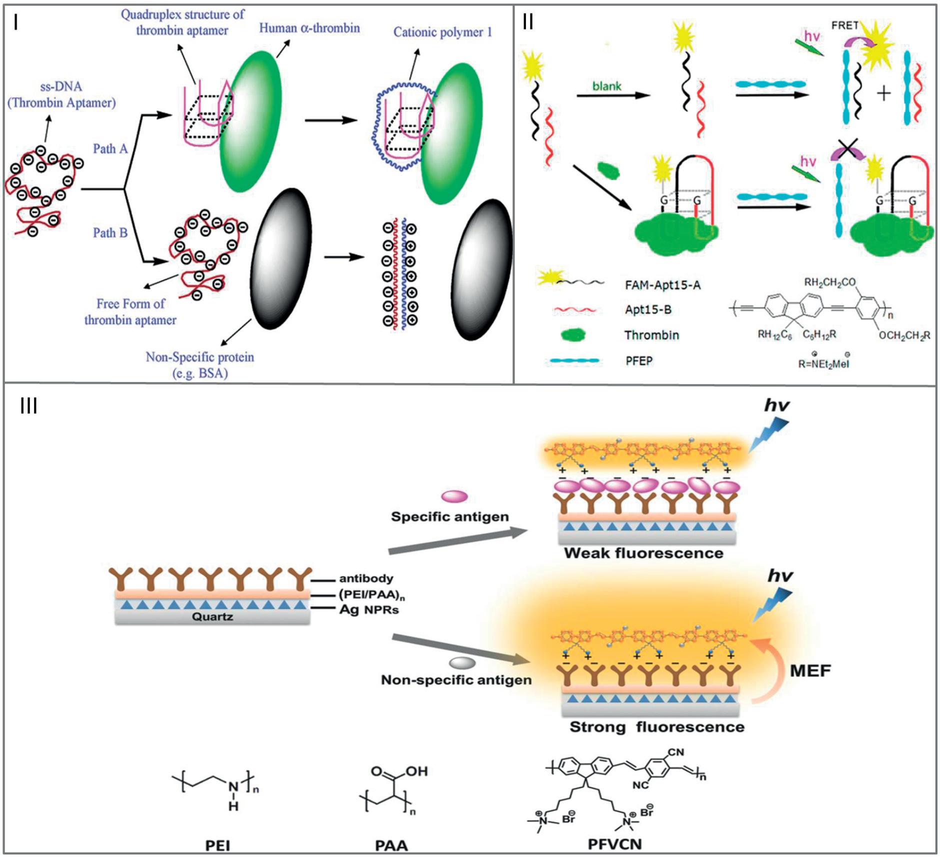

Figure 1.8. I: Scheme of human α-thrombin detection based on the intact aptamer and the conformational changes of cationic polythiophene. Reproduced with permission.[75] Copyright 2004, American Chemical Society. II: Schematic description of thrombin detection using split aptamer fragments and PFEP, and chemical structure of PFEP. Reproduced with permission.[76] Copyright 2014, American Chemical Society. III: The construction of protein nano-ruler based on antigen–antibody binding and MEF effect. Reproduced with permission.[78] Copyright 2015, Wiley-VCH.

Taking the catalytic activity of enzymes into consideration, Tang's group reported a biosensor for adenosine deaminase (ADA) detection.[79] In this platform, as shown in **Figure 1.9** I, ADA catalyzes the adenosine to inosine reaction, leading to the formation of double-stranded DNA (dsDNA) between the aptamer and DNAc-FI. Afterwards, the ethidium bromide (EB) is able to insert into the dsDNA. Upon excitation of the energy donor PFP, a multistep FRET from PFP to EB via FI is constructed, giving rise to the strong fluorescence of EB. In the absence of ADA, however, the energy could only impart to FI because the dsDNA structure is inhibited by the adenosine which promotes the complementary aptamer to form a hairpin-like conformation. In addition, Xia *et al.* synthesized a bipolar beacon (CP-c-DNA) that is comprised of a hydrophobic conjugated polymer (CP) backbone and a hydrophilic DNA tail.[80] In aqueous solution, the bipolar polymers form micelles with a hydrophilic DNA shell and a hydrophobic CP core resulting in the fluorescence quenching of the CP (off state). Interestingly, the hydrophilic properties of the bipolar polymer are remarkably changed by the length of DNA tails. Upon addition of telomerase, the bipolar probe micelles disassemble and liberate the fluorescence (on state) due to the DNA elongation reaction (yellow part, Figure 1.9 II). Moreover, these catalyzed activity based strategies could be used to determine enzyme activity as well.[81]

Generally, the recognition events used in protein detection include a DNA-based aptamer, antigen–antibody binding or enzymatic reaction. All of these events trigger the optical changes of conjugated polymers taking advantages of conformational change of polymer backbone, quenching of fluorescence, FRET technique or similar effects.

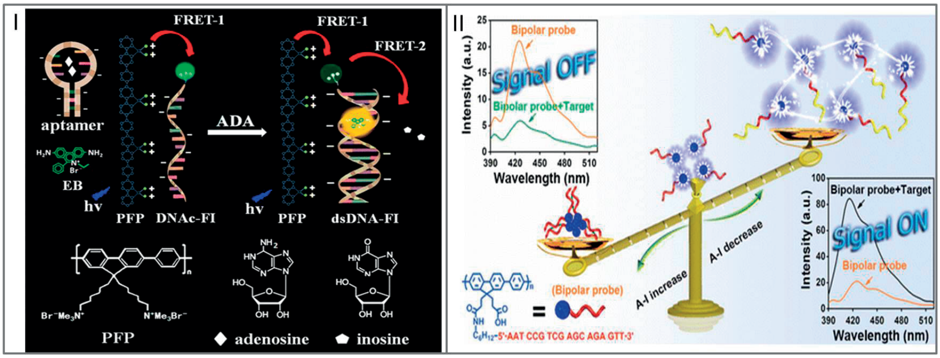

Figure 1.9. I: Schematic illustration of the detection of adenosine deaminase (ADA) and the chemical structures used in this system. Reproduced with permission.[79] Copyright 2014, American Chemical Society. II: Schematic representation of telomerase detection using the bipolar beacon (CP-c-DNA). Reproduced with permission.[80] Copyright 2015, American Chemical Society.

Protein conformation is of paramount importance in understanding biomolecular interactions. Conformational changes often direct functional activity.[82] Therefore, monitoring the structure of a protein offers the possibility to understand the functions and biochemical pathways of biological or pathological processes on a molecular, cellular, or even whole organism level. In this regard, the unique conformationally sensitive optical properties of conjugated polymers have proved to be excellent reporters for studying conformational changes of a protein.[67] Inganäs and co-authors pioneered a zwitterionic polythiophene derivative (POWT) used for sensing the conformational change of a synthetic peptide[83] and the Ca^{2+}-induced conformational change of calmodulin (CaM)[84]. The backbone of POWT planarizes when assembling with the α-helical structure of CaM, resulting in a remarkable red shift of both absorption and fluorescence. Upon formation of the Ca^{2+}/CaM complex, a blue shift is observed on account of the transformation of CaM conformation from a closed structure to an open one (**Figure 1.10** I). Furthermore, Xing's group not only used a cationic polythiophene derivative (PMNT) for visual detection of conformational changes of CaM with a much lower detection limit (6.16 pmol),[85] but also fabricated a hybrid probe combining graphene-oxide (GO) with conjugated polymers for sensing of conformational transitions of CaM by using FRET strategy.[86] In comparison with polythiophene probes, this hybrid probe has a higher signal-to-noise ratio, but a dye-label is required.

In addition, the emission spectra of conjugated polymers exhibit distinct vibronic bands owing to the characteristic delocalized electronic structure of backbone, which are uniquely sensitive to the conformational changes.[87] Sprakel *et al.* demonstrated how a conjugated polymer-based optomechanical response sensor can be employed to monitor the assembly of protein capsid.[88] As illustrated in Figure 1.10 II, an anionic water-soluble carboxylated polyfluorene derivative, poly[9,9′-bis(3′-propanoate)fluoren-2,7-yl] sodium salt (PF3), is used as mechanosensor in this work. The coat protein (C_4B^{K12}) is derived from a natural protein capsid (green coil), which is decorated with a cationic binding block (B^{K12}) consisting of 12 lysine residues (red line). In the absence of C_4B^{K12}, three distinct vibronic bands are observed in its photoluminescence spectra which composed of a main band I at 418 nm and two weaker shoulders, II and III, at 436 and 465 nm, respectively (panel B in Figure 1.10 II). These bands are in line with the 0–0, 0–1, and 0–2 vibronic transition according to the Franck-Condon description. However, the PF3 backbone is intensively stretched by the electrostatic binding with B^{K12} handler and formation of the rod-like coat. In this state, the fluorescence spectra of PF3 demonstrate significant changes in the vibronic bands, where the band I disappeares, and a new shoulder (assigned to 0–3 vibronic transition) rises up at 505 nm (panel C in Figure 1.10 II). Meanwhile, the disassembly of capsid can be monitored by the same probe as well.

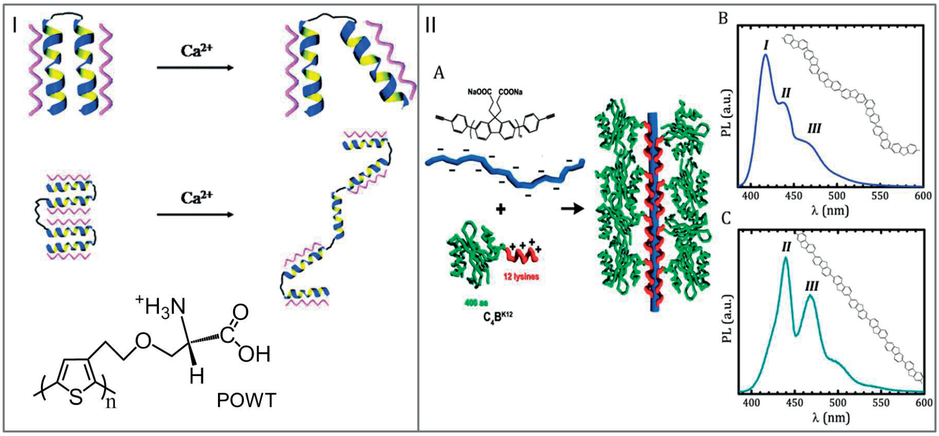

Figure 1.10. I: Chemical structure of POWT, and the schematic representation of the POWT-based probe for sensing the conformational changes of CaM. Blue helices: CaM; pink helices: POWT; top: local view of the EF-hand used for Ca^{2+} binding; bottom: the global conformational change of CaM. Reproduced with permission.[84] Copyright 2004, American Chemical Society. II: (A) Schematic drawing of the structure of PF3 and the coat protein C_4B^{K12}. PL spectra of PF3 in the absence (B) and presence (C) of the coat protein of C_4B^{K12}. Reproduced with permission.[88] Copyright 2015, American Chemical Society.

Misfolding and aggregation of proteins are important pathological hallmarks observed in many devastating diseases including Parkinson's disease, Alzheimer's disease (AD), type II diabetes, and infectious prion diseases.[89,90] The traditional optical sensors for amyloid proteins are Congo red, Thioflavine T (ThT) and Thioflavine S (ThS).[91–93] Recently, luminescent conjugated oligo- and polyelectrolytes have proven to be superb probes for studying protein misfolding and aggregation taking advantage of the unique conformation sensitive optical properties.[94,95] Compared to conventional sensors, conjugated oligo- and polyelectrolytes probe a much broader sub-set of amyloid proteins, and still are more selective as a result of characteristic spectroscopic features. The first proof of concept was demonstrated by Nilsson's group. A conjugated polythiophene functionalized with acetic acid (PTAA) was employed to detect the formation of amyloid fibrils in chicken lysozyme and bovine insulin.[95] Subsequently, a large number of conjugated oligo- and polythiophenes were designed and studied by Nilsson and scientists worldwide.[94,96–100] Representative chemical structures are shown in **Figure 1.11**. The best results are obtained for oligothiophenes with 5–7 units that are grafted with carboxylate groups and other functional moieties. As a representative example, they designed an hybrid pentameric oligothiophene linked to a porphyrin moiety (*p*-FTAA-porph), which can be used for optically studying the Aβ 1–42 amyloid fibrils and Aβ deposits by fluorescence lifetime imaging *in vivo* (**Figure 1.12** I).[101] The identification ability of oligothiophene for Aβ deposits is significantly enhanced by porphyrin group. Aβ deposits and aggregated Aβ species are clearly and selectively identified by *p*-FTAA-porph in brain tissue sections from a transgenic mouse model with Alzheimer's disease (AD) pathology. The red fibrils assigned to porphyrin are certain areas of the Aβ deposits stained by *p*-FTAA-porph, whereas the neighboring green regions exhibit a similar property to *p*-FTAA without the porphyrin moiety. Furthermore, the samples were studied by fluorescence lifetime imaging (FLIM). Three different lifetime distributions are observed when excited at 405, 490, and 565 nm, respectively. Hence, the interplay between joint optical moieties could be employed to improve molecular insight in heterogeneous protein deposits. In addition, Aguzzi and co-workers developed a superresolution platform used for imaging of the α-synuclein amyloid fibrils based on the binding-activated localization microscopy (BALM).[102] The luminescent conjugated probes are at an extreme low concentration, and very few molecules are activated along with high fluorescence when binding with amyloid fibrils. Next, the superresolution images of amyloid fibrils are precisely observed by localized probes using a stochastic method before they turn dark as a result of photobleaching (Figure 1.12 II).

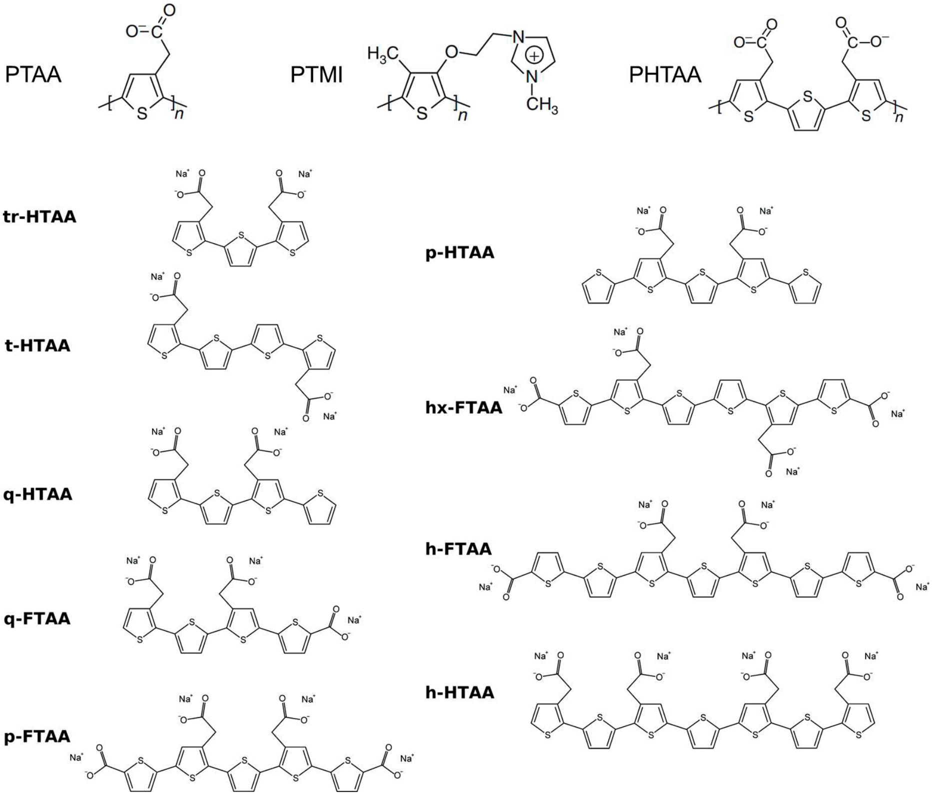

Figure 1.11. Examples of the luminescent conjugated oligo- and polyelectrolytes used for sensing of amyloid protein.

Materials that combine sensing as well as inhibition of protein aggregation offer an ideal strategy for diagnosis and therapy of protein aggregation diseases at same time. Xing and co-authors explored a method for the detection and inhibition of aggregation of hen egg white lysozyme (HEWL) induced by UV illumination, based on a cationic water soluble poly(phenylene vinylene) derivative ($PPV\text{-}NMe_3^+$).[103] As shown in Figure 1.12 III c, the fluorescence intensity of $PPV\text{-}NMe_3^+$ increases gradually with the increasing illumination time due to formation of HEWL aggregates, and becomes six-fold higher after 100 min exposure. So, they proposed that $PPV\text{-}NMe_3^+$ efficiently targets the surface of HEWL aggregates and forms HEWL/$PPV\text{-}NMe_3^+$ complexes by means of hydrophobic interactions between them, resulting in a good dispersion and increasing of fluorescence of $PPV\text{-}NMe_3^+$ due to reduction of self-quenching. Furthermore, the inhibition of HEWL aggregation by

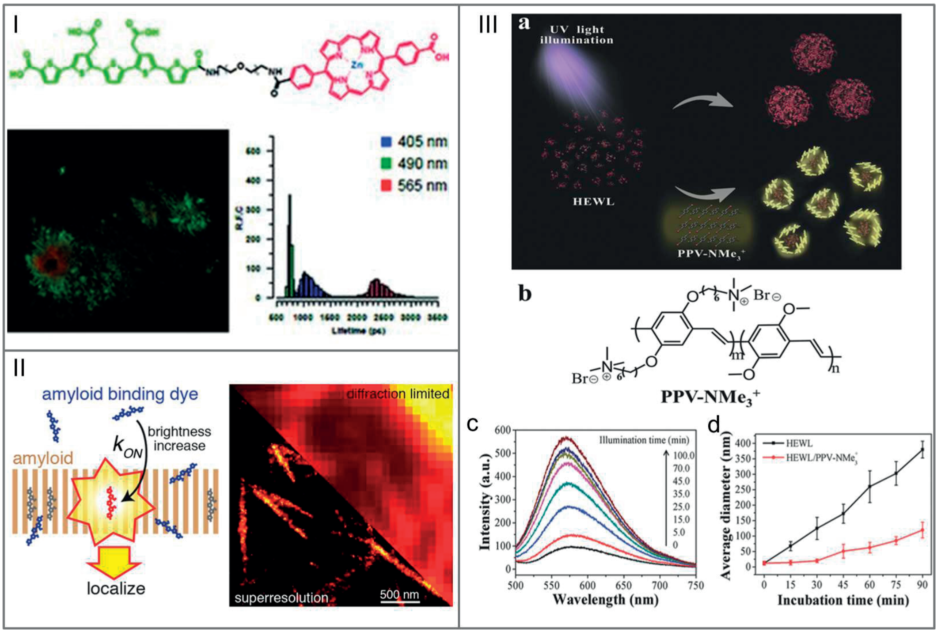

Figure 1.12. I: Chemical structure of hybrid pentameric oligothiophene linked with porphyrin (*p*-FTAA-porph), fluorescence images of Aβ-deposits stained by *p*-FTAA-porph in a brain tissue section, and photoluminescence lifetimes of *p*-FTAA-porph stained Aβ-deposits excited at 405, 490, and 565 nm, respectively. Reproduced with permission.[101] Copyright 2013, Wiley-VCH. II: Schematic illustration of superresolution imaging of amyloid fibrils based on binding activated optical probes. Reproduced with permission.[102] Copyright 2013, American Chemical Society. III: Principle of detection and inhibition of UV illumination induced HEWL aggregation using $PPV\text{-}NMe_3^+$ (a), and its chemical structure (b). (c) Emission spectra of $PPV\text{-}NMe_3^+$ in the presence of HEWL proteins with different illumination time. (d) DLS analysis of the HEWL aggregation induced by UV illumination with the increasing incubation time with and without $PPV\text{-}NMe_3^+$ at room temperature. Reproduced with permission.[103] Copyright 2016, Wiley-VCH.

PPV-NMe$_3^+$ was studied by DLS. The average diameters of HEWL aggregation increase with incubation time after triggering by UV illumination for 15.0 min. However, the size of HEWL only slightly increase after addition of PPV-NMe$_3^+$, which means that the growth rate of HEWL aggregation is significantly inhibited by PPV-NMe$_3^+$ due to the formation of HEWL/PPV-NMe$_3^+$ complexes (Figure 1.12 III d). Similarly, the Iyer[104] and He[105] research groups showed the disruption of amyloid fibrils using conjugated polymers as well.

1.3.3 Others

Water-soluble conjugated polymers have been extensively explored to detect the various intermediates and products of metabolisms which play vital roles in all kinds of biological processes. Wang and co-authors recently fabricated a micelle composed of carboxylated polyfluorene (PFTBTCOOH) and a chitosan-graft-oleic acid (CS-graft-OA), used for visible detection of aliphatic biogenic amines (BAs) in fields of food safety and public health.[106] In order to facilitate host-analyte interactions, PFTBTCOOH served as the optical probe encapsulated in the CS-graft-OA micelles. In the presence of BAs, the energy of conjugated polymer transfers from the PF to BTCOOH units induced by the bridging action of BAs, resulting in a blue to red color change. This platform exhibits very high selectivity to aliphatic BAs, even in the aromatic or heterocyclic BAs. In addition, several probes based on conjugated polymer have been designed for sensing ATP,[107,108] bilirubin,[109] dopamine,[110] glutathione[111] etc.

1.4 Detection of bacteria

In 2005, Whitten *et al.* reported that both of Gram negative and positive bacteria (*E. coli* and *B. anthracis*, respectively) are killed by a cationic conjugated polymer (PPE) upon the light irradiation.[112] Moreover, Whitten, Schanze and co-workers further developed a strategy with higher biocidal efficiency based on the PPE microcapsules by coating PPE on the surface of $MnCO_3$ particles.[113] These studies initiated a novel and important application field of CPs in photodynamic therapy (PDT), which takes advantage of the ability to produce reactive oxygen species (ROS) under irradiation. The ROS may result in tissue damage and cell death due to the active reaction with a series of nucleophilic compounds and production of hydroperoxides. Recently, CPs-based PDT has attracted a lot of attention both in anticancer and antimicrobial applications, especially with the growing problem of cellular resistance to antibiotics.[114–119] Most recently, Yoon and co-authors reviewed extensively the advances in multimodal imaging and cancer therapy.[120] Here, we will focus on antimicrobial applications.

In general, microbial pathogens such as bacteria and fungi, have a net negatively charged cell wall attributed to the presence of teichoic acids which are anionic biopolymers. In this regard, numerous conjugated polymers with positive charge have been widely used in PDT-based antimicrobial applications based on the strongly electrostatic interactions. Xing's group employed a cationic conjugated polymer (PMNT) to screen the photodynamic antimicrobial chemotherapy photosensitizers (PSs) by virtue of the optical changes upon binding with bacteria.[121] The number of bacteria can be quantitatively calculated from the fluorescence intensity of PMNT in aqueous solution. If the PSs are ineffective, the bacteria reproduce prosperously and assemble with PMNT by tight electrostatic and hydrophobic interactions, leading to aggregates and fluorescence quenching of PMNT. On the contrary, a strong fluorescence of PMNT is observed for effective PSs. In this context, six different commercial PSs were examined via a high-throughput screening method. As demonstrated in **Figure 1.13** I, they employed a 96-well microplate for high throughput screening analyzed by an automatic microplate reader. For the PSs with high efficacy, bright yellow signals are readily measured by the microplate reader. However, PSs with low efficacy result in a dark yellow color. Additionally, the color changes relate to the efficacy of PSs, can be observed by the naked eye under UV light ($\lambda_{max} = 365$ nm), which is in line with the fluorescence spectra measured by microplate reader (Figure 1.13 I b). Furthermore, both the efficacy of PSs and the amount of *E. coli* as a function of PSs concentration can be quantitatively

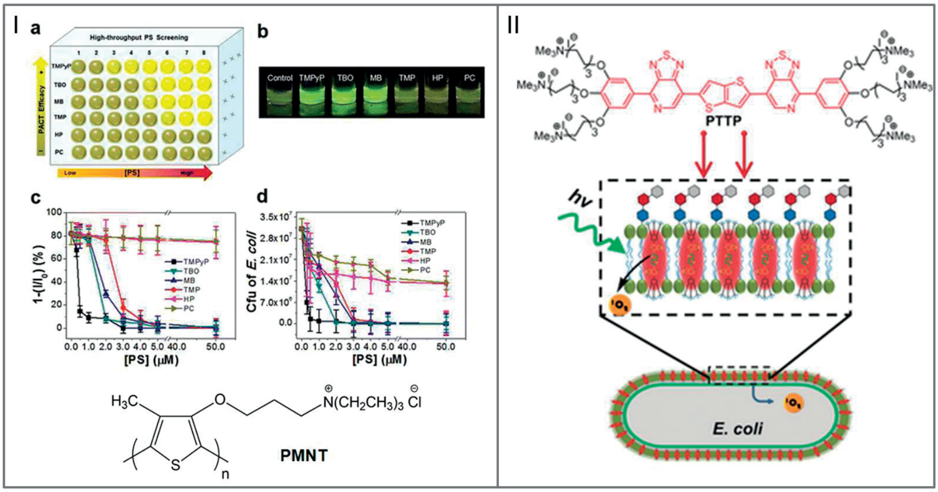

Figure 1.13. I: (a) Schematic representation of the high-throughput screening of PSs based on the fluorescence of PMNT measured by automatic microplate reader. Horizontal axis means PSs as a function of concentration. Vertical axis means different PSs. Bright and dark yellow wells indicate efficient and inefficient photoinactivation of bacteria, respectively. (b) Images of PMNT/*E. coli* complexes after illumination in presence of different PSs under UV light ($\lambda_{max} = 365$ nm). (c) Plot of the fluorescence quenching efficiency of PMNT versus the PSs concentration. (d) Plot of the *E. coli* amount as a function of the the PS concentration. Reproduced with permission.[121] Copyright 2015, American Chemical Society. II: Chemical structure of PTTP, scheme of insertion and ROS generation of PTTP into cell membrane. Reproduced with permission.[122] Copyright 2017, Wiley-VCH.

determined by plotting the fluorescence intensity of PMNT. The authors found that the six PSs studied in this work are classified into three types: the first class with high efficacy includes TMPyP, TBO, and MB; the second class contains TMP with intermediate efficacy; the last class is inefficient and includes HP and PC. Notably, this "mix-and-detect" platform of high-throughput screening is very fast (4.5 h) and cost efficient (~$1.0 for six PSs) and offers a promising route to discover new PSs.

The Bazan and Wang groups explored a membrane-intercalating conjugated oligoelectrolyte (PTTP) which can insert into the cell membrane and produce ROS to efficiently mediate bacteria under a very low light dose (0.6 J cm^{-2}, for commercial porphyrin, the value is 30–266 J cm^{-2}).[122] PTTP structures are composed of three key components which play indispensable functions in photodynamic antimicrobial activities respectively. First, in order to regulate the band gap and obtain red-shifted photophysical properties, both the electron rich (thieno[3,2-b]thiophene) and electron-poor ([1,2,5]thiadiazolo[3,4-c] pyridine) moieties are introduced. Meanwhile, PTTP shows an efficient generation of singlet oxygen ($^1O_2$) with a $\Phi_\Delta = 20\,\%$ under illumination. Second, the appropriate topology and dimensions are designed for insertion into the cell membrane. Third, the good solubility and biocompatibility are the result of the six cationic groups on the termini. The unique properties of membrane-intercalating and accumulation of PTTP endow PTTP with a highly efficient antibacterial capability, especially for the Gram-negative bacteria which are insensitive to PDA due to the protection by the outer membrane.

1.5. Aim and outline of this thesis

We are entering the age of ubiquitous sensing. Our smart phones are tracking our health and wellness all the time. Sensory technologies are extensively drawing much attention and changing our life styles in the present and in the days to come. Optical sensors are very convenient and cost-effective tools for the detection of various analytes. They are based on a change of the photophysical property such as color, absorbance or fluorescence. Water-soluble conjugated polymers (WCPs) are an important class of sensing and electronic materials by virtue of their excellent light harvesting, signal amplification, tunable optoelectronic properties derived from the long π-electron delocalized polymer backbone with many repeat units. In addition, the side chains of WCPs are readily functionalized with desired moieties such as charge carriers, anti-body/gen and stimuli responsive groups, which endow the conjugated polymers with specificity to recognize analytes. With this in mind, the goal of this thesis is to fabricate and study multifunctional hybrid materials for sensing based on the water-soluble conjugated polymers.

As a cellular Ca^{2+}-binding protein of 148 amino acid residues with negative charge on surface, calmodulin (CaM) mediates a large number of Ca^{2+}-dependent signal transductions, and regulates activities of a variety of proteins including CaM kinases and ion channels. There are three different conformations of CaM in nature: 1) closed configuration, inactive state and without Ca^{2+}; 2) open configuration, active state and binding with Ca^{2+}; 3) compact configuration, working state and binding with target proteins. The conformational changes play a very important role in biomolecular processes, contributing to Ca^{2+}-mediated intracellular signaling transductions. Taking advantage of the flexible backbone of the cationic polythiophene PMNT, we demonstrate in **Chapter 2** a strategy for visual detection of conformational changes of CaM, only when CaM is bound to the target peptide M13 to form the complex CaM-M13 in the presence of Ca^{2+}. Assembly between PMNT and CaM-M13 are directly dominated by the conformational changes of CaM triggered by binding with Ca^{2+}, resulting in the relatively blue or red-shifted absorption and emission wavelength of PMNT. We also studied the selectivity of this strategy towards other proteins (BSA, LZM and SA) and other ions (Mg^{2+}, Ba^{2+}, Sr^{2+}, Na^+ and K^+) , and found that PMNT-based assay is selective for the hybrid protein of CaM-M13. Unfortunately, the assay suffers from a high background signal arising from nonspecific interactions. In this context, a graphene oxide (GO) and conjugated polymer hybrid probe for CaM sensing with high signal to noise ratio by using a FRET approach is presented in **Chapter 3**. In this system, GO enhances the selectivity for CaM due to its interaction with biomolecules via multiple noncovalent interactions; poly(fluorene-*co*-phenylene) PFP as energy doner, improves the sensitivity based on the light harvesting property. Upon binding with Ca^{2+}, the conformational changes of CaM create less negatively charge and more hydrophobic surface area, leading to two different assemblies between GO and CaM, one with and one without Ca^{2+}. The conformational changes of CaM are quantitatively monitored through the FRET ratio between PFP and the enhanced green fluorescent protein (EGFP) labeled at the N-terminus of CaM.

Chapter 4 describes a sensor composed of guanidinium-pendent oligofluorene (G-OF) and water-soluble conjugated polythiophene (PTP) used for the “turn-on” detection of carbon dioxide (CO_2). This hybrid sensor is based on the assembly/disassembly between the guanidinium groups of G-OF and the carboxylate moieties of PTP which are CO_2 responsive. In the presence of CO_2, the electrostatic repulsion between G-OF and PTP can be effectively enhanced through protonation of the side chains, leading to disassembly of the polymer complex and thus to the “turn-on” of fluorescence. Under UV light, G-OF/PTP-based film shows a dark blue to bright blue color change upon exposure to CO_2. In a practical application, we employed this system for monitoring the concentration changes of CO_2 in a photosynthesis process. In order to enhance the response rate and capture the CO_2, we introduced a carbonic anhydrase (CA) into the system in **Chapter 5**. CA efficiently catalyzes the inter-conversion between CO_2 and HCO_3^-. Subsequent protonation of PTP regulates polymer self-assembly via the electrostatic and hydrophobic interactions and forms the heart of the sensing mechanism. Furthermore, the carboxylate side chains of

PTP coordinate with Ca^{2+} to form the chelate of PTP/Ca^{2+}, which can be employed for biomimetic CO_2 sequestration catalyzed by CA with fluorescence monitoring.

Conformation changes based on self-assembly of conjugated semiconducting polymers play an important role both in electronics and chemo/biosensor applications. In **Chapter 6**, we show how the conformation of polythiophene (PMNT) backbone can be controllably stretched by the poorly defined extremities of helical polyisocyanopeptides (PIC). PIC serves as a scaffold to trap and stretch the PMNT into a highly ordered conformation, resulting in a massive red shift (about 200 nm) both in UV-vis and fluorescence spectra. We found that the poorly defined extremities of the PIC backbone dominate the PMNT/PIC assembly, which is experimentally supported by partly denaturing the long PIC polymers. We then investigated the photophysical properties of PMNT/PIC by varying the length of PIC polymer. Finally, **Chapter 7** summarizes the proceeding chapters and provides a perspective for future work.

1.6 References

(1) Burroughes, J.; Bradley, D.; Brown, A.; Marks, R.; Mackay, K.; Friend, R.; Burns, P.; Holmes, A. *Nature* **1990**, *347*, 539.

(2) Cheng, Y.-J.; Yang, S.-H.; Hsu, C.-S. *Chem. Rev.* **2009**, *109*, 5868.

(3) Wang, S.; Bazan, G. C. *Adv. Mater.* **2003**, *15*, 1425.

(4) Gaylord, B. S.; Heeger, A. J.; Bazan, G. C. *Proc. Natl. Acad. Sci. U. S. A.* **2002**, *99*, 10954.

(5) Mei, J.; Bao, Z. *Chem. Mater.* **2013**, *26*, 604.

(6) Kymakis, E.; Amaratunga, G. *Appl. Phys. Lett.* **2002**, *80*, 112.

(7) Coakley, K. M.; McGehee, M. D. *Chem. Mater.* **2004**, *16*, 4533.

(8) Horowitz, G. *Adv. Mater.* **1998**, *10*, 365.

(9) McQuade, D. T.; Pullen, A. E.; Swager, T. M. *Chem. Rev.* **2000**, *100*, 2537.

(10) Feng, L.; Zhu, C.; Yuan, H.; Liu, L.; Lv, F.; Wang, S. *Chem. Soc. Rev.* **2013**, *42*, 6620.

(11) Zhu, C.; Liu, L.; Yang, Q.; Lv, F.; Wang, S. *Chem. Rev.* **2012**, *112*, 4687.

(12) Pinto, M. R.; Schanze, K. S. *Synthesis* **2002**, *2002*, 1293.

(13) Kadajji, V. G.; Betageri, G. V. *Polymers* **2011**, *3*, 1972.

(14) Herland, A.; Inganäs, O. *Macromol. Rapid Commun.* **2007**, *28*, 1703.

(15) He, F.; Tang, Y.; Wang, S.; Li, Y.; Zhu, D. *J. Am. Chem. Soc.* **2005**, *127*, 12343.

(16) DiCesare, N.; Pinto, M. R.; Schanze, K. S.; Lakowicz, J. R. *Langmuir* **2002**, *18*, 7785.

(17) Zhang, H.; Lu, Q.; Zuo, F.; Yuan, R.; Chen, S. *Sens. Actuators. B* **2017**, *241*, 887.

(18) Zhou, Y.; Zhang, J.; Zhao, L.; Li, Y.; Chen, H.; Li, S.; Cheng, Y. *ACS Appl. Mater. Interfaces* **2016**, *8*, 1520.

(19) Rana, S.; Elci, S. G.; Mout, R.; Singla, A. K.; Yazdani, M.; Bender, M.; Bajaj, A.; Saha, K.; Bunz, U. H.; Jirik, F. R. *J. Am. Chem. Soc.* **2016**, *138*, 4522.

(20) Gaylord, B. S.; Heeger, A. J.; Bazan, G. C. *J. Am. Chem. Soc.* **2003**, *125*, 896.

(21) Ho, H. A.; Boissinot, M.; Bergeron, M. G.; Corbeil, G.; Dore, K.; Boudreau, D.; Leclerc, M. *Angew. Chem., Int. Edit.* **2002**, *41*, 1548.

(22) Yang, Q.; Dong, Y.; Wu, W.; Zhu, C.; Chong, H.; Lu, J.; Yu, D.; Liu, L.; Lv, F.; Wang, S. *Nat. Commun.* **2012**, *3*, 1206.

(23) Li, K.; Pan, J.; Feng, S. S.; Wu, A. W.; Pu, K. Y.; Liu, Y.; Liu, B. *Adv. Funct. Mater.* **2009**, *19*, 3535.

(24) Pecher, J.; Huber, J.; Winterhalder, M.; Zumbusch, A.; Mecking, S. *Biomacromolecules* **2010**, *11*, 2776.

(25) Chemburu, S.; Corbitt, T. S.; Ista, L. K.; Ji, E.; Fulghum, J.; Lopez, G. P.; Ogawa, K.; Schanze, K. S.; G. Whitten, D. *Langmuir* **2008**, *24*, 11053.

(26) Xing, C.; Xu, Q.; Tang, H.; Liu, L.; Wang, S. *J. Am. Chem. Soc.* **2009**, *131*, 13117.

(27) Ji, E.; Corbitt, T. S.; Parthasarathy, A.; Schanze, K. S.; Whitten, D. G. *ACS Appl. Mater. Interfaces* **2011**, *3*, 2820.

(28) König, K.; Teschke, M.; Sigusch, B.; Glockmann, E.; Eick, S.; Pfister, W. *Cell. Mol. Biol.* **2000**, *46*, 1297.

(29) Dolmans, D. E.; Fukumura, D.; Jain, R. K. *Nat. Rev. Cancer* **2003**, *3*, 380.

(30) Martinez-Manez, R.; Sancenón, F. *Chem. Rev.* **2003**, *103*, 4419.

(31) Wang, F.; Wang, L.; Chen, X.; Yoon, J. *Chem. Soc. Rev.* **2014**, *43*, 4312.

(32) Feng, X.; Liu, L.; Wang, S.; Zhu, D. *Chem. Soc. Rev.* **2010**, *39*, 2411.

(33) Guais, A.; Brand, G.; Jacquot, L.; Karrer, M.; Dukan, S.; Grévillot, G.; Molina, T. J.; Bonte, J.; Regnier, M.; Schwartz, L. *Chem. Res. Toxicol.* **2011**, *24*, 2061.

(34) Bertoni, G.; Ciuchini, C.; Tappa, R. *Atmos. Environ.* **2004**, *38*, 1625.

(35) Cox, P. M.; Betts, R. A.; Jones, C. D.; Spall, S. A.; Totterdell, I. J. *Nature* **2000**, *408*, 184.

(36) Leaf, D.; Verolme, H. J.; Hunt, W. F. *Environ. Int.* **2003**, *29*, 303.

(37) Xu, Q.; Lee, S.; Cho, Y.; Kim, M. H.; Bouffard, J.; Yoon, J. *J. Am. Chem. Soc.* **2013**, *135*, 17751.

(38) Guais, A.; Brand, G.; Jacquot, L.; Karrer, M.; Dukan, S.; Grévillot, G.; Molina, T. J.; Bonte, J.; Regnier, M.; Schwartz, L. *Chem. Res. Toxicol.* **2011**, *24*, 2061.

(39) Guo, Z.; Song, N. R.; Moon, J. H.; Kim, M.; Jun, E. J.; Choi, J.; Lee, J. Y.; Bielawski, C. W.; Sessler, J. L.; Yoon, J. *J. Am. Chem. Soc.* **2012**, *134*, 17846.

(40) Cox, P. M.; Pearson, D.; Booth, B. B.; Friedlingstein, P.; Huntingford, C.; Jones, C. D.; Luke, C. M. *Nature* **2013**, *494*, 341.

(41) Fan, Y.; Xing, C.; Yuan, H.; Chai, R.; Zhao, L.; Zhan, Y. *ACS Appl. Mater. Interfaces* **2017**.

(42) Oter, O.; Ertekin, K.; Derinkuyu, S. *Talanta* **2008**, *76*, 557.

(43) Amao, Y.; Nakamura, N. *Sens. Actuators. B* **2005**, *107*, 861.

(44) Neethirajan, S.; Jayas, D.; Sadistap, S. *Food Bioprocess Technol.* **2009**, *2*, 115.

(45) Dansby-Sparks, R. N.; Jin, J.; Mechery, S. J.; Sampathkumaran, U.; Owen, T. W.; Yu, B. D.; Goswami, K.; Hong, K.; Grant, J.; Xue, Z.-L. *Anal. Chem.* **2010**, *82*, 593.

(46) Ji, X.; Yao, Y.; Li, J.; Yan, X.; Huang, F. *J. Am. Chem. Soc.* **2012**, *135*, 74.

(47) Kim, H. N.; Guo, Z.; Zhu, W.; Yoon, J.; Tian, H. *Chem. Soc. Rev.* **2011**, *40*, 79.

(48) Esser, B.; Swager, T. M. *Angew. Chem., Int. Edit.* **2010**, *122*, 9056.

(49) Xing, C.; Yu, M.; Wang, S.; Shi, Z.; Li, Y.; Zhu, D. *Macromol. Rapid Commun.* **2007**, *28*, 241.

(50) Tran, D.; Skelton, B. W.; White, A. H.; Laverman, L. E.; Ford, P. C. *Inorg. Chem.* **1998**, *37*, 2505.

(51) Zhai, D.; Shi, W.; Hui, Y.; Xie, Z. *J. Polym. Sci., Part A: Polym. Chem.* **2017**, *55*, 1067.

(52) Giovannitti, A.; Nielsen, C. B.; Rivnay, J.; Kirkus, M.; Harkin, D. J.; White, A. J.; Sirringhaus, H.; Malliaras, G. G.; McCulloch, I. *Adv. Funct. Mater.* **2016**, *26*, 514.

(53) Xing, C.; Yuan, H.; Xu, S.; An, H.; Niu, R.; Zhan, Y. *ACS Appl. Mater. Interfaces* **2014**, *6*, 9601.

(54) Hussain, S.; De, S.; Iyer, P. K. *ACS Appl. Mater. Interfaces* **2013**, *5*, 2234.

(55) Huang, X.; Meng, J.; Dong, Y.; Cheng, Y.; Zhu, C. *Polymer* **2010**, *51*, 3064.

(56) Wu, Y.; Dong, Y.; Li, J.; Huang, X.; Cheng, Y.; Zhu, C. *Chem. Asian J.* **2011**, *6*, 2725.

(57) Lei, Y.; Li, H.; Gao, W.; Liu, M.; Chen, J.; Ding, J.; Huang, X.; Wu, H. *J. Mater. Chem. C* **2014**, *2*, 7402.

(58) Xu, Q.; Lee, K. M.; Wang, F.; Yoon, J. *J. Mater. Chem.* **2011**, *21*, 15214.

(59) Ding, J.; Li, H.; Xie, Y.; Peng, Q.; Li, Q.; Li, Z. *Polym. Chem.* **2017**, *8*, 2221.

(60) Kim, I.-B.; Bunz, U. H. *J. Am. Chem. Soc.* **2006**, *128*, 2818.

(61) Liu, X.; Tang, Y.; Wang, L.; Zhang, J.; Song, S.; Fan, C.; Wang, S. *Adv. Mater.* **2007**, *19*, 1471.

(62) Lu, Y.; Li, X.; Wang, G.; Tang, W. *Biosens. Bioelectron.* **2013**, *39*, 231.

(63) Lee, J.; Kim, H.-J.; Kim, J. *J. Am. Chem. Soc.* **2008**, *130*, 5010.

(64) Ballard-Barbash, R.; Friedenreich, C. M.; Courneya, K. S.; Siddiqi, S. M.; McTiernan, A.; Alfano, C. M. *J. Natl. Cancer Inst.* **2012**, *104*, 815.

(65) Orrù, G.; Pettersson-Yeo, W.; Marquand, A. F.; Sartori, G.; Mechelli, A. *Neurosci. Biobehav. Rev.* **2012**, *36*, 1140.

(66) Liu, R.; Wang, X.; Aihara, K.; Chen, L. *Med. Res. Rev.* **2014**, *34*, 455.

(67) Li, K.; Liu, B. *Polym. Chem.* **2010**, *1*, 252.

(68) Doré, K.; Dubus, S.; Ho, H.-A.; Lévesque, I.; Brunette, M.; Corbeil, G.; Boissinot, M.; Boivin, G.; Bergeron, M. G.; Boudreau, D. *J. Am. Chem. Soc.* **2004**, *126*, 4240.

(69) Xing, X.-J.; Liu, X.-G.; He, Y.; Lin, Y.; Zhang, C.-L.; Tang, H.-W.; Pang, D.-W. *Biomacromolecules* **2012**, *14*, 117.

(70) Zhang, Z.; Xia, X.; Xiang, X.; Huang, F.; Han, L. *Sens. Actuators. B* **2017**, *249*, 8.

(71) Liu, X.; Fan, Q.; Huang, W. *Biosens. Bioelectron.* **2011**, *26*, 2154.

(72) Song, J.; Zhang, J.; Lv, F.; Cheng, Y.; Wang, B.; Feng, L.; Liu, L.; Wang, S. *Angew. Chem., Int. Edit.* **2013**, *52*, 13020.

(73) Consortium, G. *Science* **2015**, *348*, 648.

(74) Samuels, Y.; Wang, Z.; Bardelli, A.; Silliman, N.; Ptak, J.; Szabo, S.; Yan, H.; Gazdar, A.; Powell, S. M.; Riggins, G. J. *Science* **2004**, *304*, 554.

(75) Ho, H.-A.; Leclerc, M. *J. Am. Chem. Soc.* **2004**, *126*, 1384.

(76) Liu, X.; Shi, L.; Hua, X.; Huang, Y.; Su, S.; Fan, Q.; Wang, L.; Huang, W. *ACS Appl. Mater. Interfaces* **2014**, *6*, 3406.

(77) Chen, J.; Zhang, J.; Li, J.; Yang, H.-H.; Fu, F.; Chen, G. *Biosens. Bioelectron.* **2010**, *25*, 996.

(78) Wang, X.; Li, S.; Zhang, P.; Lv, F.; Liu, L.; Li, L.; Wang, S. *Adv. Mater.* **2015**, *27*, 6040.

(79) Wang, C.; Tang, Y.; Liu, Y.; Guo, Y. *Anal. Chem.* **2014**, *86*, 6433.

(80) Jia, Y.; Zuo, X.; Lou, X.; Miao, M.; Cheng, Y.; Min, X.; Li, X.; Xia, F. *Anal. Chem.* **2015**, *87*, 3890.

(81) Bai, J.; Liu, C.; Yang, T.; Wang, F.; Li, Z. *Chem. Commun.* **2013**, *49*, 3887.

(82) Grant, B. J.; Gorfe, A. A.; McCammon, J. A. *Curr. Opin. Struct. Biol.* **2010**, *20*, 142.

(83) Nilsson, K. P. R.; Rydberg, J.; Baltzer, L.; Inganäs, O. *Proc. Natl. Acad. Sci. U. S. A.* **2003**, *100*, 10170.

(84) Nilsson, K. P. R.; Inganäs, O. *Macromolecules* **2004**, *37*, 9109.

(85) Yuan, H.; Xing, C.; An, H.; Niu, R.; Li, R.; Yan, W.; Zhan, Y. *ACS Appl. Mater. Interfaces* **2014**, *6*, 14790.

(86) Yuan, H.; Qi, J.; Xing, C.; An, H.; Niu, R.; Zhan, Y.; Fan, Y.; Yan, W.; Li, R.; Wang, B. *Adv. Funct. Mater.* **2015**, *25*, 4412.

(87) Kuehne, A. J.; Kaiser, M.; Mackintosh, A. R.; Wallikewitz, B. H.; Hertel, D.; Pethrick, R. A.; Meerholz, K. *Adv. Funct. Mater.* **2011**, *21*, 2564.

(88) Cingil, H. E.; Storm, I. M.; Yorulmaz, Y.; te Brake, D. W.; de Vries, R.; Cohen Stuart, M. A.; Sprakel, J. *J. Am. Chem. Soc.* **2015**, *137*, 9800.

(89) Hartl, F. U. *Annu. Rev. Biochem.* **2017**.

(90) Chaturvedi, S. K.; Siddiqi, M. K.; Alam, P.; Khan, R. H. *Process Biochem.* **2016**, *51*, 1183.

(91) Maezawa, I.; Hong, H. S.; Liu, R.; Wu, C. Y.; Cheng, R. H.; Kung, M. P.; Kung, H. F.; Lam, K. S.; Oddo, S.; LaFerla, F. M. *J. Neurochem.* **2008**, *104*, 457.

(92) Younan, N. D.; Viles, J. H. *Biochemistry* **2015**, *54*, 4297.

(93) Qin, Z.; Sun, Y.; Jia, B.; Wang, D.; Ma, Y.; Ma, G. *Langmuir* **2017**. *33*, 5398.

(94) Sjöqvist, J.; Maria, J. m.; Simon, R. A.; Linares, M.; Norman, P.; Nilsson, K. P. R.; Lindgren, M. *J. Phys. Chem. A* **2014**, *118*, 9820.

(95) Nilsson, K. P. R.; Herland, A.; Hammarström, P.; Inganäs, O. *Biochemistry* **2005**, *44*, 3718.

(96) Klingstedt, T.; Åslund, A.; Simon, R. A.; Johansson, L. B.; Mason, J. J.; Nyström, S.; Hammarström, P.; Nilsson, K. P. R. *Org. Biomol. Chem.* **2011**, *9*, 8356.

(97) Klingstedt, T.; Shirani, H.; Mahler, J.; Wegenast-Braun, B. M.; Nyström, S.; Goedert, M.; Jucker, M.; Nilsson, K. P. R. *Chem. Eur. J.* **2015**, *21*, 9072.

(98) Herrmann, U. S.; Schütz, A. K.; Shirani, H.; Huang, D.; Saban, D.; Nuvolone, M.; Li, B.; Ballmer, B.; Åslund, A. K.; Mason, J. J. *Sci. Transl. Med.* **2015**, *7*, 299ra123.

(99) Sigurdson, C. J.; Nilsson, K. P. R.; Hornemann, S.; Manco, G.; Polymenidou, M.; Schwarz, P.; Leclerc, M.; Hammarström, P.; Wüthrich, K.; Aguzzi, A. *Nat. Methods* **2007**, *4*, 1023.

(100) Magnusson, K.; Simon, R.; Sjölander, D.; Sigurdson, C. J.; Hammarström, P.; Nilsson, K. P. R. *Prion* **2014**, *8*, 319.

(101) Arja, K.; Sjölander, D.; Åslund, A.; Prokop, S.; Heppner, F. L.; Konradsson, P.; Lindgren, M.; Hammarström, P.; Åslund, K.; Nilsson, K. P. R. *Macromol. Rapid Commun.* **2013**, *34*, 723.

(102) Ries, J.; Udayar, V.; Soragni, A.; Hornemann, S.; Nilsson, K. P. R.; Riek, R.; Hock, C.; Ewers, H.; Aguzzi, A. A.; Rajendran, L. *ACS Chem. Neurosci.* **2013**, *4*, 1057.

(103) Chai, R.; Xing, C.; Qi, J.; Fan, Y.; Yuan, H.; Niu, R.; Zhan, Y.; Xu, J. *Adv. Funct. Mater.* **2016**, *26*, 9026.

(104) Muthuraj, B.; Hussain, S.; Iyer, P. K. *Polym. Chem.* **2013**, *4*, 5096.

(105) Dou, W.-T.; Lv, Y.; Tan, C.; Chen, G.-R.; He, X.-P. *J. Mater. Chem. B* **2016**, *4*, 4502.

(106) Zhong, H.; Liu, C.; Ge, W.; Sun, R.-C.; Huang, F.; Wang, X. *ACS Appl. Mater. Interfaces* **2017**.

(107) Li, C.; Numata, M.; Takeuchi, M.; Shinkai, S. *Angew Chem Int Edit* **2005**, *44*, 6371.

(108) Chen, Z.; Wu, P.; Cong, R.; Xu, N.; Tan, Y.; Tan, C.; Jiang, Y. *ACS Appl. Mater. Interfaces* **2015**, *8*, 3567.

(109) Senthilkumar, T.; Asha, S. *Macromolecules* **2015**, *48*, 3449.

(110) Khudaish, E. A.; Al-Nofli, F.; Rather, J. A.; Al-Hinaai, M.; Laxman, K.; Kyaw, H. H.; Al-Harthy, S. *J. Electroanal. Chem.* **2016**, *761*, 80.

(111) Huang, H.; Shi, F.; Li, Y.; Niu, L.; Gao, Y.; Shah, S. M.; Su, X. *Sens. Actuators. B* **2013**, *178*, 532.

(112) Lu, L.; Rininsland, F. H.; Wittenburg, S. K.; Achyuthan, K. E.; McBranch, D. W.; Whitten, D. G. *Langmuir* **2005**, *21*, 10154.

(113) Corbitt, T. S.; Sommer, J. R.; Chemburu, S.; Ogawa, K.; Ista, L. K.; Lopez, G. P.; Whitten, D. G.; Schanze, K. S. *ACS Appl. Mater. Interfaces* **2008**, *1*, 48.

(114) Whitten, D. G.; Schanze, K. S.; Ji, E.; Dascier, D.; Parthasarathy, A.; Corbitt, T. S.; Cicotte, K.; Dirk, E. L.; Zhu, X.; Google Patents: 2017.

(115) Huang, Y.; Pappas, H. C.; Zhang, L.; Wang, S.; Cai, R.; Tan, W.; Wang, S.; Whitten, D. G.; Schanze, K. S. *Chem. Mater.* **2017**.

(116) Yuan, H.; Wang, B.; Lv, F.; Liu, L.; Wang, S. *Adv. Mater.* **2014**, *26*, 6978.

(117) Lee, S.; Cheng, H.; Chi, M.; Xu, Q.; Chen, X.; Eom, C.-Y.; James, T. D.; Park, S.; Yoon, J. *Biosens. Bioelectron.* **2016**, *77*, 1016.

(118) Bai, H.; Yuan, H.; Nie, C.; Wang, B.; Lv, F.; Liu, L.; Wang, S. *Angew. Chem., Int. Edit.* **2015**, *54*, 13208.

(119) Yang, T.; Liu, L.; Deng, Y.; Guo, Z.; Zhang, G.; Ge, Z.; Ke, H.; Chen, H. *Adv. Mater.* **2017**.

(120) Li, X.; Kim, J.; Yoon, J.; Chen, X. *Adv. Mater.* **2017**.

(121) Li, R.; Niu, R.; Qi, J.; Yuan, H.; Fan, Y.; An, H.; Yan, W.; Li, H.; Zhan, Y.; Xing, C. *ACS Appl. Mater. Interfaces* **2015**, *7*, 14569.

(122) Wang, B.; Wang, M.; Mikhailovsky, A.; Wang, S.; Bazan, G. C. *Angew. Chem., Int. Edit.* **2017**, *56*, 5031.

CHAPTER 2

CA^{2+}-CONTROLLED ASSEMBLY FOR VISUALIZED DETECTION OF CONFORMATION CHANGES OF CALMODULIN

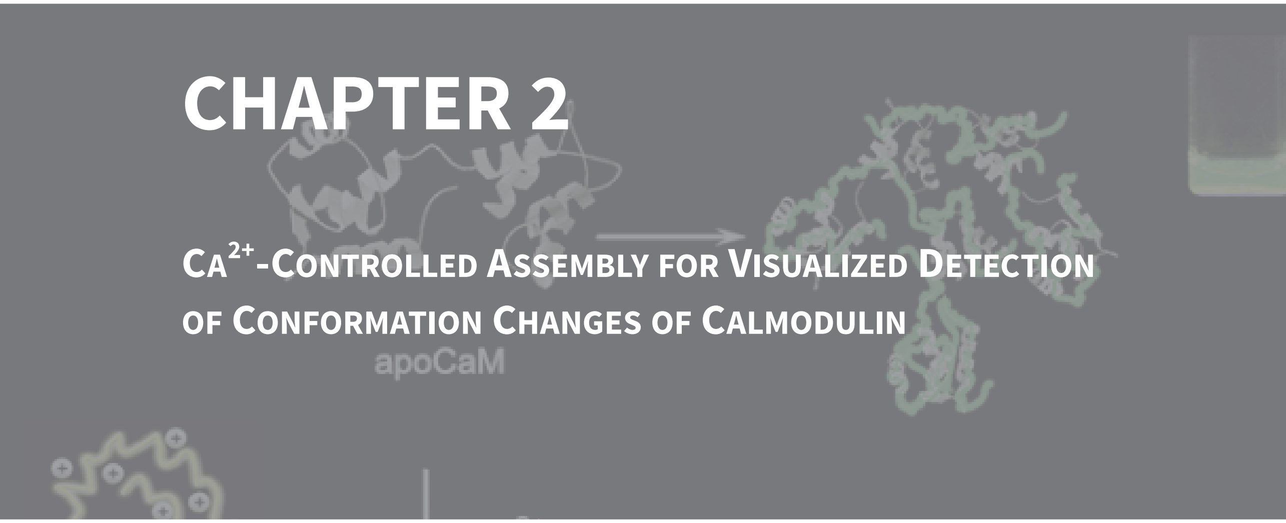

This chapter has been published in:
Yuan, H.; Xing, C.; An, H.; Niu, R.; Li, R.; Yan, W.; Zhan, Y. *ACS Appl. Mater. Interfaces* **2014**, *6*, 14790–14794.

Li R., Yan W. and Niu R. are acknowledged for the synthesis and characterization of PMNT. Prof. An H. is acknowledged for discussions on the interpretation of the results. Prof. Xing C. and Prof. Zhan Y. supervised the project.

Abstract

A new strategy has been designed for the visualized detection of the conformation changes of calmodulin bound to target peptide (CaM-M13) based on the conformation sensitive property of a water-soluble conjugated polythiophene derivative (PMNT) and the electrostatic interactions of PMNT/CaM-M13. Interestingly, the direct visualized PMNT color changes under UV irradiation and the turbidity changes of samples in aqueous medium can be applied to detect the conformation changes as well as the controllable assembly of PMNT/CaM-M13 with Ca^{2+} in aqueous medium. Because of specific binding of Ca^{2+}, the assembly of PMNT/CaM-M13 can be applied to sense the calcium as well.

2.1 Introduction

Calmodulin (CaM) functions as a calcium sensor in cells, mediating a variety of intracellular signaling transductions by binding of calcium.[1] The closed conformation of calcium free form converts to a compact structure upon binding with target protein in the presence of calcium.[2] The C terminus of CaM has been bound to the target peptide of M13, the 577 to 602 residues of skeletal myosin light-chain kinase, leading to the formation of the hybrid protein of CaM-M13.[3] The closed dumb-bell-like conformation of calcium free form (apoCaM-M13) converts to a compact globular structure upon binding with Ca^{2+} (Ca^{2+}/CaM-M13).[2–5] Such a conformation change is very important biomolecular process, forming one part in Ca^{2+} mediated intracellular signaling transductions.[6] The most conventional techniques to determine the conformations of protein include X-ray crystallography,[7] NMR spectroscopy,[2] and single-pair fluorescence resonance energy transfer.[8] However, these methods require expensive instruments, complicated procedures and veteran experimenter, which limits their applications. Therefore, a new, simple, high sensitive and selective approach to sense the conformation change process of CaM-M13 is urgently needed.

Water-soluble conjugated polymers (WCPs) are well-known for their light-harvesting property and signal amplification by coordinating the action of a large number of absorbing units.[9–11] WCPs have been used for sensitive detection of biological macromolecules and fluorescence imaging, offering remarkable advantages in contrast to small molecule probes.[12–18] The optical properties of conjugated polythiophene have been reported to be highly sensitive to conformational variations of its conjugated backbone.[19–22] For example, Nilsson and Inganäs have introduced conjugated polythiophene as an optical conformation sensitive probe to detect amyloid fibrils and the conformational changes of calmodulin.[16,23–26] Inspired by these observations, we describe here a new simple, label-free, high sensitive visual detection for the conformation changing process of CaM-M13 and present a strategy to control the formation of assemblies of CaM-M13 with PMNT in aqueous medium based on the conformational flexibility of PMNT.

2.2 Results and Discussions

As illustrated in **Scheme 2.1**, we employed a water-soluble, positively charged conjugated polythiophene, poly(3-(3’-*N,N,N*-triethylammonium-1’-propyloxy)- 4-methyl-2,5-thiophene chloride) (PMNT) to detect the conformation changes of CaM-M13. The anionic CaM-M13 with many negatively charged amino acid residues in the four EF-hands of opposing globular domains and the central linker region can form micrometer-sized supramolecular complexes with the cationic PMNT by intense electrostatic interactions, in which PMNT backbone coiled around CaM and transform from a random-coil conformation to a more nonplanar and less conjugated conformation, exhibiting relatively blue-shifted absorption and emission wavelength. However, the blue-shifted values decrease gradually with the addition of Ca^{2+} ions due to the transformation of closed form of apoCaM-M13 to compact form of Ca^{2+}/CaM-M13, which induces the PMNT to return to the random-coil conformation. Moreover, the negative charge density of Ca^{2+}/CaM-M13 becomes lower in contrast to that in apoCaM-M13, and the free Ca^{2+} ions in solution make the negative charge density on surface of CaM-M13 decrease. Therefore, Ca^{2+} ions can induce micrometer-sized supramolecular complexes into well-separate nanoparticles in aqueous medium. Furthermore, the conformational changes of CaM-M13 and the Ca^{2+} controllable assembly of CaM-M13 with PMNT can be monitored directly by “naked-eye” in view of the turbidity changes of samples in aqueous medium and the observed PMNT color changes under UV irradiation.

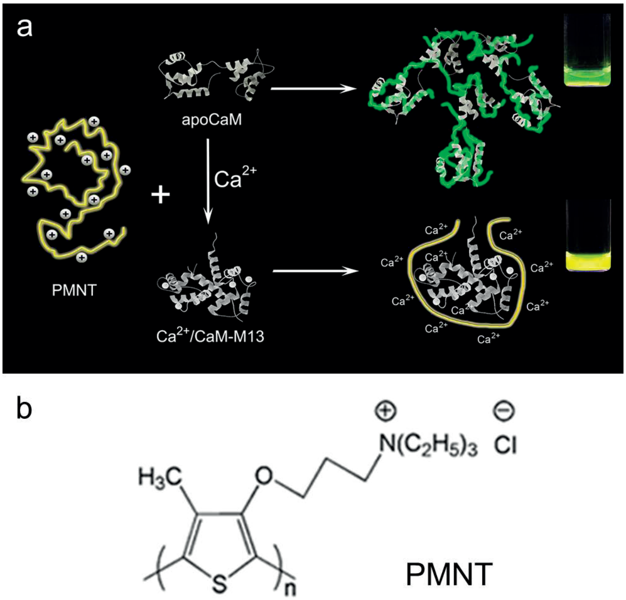

Scheme 2.1. (a) Schematic representation of the detection of conformation changes of CaM-M13 and Ca^{2+} controllable assembly of PMNT/CaM-M13. (b) Chemical structure of the PMNT.

The PMNT shows an absorption maximum at 410 nm, relating to the π–π* transition of the conjugated polythiophenes.[27] The molecular weights of the cationic polythiophene showed that the polymers contain 20-40 thiophene repeat units in the backbone,[27] indicating the intense inter-polyelectrolyte interactions between PMNT and CaM-M13. The PMNT emits yellow fluorescence in Tris-HCl buffer with UV light irradiation and exhibits emission spectra with a maximum at 523 nm, corresponding to a flexible and random-coil conformation of the polythiophenes backbone.[19,28,29] Upon addition of CaM-M13

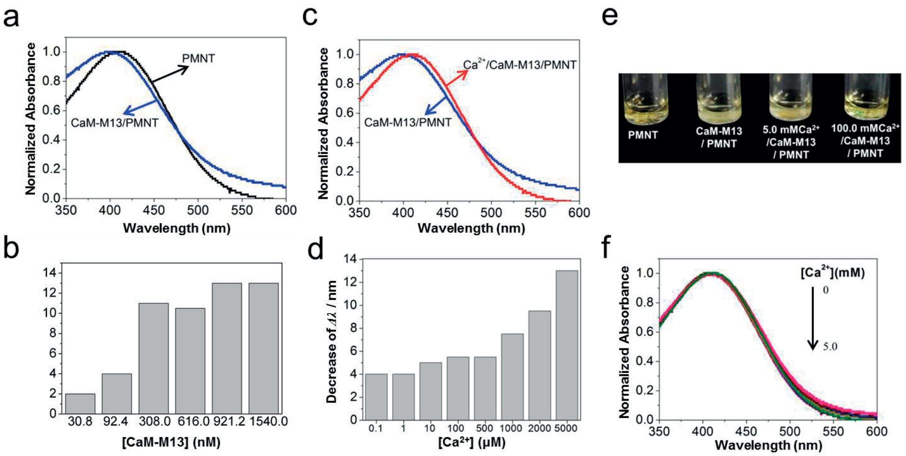

Figure 2.1. (a) The UV-vis spectra of PMNT in the absence and presence of CaM-M13. (b) The blue-shifted value (Δλ) of absorption maximum of PMNT with successive addition of CaM-M13. (c) The UV-vis spectra of CaM-M13/PMNT with and without Ca^{2+} (5.0 mM). (d) The decrease of Δλ of absorption maximum of CaM-M13/PMNT as a function of Ca^{2+} concentrations. (e) Photographs of PMNT, CaM-M13/PMNT, 5.0 mM Ca^{2+}/CaM-M13/PMNT and 100.0 mM Ca^{2+}/CaM-M13/PMNT. [PMNT] = 150.0 μM in repeat units (RUs), [CaM-M13] = 8.4 μM. (f) The UV-vis spectra of PMNT with successive addition of Ca^{2+}. Measurements were performed in Tris-HCl buffer solution (20.0 mM, pH 7.4).

([PMNT] = 25.0 μM in repeat units (RUs), [CaM-M13] = 1.4 μM), the absorption maximum of PMNT was blue-shifted 13 nm (**Figure 2.1**a), indicating transformation from a random-coil conformation to a more nonplanar and less conjugated conformation and formation of the electrostatic complexes of PMNT with CaM-M13. The blue-shifted value (Δλ) of absorption maximum of PMNT with successive addition of CaM-M13 was also examined. As shown in Figure 2.1b, it exhibits the increase of Δλ with adding CaM-M13 and the detection limit can be lowered to 6.16 pmol. However, the Δλ decrease gradually with the addition of Ca^{2+} ions (Figure 2.1d), and when the concentration of Ca^{2+} ions increase to 5.0 mM, the absorption maximum of PMNT return to 410 nm (Figure 2.1c), the same to that of free PMNT in aqueous solution, implying that the PMNT backbone returned to the random-coil conformation of the PMNT alone. Furthermore, the effect of the concentration of Tris-HCl buffer to the *Δλ* was also checked, and the UV-vis spectra and fluorescence emission show about 20 nm changes between PMNT and PMNT/CaM-M13 with 100 mM of Tris-HCl buffer, maximizing the difference of PMNT/CaM-M13 with and without Ca^{2+}. Interestingly, the turbidity changes can be observed by absorption spectra as well as by the naked eye during this conformational changing process. As shown in Figure 2.1e, it shows the changes from clear to turbid upon forming complexes of CaM-M13/PMNT, and the complexes reconvert to clear solution along with adding of Ca^{2+} ions, implying that the anionic CaM-M13 can form supramolecular complexes with the cationic PMNT by electrostatic interactions and Ca^{2+} ions separate the complexes in aqueous medium. The control experiment shows that Ca^{2+} ions cannot alter the absorption spectra of PMNT when adding Ca^{2+} ions successively into solution of PMNT (Figure 2.1f). These results show that it is simple, convenient and visualized to detect the conformation changes of CaM-M13 and the formation of electrostatic assemblies of CaM-M13/PMNT.

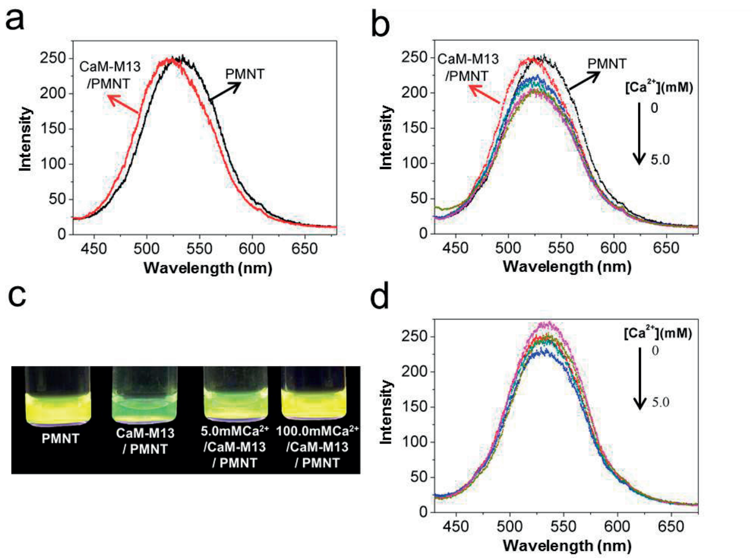

Figure 2.2. (a) Emission spectra of PMNT, CaM-M13/PMNT. (b) Emission spectra of CaM-M13/PMNT as a function of Ca^{2+} concentrations. (c) Fluorescence images of PMNT, CaM-M13/PMNT, 5.0 mM Ca^{2+}/CaM-M13/PMNT and 100 mM Ca^{2+}/CaM-M13/PMNT under UV light (λ_{max} = 365 nm). [PMNT] = 150.0 μM in RUs, [CaM-M13] = 8.4 μM. (d) Emission spectra of PMNT with successive addition of Ca^{2+}. Measurements were performed in Tris-HCl buffer solution (20.0 mM, pH 7.4). The excitation wavelength was 410 nm.

Figure 2.2 exhibits that the fluorescence emission spectra can be applied to probe the conformational changes of CaM-M13 as well. Upon the addition of CaM-M13 ([PMNT] = 30.0 μM in RUs, [CaM-M13] = 1.4 μM), the emission maximum was blue-shifted 11 nm (Figure 2.2a), and the blue-shifted value decrease gradually with the addition of Ca^{2+} ions ($[Ca^{2+}]$ = 0 ~ 5.0 mM) (Figure 2.2b), and when the concentration of Ca^{2+} ions increase to 5.0 mM, the emission spectra of PMNT return to the same with that of free PMNT in aqueous solution. The fluorescence measurements indicate that the PMNT exhibits relatively blue-shifted emission wavelength as a result of the less conjugated and more nonplanar conformation in comparison to PMNT itself in CaM-M13/PMNT complexes, and then reconvert to the random-coil conformation induced by Ca^{2+} ions. Fluorescence images of PMNT, CaM-M13/PMNT, and Ca^{2+}/CaM-M13/PMNT under UV light (λ_{max} = 365 nm) presented a noticeable color changes from yellow to green and then return to yellow (Figure 2.2c). From the emission spectra, fluorescence images and minor interference to the emission of PMNT from Ca^{2+} ions (Figure 2.2d), it offers a versatile methodology without any expensive equipments and sophisticated procedures to probe the CaM-M13 conformational transition. To determine the optimum working pH condition, the blue-shifted value (Δλ) of absorption maximum (**Figure 2.3**) and emission maximum (**Figure 2.4**) for CaM-M13/PMNT and Ca^{2+}/CaM-M13/PMNT at various pH were measured, indicating that the system could satisfy with the physiological pH range.

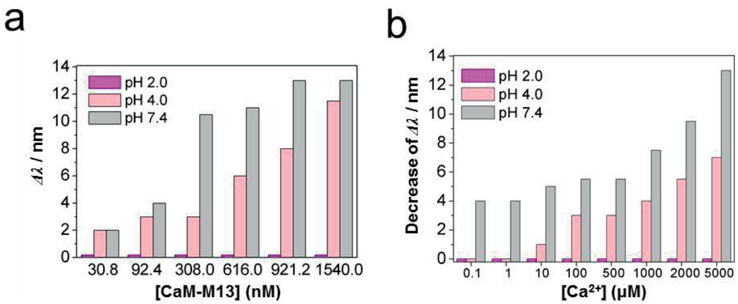

Figure 2.3. (a) The blue-shifted value (Δλ) of absorption maximum of PMNT with successive addition of CaM-M13 at various pH. [PMNT] = 25.0 μM in repeat units (RUs), [CaM-M13] = 3.08×10^{-8} ~ 1.54×10^{-6} M. (b) The decrease of the blue-shifted value (Δλ) of absorption maximum of CaM-M13/PMNT as a function of Ca^{2+} concentrations at various pH. [PMNT] = 25.0 μM in repeat units (RUs), [CaM-M13] = 1.4×10^{-6} M, [Ca^{2+}] = 0 ~ 5.0 mM. Measurements were performed in Tris-HCl buffer solution (20.0 mM).

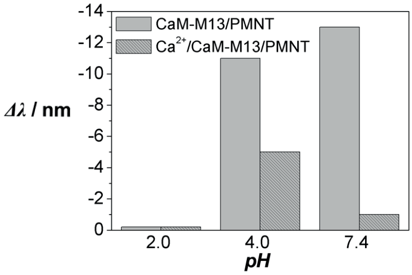

Figure 2.4. The blue-shifted value (Δλ) of emission maximum for CaM-M13/PMNT complex and CaM-M13/Ca^{2+}/PMNT complex at various pH in Tris-HCl buffer (20.0 mM). [PMNT] = 25.0 μM in repeat units (RUs), [CaM-M13] = 1.4×10^{-6} M, [Ca^{2+}] = 5.0 mM.

We conducted the control absorbance and emission measurements for solutions of PMNT containing natural calmodulin (CaM) without M13 in the absence and presence of Ca^{2+}, showing a slight shift as well as that for albumin from bovine serum (BSA), lysozyme

(LZM) and streptavidin (SA), implying that binding to the target peptide of M13 causes the transition from the closed dumb-bell-like conformation of calcium free form to a compact globular structure in the presence of Ca^{2+} and then lead to the conformational change of PMNT (**Table 2.1**). It is noteworthy that the assembly of PMNT/CaM-M13 can also be used to sense the Ca^{2+} ions with high selectivity because of the specific binding of Ca^{2+} (**Figure 2.5**). The decrease of blue-shifted value (Δλ) of absorption maximum of PMNT in Ca^{2+}/CaM-M13/ PMNT versus incubation time of CaM-M13/Ca^{2+} in Tris-HCl buffer was also investigated, indicating that PMNT can be used to detect the process of conformation changes (**Figure 2.6**).

Table 1. Absorption maximum, emission maximum, and the shifted value (Δλ) for solutions of PMNT containing different kinds of proteins (CaM-M13, CaM, BSA, LZM, SA) in the absence and presence of Ca^{2+}.

	Absorption Max (nm)			Emission Max (nm)		
	Protein /PMNT	Ca^{2+}/Protein /PMNT	Δλ	Protein /PMNT	Ca^{2+}/Protein /PMNT	Δλ
CaM-M13	396	408	12	511	522	11
CaM	399	397	-2	511	509	-2
BSA	394	396	2	516	516	0
LZM	410	410	0	522	522	0
SA	408	410	2	518	518	0

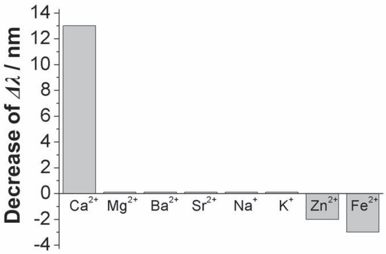

Figure 2.5. The decrease of the blue-shifted value (Δλ) of absorption maximum of CaM-M13/PMNT with various metal ions in Tris-HCl buffer (20.0 mM, pH 7.4). [PMNT] = 25.0 µM in repeat units (RUs), [CaM-M13] = 1.4 ×10^{-6} M, [metal ions] = 5.0 mM.

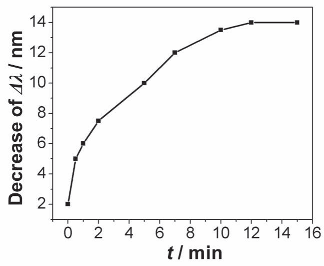

Figure 2.6. The decrease of blue-shifted value (Δλ) of absorption maximum of PMNT in Ca^{2+}/CaM-M13/PMNT versus incubation time of CaM-M13/Ca^{2+} was measured in Tris-HCl buffer (20.0 mM, pH 7.4). [PMNT] = 25.0 μM in repeat units (RUs), [CaM-M13] = 1.4×10^{-6} M, [Ca^{2+}] = 5.0 mM.

In order to investigate the controllable supramolecular assemblies by calcium in aqueous medium, we performed the dynamic light scattering (DLS) measurements in Tris-HCl buffer (20 mM, pH 7.4). As shown in **Figure 2.7**, the average hydrodynamic radius of CaM-M13/PMNT was about 1 μm, which was much larger than that of PMNT and CaM-M13 themself, indicating the formation of larger assembly or aggregation upon addition of CaM-M13 in Tris-HCl buffer and thus the turbid suspension was observed. However, upon the addition of Ca^{2+} ions in aqueous medium, the micrometer-sized supramolecular complexes were disassembled to well-separate nanoparticles with the average hydrodynamic radius of 5 nm, which is close to that of PMNT itself. Furthermore, ζ potentials of CaM-M13 and CaM-M13/PMNT complex with and without Ca^{2+} ions have also been examined in Tris-HCl buffer (**Table 2.2**). For CaM-M13/PMNT complex, ζ potential became less cationic than that of PMNT itself, confirming the electrostatic interactions between PMNT and CaM-M13. For CaM-M13, its ζ potentials data demonstrated that the surface charges became less when binding with Ca^{2+} ions, from -13.0 to -3.1 mV, leading to the weak interactions with PMNT and then disassembly of supramolecular complexes of CaM-M13/PMNT. Considering the DLS and ζ potential measurements, it is proposed that intense electrostatic interaction between the PMNT and apoCaM-M13 makes the formation of micrometer-sized supramolecular assemblies of CaM-M13/PMNT. The CaM-M13 bind with Ca^{2+} in four EF-hands domains and then convert to a compact structure of Ca^{2+}/CaM-M13 when adding of Ca^{2+}, and the negative charge density of Ca^{2+}/CaM-M13 becomes lower in contrast to that in apoCaM-M13, therefore, PMNT return to the random-coil conformation and the assemblies of CaM-M13/PMNT disassemble in aqueous media.

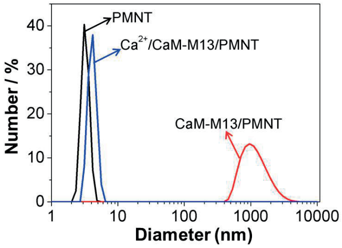

Figure 2.7. Dynamic light scattering analysis of PMNT, CaM-M13/PMNT and Ca^{2+}/CaM-M13/PMNT in Tris-HCl buffer (20.0 mM). [PMNT] = 30.0 μM in repeat units (RUs), [CaM-M13] = 1.4 μM, $[Ca^{2+}]$ = 100.0 mM.

Table 2.2. ζ Potential of PMNT, CaM-M13, Ca^{2+}/CaM-M13, CaM-M13 /PMNT and Ca^{2+}/CaM-M13/PMNT in Tris-HCl buffer (20.0 mM, pH 7.4).

	ζ Potential (mV)
PMNT	21.9
CaM-M13	-13.0
Ca^{2+}/CaM-M13	-3.1
CaM-M13/PMNT	7.28
Ca^{2+}/CaM-M13/PMNT	14.9

2.3 Conclusions

In conclusion, we have developed a straight-forward, simple, label-free and high sensitive visualized detection for the conformation changes of calmodulin bound to target peptide and calcium controllable assembly in aqueous medium based on the conformational flexibility of PMNT. The new electrostatic complex of PMNT/CaM-M13 has several significant characteristics. First, PMNT/CaM-M13 complex can be obtained without covalent linkage of chemical ligands and fluorescent labels, which reduces complicated synthesis procedures. Second, Ca^{2+} ions induce the micrometer-sized supramolecular complexes of PMNT/CaM-M13 into well-separate nanoparticles in aqueous medium. Third, the transition of apoCaM-M13 to Ca^{2+}/CaM-M13 and the Ca^{2+} controllable assembly of CaM-M13 with PMNT were directly visualized with naked-eye by the turbidity changes of samples in aqueous medium and the fluorescence color changes. Last but not least, the assembly of PMNT/CaM-M13 can also be applied as a platform for Ca^{2+} ions detection. This strategy is potential to detect conformation changes induced by biospecific interactions and construct controllable hybrid materials.

2.4 Experimental Section

Materials and Instruments

PMNT was prepared according to a literature procedure.[28] CaM-M13 was gene constructed, expressed in *Escherichia coli* and purified according to a reported method.[3,30] HisTrap FF (17–5319–01) was purchased from GE Healthcare Life Sciences for preparative purification of histidine-tagged recombinant CaM-M13. Natural calmodulin full length protein (from bovine brain) was obtained from Abcam. Standard $CaCl_2$ (1.0 M) was purchased from Sigma. The others were obtained from Aladdin, Acros, or Alfa-Aesar and used as received. All solutions were prepared with MilliQ water (18.2 MXcm). The UV-vis absorption spectra were recorded on a SHIMADZU UV-1800 spectrometer. Fluorescence measurements were taken on a Hitachi F-4500 fluorimeter equipped with a Xenon lamp excitation source. Photographs were taken with a Canon EOS-600D digital camera. Dynamic light scattering (DLS) experiments were carried out on Nano-ZS90 (Malvern Instruments, UK).

Preparation for CaM-M13

CaM-M13 was extracted, purified, identified by SDS-PAGE and dialyzed with 2.0 L of 20.0 mM Tris-HCl, pH 7.4 at 4°C, and its concentration was determined through BCA Protein Assay Kit. Finally, store the CaM-M13 ([CaM-M13] = 28.0×10^{-6} M) at -20 °C, and avoid freeze/thaw cycles.

Preparation for Tris-HCl buffer

For zero-Ca^{2+} buffer, the solution contained 20.0 mM Tris-HCl and 20.0 μM EGTA, adjusted to pH 7.4 with NaOH. For high-Ca^{2+} buffer, the solution contained 20.0 mM Tris-HCl, 20.0 μM EGTA and 100.0 mM $CaCl_2$, adjusted to pH 7.4. Different free [Ca^{2+}] solutions were made by mixing zero-Ca^{2+} and high-Ca^{2+} solutions according to the Ca-EGTA calculator (http://www.stanford.edu/~cpatton/CaEGTA -NIST. htm).

Assay for conformation changes

To 200 μL of Tris-HCl buffer were added different concentrations of CaM-M13 (3.08×10^{-8} ~ 1.54×10^{-6} M), and 25.0 μM of PMNT respectively. After 10 min of incubation, the UV-vis absorption spectra were measured in 100 μL quartz cuvettes at room temperature. For fluorescence spectra, CaM-M13 was mixed with 1.0 mL of Tris-HCl buffer and was added PMNT ([PMNT] = 30.0 μM in RUs, [CaM-M13] = 1.4×10^{-6} M). After 10 min of incubation, the samples were measured the fluorescence spectra in 3 mL quartz cuvettes. CaM-M13 was added to solutions with different concentrations of free Ca^{2+} ([CaM-M13] = 1.4×10^{-6} M, [Ca^{2+}] = 0 ~ 5.0 mM). After incubation of 10 min, PMNT (30.0 μM in RUs) was added. These samples were incubation for 10 min again before the absorption and emission spectra were recorded.

Protein selectivity

To 200 μL of Tris-HCl buffer were added 1.4 μM of CaM-M13, CaM, bovine serum (BSA), lysozyme (LZM) and streptavidin (SA) and 25.0 μM of PMNT respectively. After 10 min of incubation, the UV-vis absorption spectra were measured in 100 μL quartz cuvettes at room temperature. For fluorescence spectra, 1.4 μM of CaM-M13, CaM, bovine serum (BSA), lysozyme (LZM) and streptavidin (SA) was mixed with 1.0 mL of Tris-HCl buffer and was added PMNT respectively (30.0 μM in RUs). After 10 min of incubation, the samples were measured the fluorescence spectra in 3 mL quartz cuvettes. Various protein solutions were added to Tris-HCl buffer solutions with Ca^{2+} (5.0 mM) respectively. After incubation of 10 min, PMNT (30.0 μM in RUs) was added. These samples were incubation for 10 min again before the absorption and emission spectra were recorded.

Ion selectivity of CaM-M13/PMNT

CaM-M13 (1.40×10^{-8} M) was added to the various metal ions (Mg^{2+}, Ba^{2+}, Sr^{2+}, Na^{+}, K^{+}) respectively in Tris-HCl buffer (20 mM Tris-HCl, 20 μM EGTA, pH 7.4, [metal ions] = 5.0 mM). After an incubation of 10 min, PMNT (25.0 μM in repeat units (RUs)) was added. These samples were incubated for 10 min again before the absorption spectra were recorded.

2.5 References

(1) Chin, D.; Means, A. R. *Trends Cell Biol.* **2000**, *10*, 322.

(2) Ikura, M.; Clore, G. M.; Gronenborn, A. M.; Zhu, G.; Klee, C. B.; Bax, A. *Science* **1992**, *256*, 632.

(3) Miyawaki, A.; Llopis, J.; Heim, R.; McCaffery, J. M.; Adams, J. A.; Ikura, M.; Tsien, R. Y. *Nature* **1997**, *388*, 882.

(4) Osawa, M.; Tokumitsu, H.; Swindells, M. B.; Kurihara, H.; Orita, M.; Shibanuma, T.; Furuya, T.; Ikura, M. *Nat. Struct. Biol.* **1999**, *6*, 819.

(5) Finn, B. E.; Forsen, S. *Structure* **1995**, *3*, 7.

(6) Zhang, M.; Abrams, C.; Wang, L.; Gizzi, A.; He, L.; Lin, R.; Chen, Y.; Loll, P. J.; Pascal, J. M.; Zhang, J. F. *Structure* **2012**, *20*, 911.

(7) Babu, Y. S.; Bugg, C. E.; Cook, W. J. *J. Mol. Biol.* **1988**, *204*, 191.

(8) Slaughter, B. D.; Unruh, J. R.; Allen, M. W.; Bieber Urbauer, R. J.; Johnson, C. K. *Biochemistry* **2005**, *44*, 3694.

(9) Swager, T. M. *Acc. Chem. Res.* **1998**, *31*, 201.

(10) Leclerc, M. *Adv. Mater.* **1999**, *11*, 1491.

(11) Feng, L. H.; Zhu, C. L.; Yuan, H. X.; Liu, L. B.; Lv, F. T.; Wang, S. *Chem. Soc. Rev.* **2013**, *42*, 6620.

(12) Wang, F.; Liu, Z.; Wang, B.; Feng, L.; Liu, L.; Lv, F.; Wang, Y.; Wang, S. *Angew. Chem., Int. Ed.* **2014**, *126*, 434.

(13) Feng, L.; Liu, L.; Lv, F.; Bazan, G. C.; Wang, S. *Adv. Mater.* **2014**, *26*, 3926.

(14) Usmani, S. M.; Zirafi, O.; Muller, J. A.; Sandi-Monroy, N. L.; Yadav, J. K.; Meier, C.; Weil, T.; Roan, N. R.; Greene, W. C.; Walther, P.; Nilsson, K. P. R.; Hammarstrom, P.; Wetzel, R.; Pilcher, C. D.; Gagsteiger, F.; Faendrich, M.; Kirchhoff, F.; Munch, J. *Nat. Commun.* **2014**, *5*, 1962.

(15) Feng, X.; Liu, L.; Wang, S.; Zhu, D. *Chem. Soc. Rev.* **2010**, *39*, 2411.

(16) Nilsson, K. P. R.; Hammarström, P.; Wiley–VCH: Weinheim, Germany: 2013.

(17) Lan, M.; Wu, J.; Liu, W.; Zhang, W.; Ge, J.; Zhang, H.; Sun, J.; Zhao, W.; Wang, P. *J. Am. Chem. Soc.* **2012**, *134*, 6685.

(18) Lan, M.; Liu, W.; Wang, Y.; Ge, J.; Wu, J.; Zhang, H.; Chen, J.; Zhang, W.; Wang, P. *ACS Appl. Mater. Interfaces* **2013**, *5*, 2283.

(19) Tang, Y. L.; He, F.; Yu, M. H.; Feng, F. D.; An, L. L.; Sun, H.; Wang, S.; Li, Y. L.; Zhu, D. B. *Macromol. Rapid Commun.* **2006**, *27*, 389.

(20) Pu, F.; Hu, D.; Ren, J.; Wang, S.; Qu, X. *Langmuir* **2009**, *26*, 4540.

(21) Ho, H. A.; Najari, A.; Leclerc, M. *Acc. Chem. Res.* **2008**, *41*, 168.

(22) Charlebois, I.; Gravel, C.; Arrad, N.; Boissinot, M.; Bergeron, M. G.; Leclerc, M. *Macromol. Biosci.* **2013**, *13*, 717.

(23) Nilsson, K. P. R.; Hammarstrom, P.; Ahlgren, F.; Herland, A.; Schnell, E. A.; Lindgren, M.; Westermark, G. T.; Inganas, O. *Chembiochem.* **2006**, *7*, 1096.

(24) Herland, A.; Nilsson, K. P.; Olsson, J. D.; Hammarstrom, P.; Konradsson, P.; Inganas, O. *J. Am. Chem. Soc.* **2005**, *127*, 2317.

(25) Arja, K.; Sjolander, D.; Aslund, A.; Prokop, S.; Heppner, F. L.; Konradsson, P.; Lindgren, M.; Hammarstrom, P.; Aslund, K. O. A.; Nilsson, K. P. R. *Macromol. Rapid Commun.* **2013**, *34*, 723.

(26) Aslund, A.; Sigurdson, C. J.; Klingstedt, T.; Grathwohl, S.; Bolmont, T.; Dickstein, D. L.; Glimsdal, E.; Prokop, S.; Lindgren, M.; Konradsson, P.; Holtzman, D. M.; Hof, P. R.; Heppner, F. L.; Gandy, S.; Jucker, M.; Aguzzi, A.; Hammarstrom, P.; Nilsson, K. P. *ACS Chem. Biol.* **2009**, *4*, 673.

(27) Tang, Y.; Feng, F.; He, F.; Wang, S.; Li, Y.; Zhu, D. *J. Am. Chem. Soc.* **2006**, *128*, 14972.

(28) Ho, H. A.; Boissinot, M.; Bergeron, M. G.; Corbeil, G.; Dore, K.; Boudreau, D.; Leclerc, M. *Angew. Chem., Int. Ed.* **2002**, *41*, 1548.

(29) Liu, X. F.; Tang, Y. L.; Wang, L. H.; Zhang, J.; Song, S. P.; Fan, C. H.; Wang, S. *Adv. Mater.* **2007**, *19*, 1662.

(30) Arndt, K. M.; Müller, K. M. *Protein engineering protocols*; Humana Press: Totowa, N.J., 2007.

CHAPTER 3

GRAPHENE OXIDE-CONJUGATED POLYMER HYBRID MATERIALS FOR CALMODULIN SENSING BY USING FRET STRATEGY

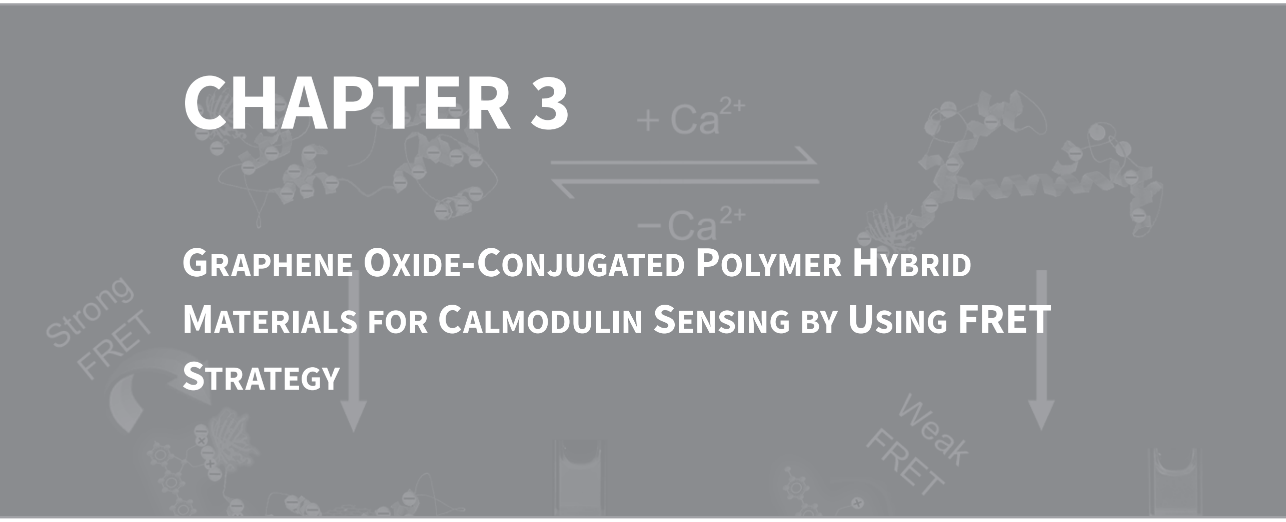

This chapter has been published in:
Yuan, H.; Qi, J.; Xing, C.; An, H.; Niu, R.; Zhan, Y.; Fan, Y.; Yan, W.; Li, R.; Wang, B., Wang, S., *Adv. Funct. Mater.* **2015,** *25*, 4412–4418. (Back cover)

Dr. Qi J. and Niu R. are acknowledged for the synthesis and characterization of GO. Li R., Yan W. and Fan Y. synthesized PFP. Prof. Wang S., Prof. An H. and Wang B. are acknowledged for discussions on the interpretation of the results. Prof. Xing C. and Prof. Zhan Y. supervised the project.

Abstract

The conformation of calmodulin (CaM) changes from closed configuration to open one, converting to a claviform dumbbell-shaped biomolecule upon Ca^{2+}-binding. A hybrid probe of graphene oxide (GO)-cationic conjugated polymer for detection of the conformation transition of CaM by using FRET technique has been demonstrated. The stronger hydrophobic interaction and weaker electrostatic repulsion leads to more CaM adsorption to the surface of GO upon binding with Ca^{2+} than that of CaM in the absence of Ca^{2+} (apoCaM), resulting in much farther distance between poly[(9,9-bis(6'-*N,N,N*-trimethylammonium)hexyl)-fluorenylene phenylene dibromide] (PFP) and green fluorescent protein (EGFP) labeled at the N-terminus of CaM and therefore much weaker FRET efficiency for PFP/Ca^{2+}/CaM in comparison with that of PFP/apoCaM in the presence of GO. Notably, the assembly of CaM with GO is quantitatively and reversibly controlled by Ca^{2+} ions.

3.1 Introduction

As a cellular Ca^{2+}-binding protein of 148 amino acid residues, calmodulin (CaM) mediates a large number of Ca^{2+}-dependent signal transductions, regulating activities of a variety of proteins including CaM kinases and ion channels.[1,2] CaM consists of two globular domains at C- and N- terminus and each contains two canonical EF hands as Ca^{2+}-binding motifs, connected by a flexible linker.[3–5] Upon Ca^{2+}-binding, the conformation of CaM changes from the closed configuration to the open one, converting to a claviform dumbbell-shaped biomolecule with a long and rigid central helix connecting the N-lobe with the C-lobe, exposing much more hydrophobic and less negatively charged surfaces.[6–9] The exposed hydrophobic patches enable Ca^{2+}/CaM to recognize and bind with a wide range of target proteins.[10,11] Therefore, the conformation changes perform an essential part in Ca^{2+} mediated signal transductions. Despite several techniques including NMR,[6] X-ray crystallography[8] and single-molecule spectroscopy[12] were used to determine the conformations of CaM, technical complexity, expensive instruments and veteran experimenter limit their extensive applications.

Graphene is a single-atom-thick nanosheet with two-dimensional shape, which has been extensively explored with exciting applications.[13–17] Graphene oxide (GO)[18] decorated by oxygen-based functional groups has recently been widely used in biological applications,[19,20] resulting from the hybrid structure comprised of sp^2 and sp^3 hybridized carbon atoms that facilitate non-covalent interacting with biomolecules via electrostatic interactions, hydrophobic interactions or non-radiative dipole–dipole coupling.[21,22] Furthermore, GO exhibits amphiphilicity, excellent water dispersibility, efficient fluorescence quenching effect, and excellent surface functionalizability, enabling to perform as an optical probe for biosensing.[23–26] GO has been developed as an efficient platform for detection of biomolecules such as single-strand DNA,[27–31] microribonucleic acid (microRNA),[32,33] enzymes,[34,35] hormone,[36] denosine-5´-triphosphate (ATP),[37] and bioorganisms[38,39] by using GO with fluorescent dye-labeled nucleic acid, aptamers or peptide as probes. Due to the limited capability for recognition of these probes,[40,41] GO-based bioassays for sensing the conformation changes of proteins especially for CaM are still needed.

Water-soluble cationic conjugated polymers (CCPs) are extensively employed in biological detections and fluorescence imaging by virtue of their light-harvesting properties and signal amplification properties.[42–45] Nilsson and Inganäs have developed optical conformation probes to detect amyloid fibrils and calmodulin by using conjugated polythiophene and oligothiophene which is highly conformation sensitive.[46–48] Recently, we have used the optical properties of cationic polythiophene to visually detect the conformation change of CaM bound to synthetic peptide of M13.[49] However, this conjugated polymer-based assay is only workable toward the hybrid protein of CaM-M13, and also exhibits high background signal arising from non-specific interactions. CCPs have been found to have strong π-π interactions with GO and induce efficient fluorescence quenching effect.[50] Consequently, CCPs have recently been combined with GO for new biosensing systems with high signal-to-noise ratio.[40,51,52] For example, Liu and co-workers demonstrated a graphene–conjugated oligomer hybrid probe for sensing of lectin and *Escherichia Coli*.[40] Here, we describe a hybrid probe of graphene oxide-cationic conjugated polymer for detection of Ca^{2+} induced conformation changes of calmodulin by using FRET technique. As illustrated in **Scheme 3.1**, the CaM was labeled with enhanced green fluorescent protein (EGFP) at the N-terminus. Upon Ca^{2+}-binding, the conformation of CaM changes from the closed configuration to the open one, and the flexible linker converts to a rigid α-helix, resulting in the exposure of more hydrophobic and less negatively charge surface. Therefore, in contrast to the apoEGFP-CaM, the EGFP-CaM/Ca^{2+} can be assembled with GO tightly with stronger hydrophobic interaction and weaker electrostatic repulsion, leading to more EGFP-CaM/Ca^{2+} adsorption to the surface of GO. Upon adding PFP (poly[(9,9-bis(6'-*N,N,N*-trimethylammonium)hexyl)-fluorenylene phenylene dibromide]) to EGFP-CaM/Ca^{2+}/GO,

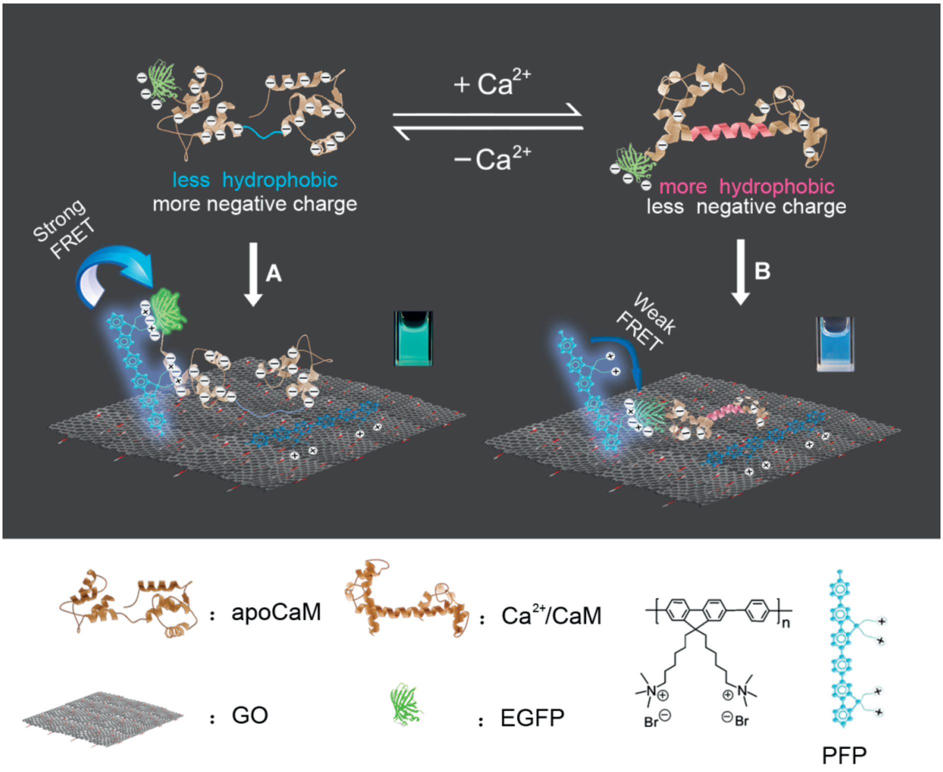

Scheme 3.1. Schematic representation of a GO-PFP based hybrid probe for the detection of conformation changes of calmodulin.

the PFP resides in much farther distance to EGFP than that in PFP/apoEGFP-CaM/GO, and therefore, much weaker FRET is observed in situation B than that in situation A. Interestingly, the assembly can be controlled by Ca^{2+} ions reversibly and circularly. Furthermore, the conformation changes of CaM and the Ca^{2+} controllable assembly of CaM with GO and PFP can be visualized directly in view of the color changes under UV irradiation.

3.2 Results and Discussion

3.2.1 Detection of the conformation changes of calmodulin

PFP with a linear poly(fluorene)s backbone structure is used as the energy donor in FRET experiments, exhibiting an absorption maximum at 375 nm and an emission maximum at 420 nm, which overlaps with the absorption of EGFP.[53–57] Irradiation at 375 nm selectively excited PFP, and the FRET from PFP to EGFP leads to the fluorescence quenching of PFP at 420 nm and appearance of EGFP emission peak at 510 nm. As illustrated in **Figure 3.1**a, in the presence of GO, upon saturation of EGFP-CaM (1.0 µM) with Ca^{2+} ions (5.0 mM) and then PFP (7.5 µM in repeat units (RUs)) was added, the resulting FRET ratio of the fluorescence intensity at 510 nm to that at 420 nm ($I_{510\ nm}/I_{420\ nm}$) shows a much lower signal than that for apoEGFP-CaM. However, in the absence of GO, both EGFP-CaM/Ca^{2+} and apoEGFP-CaM keep tight electrostatic interactions with PFP, and thus the observed FRET efficiency is not changed with adding Ca^{2+} ions (Figure 3.1b). Fluorescence emission ratio of $I_{510\ nm}/I_{420\ nm}$ of the PFP/EGFP-CaM in the presence and absence of GO as a function of Ca^{2+} concentrations was also examined. As exhibited in Figure 3.1c, in the presence of GO, the FRET ratio decreased gradually with the increase of the Ca^{2+} ions concentration and reached the plateau after about 1.0 mM. However, the FRET ratio keep constant without GO. Figure 3.1d shows the fluorescence emission ratio ($I_{510\ nm}/I_{420\ nm}$) of PFP/EGFP-CaM in the presence of GO with various metal ions. For Ba^{2+}, Sr^{2+} and Zn^{2+}, the FRET ratio values show slight changes relative to that of blank which was PFP/EGFP-CaM without metal ions, resulting from their weak binding abilities to CaM to produce conformation changes. For Mg^{2+} ions, the FRET ratio values was 50 % decreased in contrast to the blank since Mg^{2+} ions can bind to CaM and induce a smaller conformational change than that of Ca^{2+} ions.[58] The FRET ratio for Ca^{2+} ions shows about 10 times lower relative to that for Ba^{2+}, Sr^{2+} and Zn^{2+} ions and 5 times lower relative to that for Mg^{2+} ions. Therefore, this GO-PFP based probe can be used to achieve detection of conformation changes of CaM specifically, and

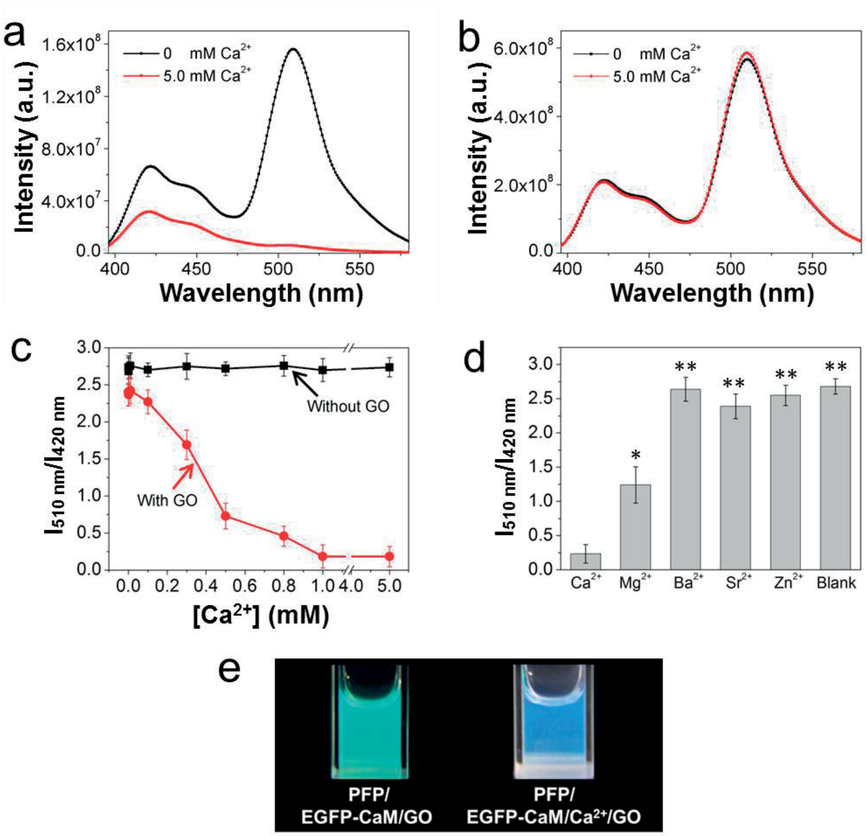

Figure 3.1. Fluorescence emission spectra of the PFP/EGFP-CaM in the presence (a) and absence (b) of GO with and without Ca^{2+}. (c) Fluorescence emission ratio of $I_{510\ nm}/I_{420\ nm}$ of the PFP/EGFP-CaM in the presence and absence of GO as a function of Ca^{2+} concentrations. (d) Fluorescence emission ratio of $I_{510\ nm}/I_{420\ nm}$ of PFP/EGFP-CaM in the presence of GO with various metal ions in HEPES buffer. (e) Fluorescence images of the PFP/EGFP-CaM in the presence of GO with and without Ca^{2+} under UV light (λ_{max} = 365 nm). [GO] = 25.0 µg/mL, [EGFP-CaM] = 1.0 µM, [PFP] = 7.5 µM in repeat units (RUs), [metal ions] = 5.0 mM, [Ca^{2+}] = 0 ~ 5.0 mM. Measurements were performed in HEPES buffer solution (20.0 mM, pH 7.4). The excitation wavelength was 375 nm. All data were presented as mean values ± standard deviation of three separate experiments. Error bars represent standard deviations of data from three separate measurements. Student's t-test was performed to determine statistical significance. Differences between groups were considered to be significant at p-values < 0.05, designated by *; and $p < 0.01$, by**.

the detection limit can be lowered to 50.0 nM by evaluating the FRET ratio changes of PFP/EGFP-CaM with Ca^{2+} relative to that without Ca^{2+} in the presence of GO as a function of EGFP-CaM concentration (**Figure 3.2**). Notably, the fluorescence images of the PFP/EGFP-CaM in the presence of GO with and without Ca^{2+} under UV light show the color change from green to blue upon Ca^{2+}-binding (Figure 3.1e). In the control experiments, emission spectra of EGFP-CaM and PFP with and without GO as a function of Ca^{2+} concentrations were also measured (**Figure 3.3**). The FRET results show the signal amplification by GO-PFP hybrid probe for detecting Ca^{2+} induced conformation changes of calmodulin. The strategy of "pre-mixing" or "post-mixing" were studied to illustrate the each other interactions in our system. As shown in **Figure 3.4**, when EGFP-CaM and EGFP-CaM/Ca^{2+} was firstly mixed with PFP respectively and then GO was added, the FRET ratio values shows slight difference. Similarly, when PFP was firstly mixed with GO and then with EGFP-CaM and EGFP-CaM/Ca^{2+}, the fluorescence of PFP was quenched by GO greatly and the FRET ratio values illustrate no obvious changes as well. Therefore, in our protocol, EGFP-CaM and EGFP-CaM/Ca^{2+} must firstly assemble with GO respectively and then mix with PFP as illustrated in Scheme 3.1.

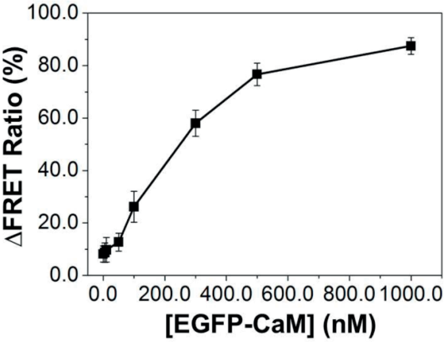

Figure 3.2. ΔFRET ratio of the PFP/EGFP-CaM in the presence of GO as a function of EGFP-CaM concentration. Fluorescence emission ratio of $I_{510\ nm}/I_{420\ nm}$ of the PFP/EGFP-CaM with and without Ca^{2+} were defined as R and R_0, respectively, and ΔFRET ratio is equal to $(R_0 - R)/R_0 \times 100\,\%$. [GO] = 25.0 µg/mL, [$Ca^{2+}$] = 1.0 mM, [PFP] = 7.5 µM in repeat units (RUs), [EGFP-CaM] = 0–1.0 µM, Measurements were performed in HEPES buffer solution (20.0 mM, pH 7.4). The excitation wavelength was 375 nm. Values represent means ± standard deviation of three separate experiments. Error bars represent standard deviations of data from three separate measurements.

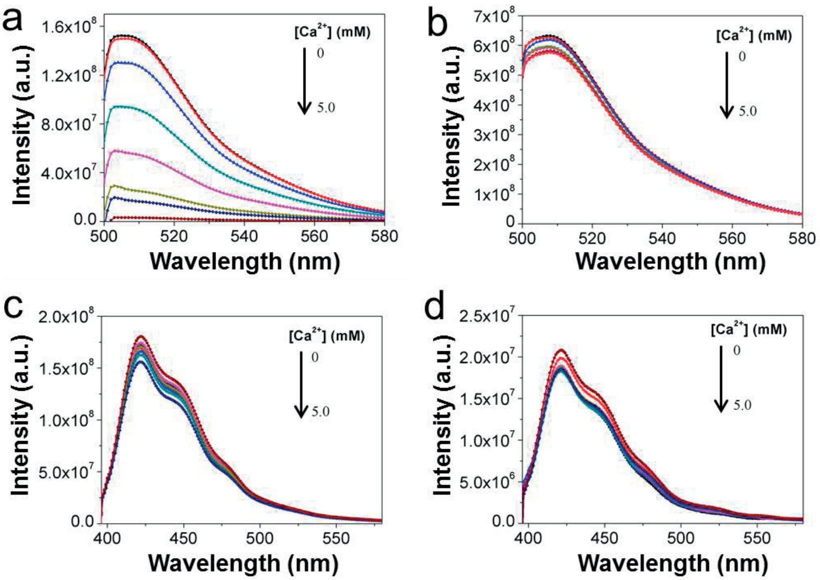

Figure 3.3. (a) Emission spectra of EGFP-CaM in the presence of GO as a function of Ca^{2+} concentrations. (b) Emission spectra of EGFP-CaM with successive addition of Ca^{2+}. (c) Emission spectra of PFP versus different concentrations of Ca^{2+}. (d) Emission spectra of PFP with GO versus different concentrations of Ca^{2+}. [GO] = 25.0 µg/mL, [EGFP-CaM] = 1.0 µM, [PFP] = 7.5 µM in repeat units (RUs), [Ca^{2+}] = 0 ~ 5.0 mM. Measurements were performed in HEPES buffer solution (20.0 mM, pH 7.4). The excitation wavelength was 480 nm for (a) and (b), 375 nm for (c) and (d).

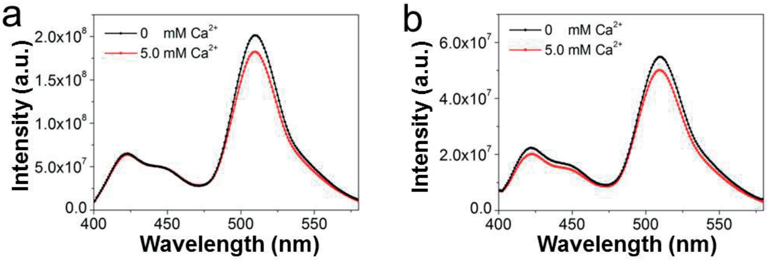

Figure 3.4. Fluorescence emission spectra of the PFP/EGFP-CaM in the presence of GO with and without Ca^{2+} by premixing EGFP-CaM and EGFP-CaM/Ca^{2+} with PFP (a) and premixing PFP with GO (b). [GO] = 25.0 µg/mL, [EGFP-CaM] = 1.0 µM, [PFP] = 7.5 µM in repeat units (RUs), [Ca^{2+}] = 0 ~ 5.0 mM. Measurements were performed in HEPES buffer solution (20.0 mM, pH 7.4). The excitation wavelength wss 375 nm.

3.2.2 Mechanism study of calmodulin sensing

To obtain further insight into the biosensing mechanism for CaM, the interactions of EGFP-CaM with GO were studied by phase contrast and fluorescence microscopy, as well as by scanning electron microscopy (SEM). As shown in **Figure 3.5**, EGFP-CaM/Ca^{2+} forms aggregates with GO, exhibiting bright fluorescence (Figure 3.5b), however, there was no obvious aggregation for apoEGFP-CaM in the presence of GO and little fluoresence can be observed (Figure 3.5a), which illustrates more EGFP-CaM/Ca^{2+} were absorbed on the surface of GO in comparison with apoEGFP-CaM. The SEM images indicate that the apoEGFP-CaM/GO complex has a regular and smooth surface (Figure 3.5c, left). Upon Ca^{2+}-binding, abundant absorption of EGFP-CaM/Ca^{2+} leads the surface of GO to become irregular, coarse and wrinkled (Figure 3.5c, right). Because Ca^{2+}-binding induces the con-

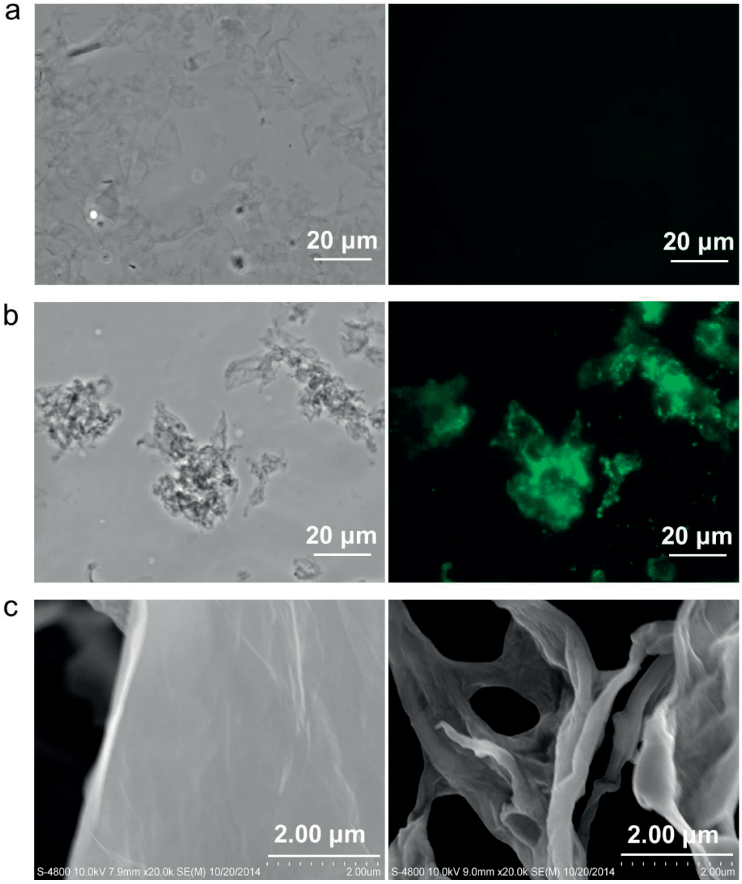

Figure 3.5. Phase contrast bright-field images and fluorescence images of EGFP-CaM/GO (a) and EGFP-CaM/Ca^{2+}/GO (b). Left: phase contrast bright-field images. Right: fluorescence images. Phase contrast images were taken at 20 ms exposure time and the fluorescence images were taken at 200 ms exposure time under EGFP filters. The false color of EGFP is green and the type of light filter is D470/40 nm exciter, 495 nm beamsplitter, and D525/50 nm emitter. The magnification of objective lens is 60×. (c) SEM images of EGFP-CaM/GO (left) and EGFP-CaM/Ca^{2+}/GO (right) were observed at an accelerating voltage of 10.0 kV.

formation of CaM to changes from the closed configuration to the open one, exposing more hydrophobic and less negatively charge surface, there is stronger binding of EGFP-CaM/Ca^{2+} with GO relative to that of apoEGFP-CaM. In addition, the SEM images of EGFP-CaM/Ca^{2+}/GO and EGFP-CaM/GO in the presence of PFP were also checked (**Figure 3.6**), which indicates that the former triggers the formation of larger aggregates. Moreover, the assembly of EGFP-CaM with GO in the presence and absence of Ca^{2+} ions was also studied by atomic force microscopy (AFM). As shown in **Figure 3.7**, EGFP-CaM/GO forms well-dispersed nanosheets with a topographic height of ~1.5 nm which is similar to that of single layered GO, and Ca^{2+}-binding induces large aggregates with undulating morphology and a topographic height of ~50 nm. Furthermore, ζ potentials of EGFP-CaM with and without Ca^{2+} ions were examined in HEPES buffer. **Table 3.1** demonstrates that the surface charges of EGFP-CaM became less when binding with Ca^{2+} ions. These results show that the EGFP-CaM/Ca^{2+} can be assembled with GO tightly with stronger hydrophobic interaction and weaker electrostatic repulsion, which induces different distance from PFP to EGFP-CaM/Ca^{2+} and apoEGFP-CaM, leading to different FRET efficiency for sensing CaM.

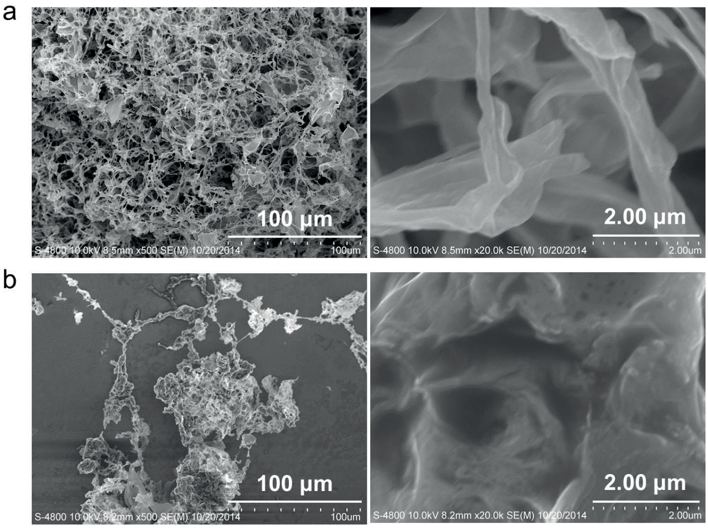

Figure 3.6. (a) Lower-magnification (left) and higher-magnification (right) SEM images of EGFP-CaM/GO in the presence of PFP. (b) Lower-magnification (left) and higher-magnification (right) SEM images of EGFP-CaM/Ca^{2+}/GO in the presence of PFP. The accelerating voltage was 10.0 kV.

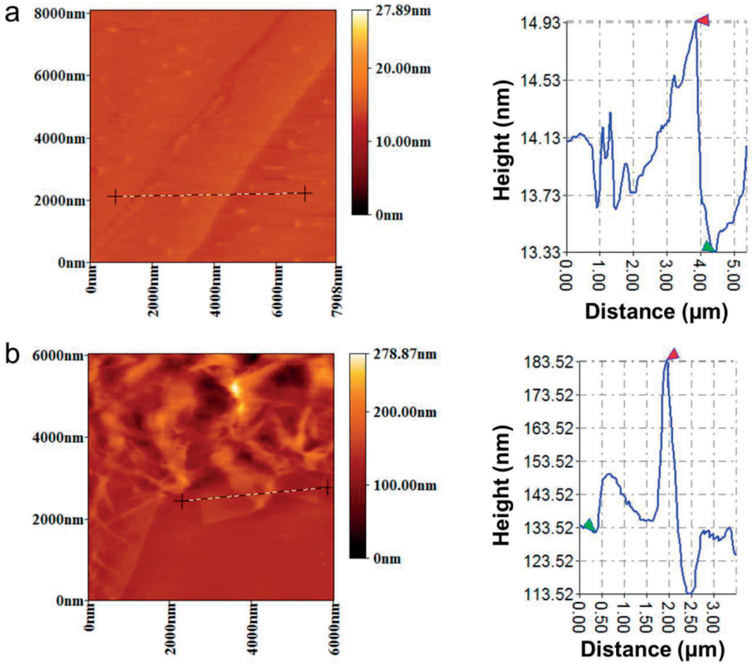

Figure 3.7. Atomic force microscopic images of EGFP-CaM/GO (a) and EGFP-CaM/Ca^{2+}/GO (b). The line profile of the assembly shown in (a) and (b) are represented in the right, respectively.

Table 3.1. ζ Potentials of CaM, EGFP-CaM, CaM/Ca^{2+}, EGFP-CaM/Ca^{2+}, PFP, and GO in HEPES buffer (20.0 mM, pH 7.4)

	ζ Potentials (mV)
CaM	-5.57
EGFP-CaM	-5.93
Ca^{2+}/CaM	-3.30
Ca^{2+}/EGFP-CaM	-2.33
PFP	12.70
GO	-35.13

3.2.3 Reversibility assay of Ca^{2+}-controlled assembly

To demonstrate the reversible assembly of EGFP-CaM with GO, EGTA (Ethylene glycol-bis(2-aminoethylether)-*N,N,N′,N′*-tetraacetic acid) was used as a conductor to cycling Ca^{2+} ions concentration. **Figure 3.8**a shows that the FRET efficiency from PFP to EGFP was significantly quenched with Ca^{2+}-binding. However, after introduction of EGTA to chelate the Ca^{2+} ions subtotally, the FRET signal was recovered, indicating the disassembly of EGFP-CaM from GO. Moreover, the FRET ratio values of $I_{510\ nm}/I_{420\ nm}$ of the PFP/EGFP-CaM in the presence of GO versus different concentrations of Ca^{2+} upon cycling Ca^{2+} were also examined. As shown in Figure 3.8b, it exhibits excellent circulatory change versus the concentrations of Ca^{2+} ions between 0 and 1.0 mM, indicating that the assembly of EGFP-CaM with GO was controlled by Ca^{2+} ions quantitatively and reversibly.

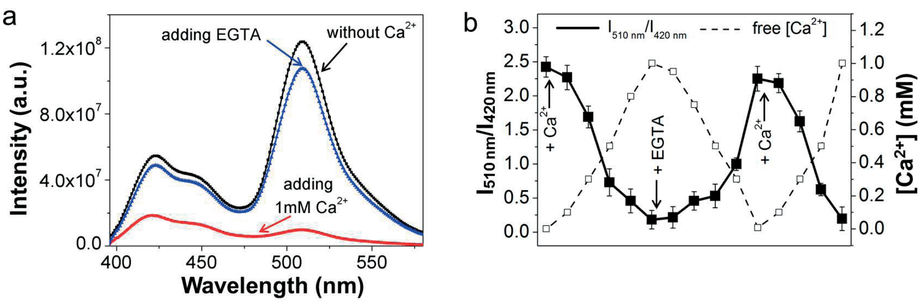

Figure 3.8. (a) Fluorescence emission spectra of the PFP/EGFP-CaM in the presence of GO upon adding Ca^{2+} and EGTA in HEPES buffer solution. (b) Fluorescence emission ratio of $I_{510\ nm}/I_{420\ nm}$ of the PFP/EGFP-CaM in the presence of GO versus different concentrations of Ca^{2+} upon cycling Ca^{2+}. Solid line represents the FRET ratio values of $I_{510\ nm}/I_{420\ nm}$ and dashed line represents the concentration of Ca^{2+}. [GO] = 25.0 µg/mL, [EGFP-CaM] = 1.0 µM, [PFP] = 7.5 µM in repeat units (RUs), $[Ca^{2+}]$ = 0 ~ 1.0 mM. Measurements were performed in HEPES buffer solution (20.0 mM, pH 7.4). The excitation wavelength was 375 nm.

3.2.4 Detection of CaM binding to target peptide

In order to imitate the conformation change of CaM binding to target peptide in vivo, the 577 to 602 residues of skeletal myosin light-chain kinase called M13 was linked to the C-terminus of EGFP-CaM to obtain the hybrid protein of EGFP-CaM-M13.[59,60] Interestingly, fluorescence emission spectra of the PFP/EGFP-CaM-M13 in the presence of GO shows similar changes to that of EGFP-CaM upon binding with Ca^{2+} ions (**Figure 3.9**a). The curves of FRET ratio values of $I_{510\ nm}/I_{420\ nm}$ versus different concentrations of Ca^{2+} ions for EGFP-CaM-M13 were also similar to that of EGFP-CaM (Figure 3.9b). Therefore, GO-PFP hybrid probe can be applied to sensing the conformation changes of CaM binding to target peptide with FRET strategy. Moreover, the binding assay of EGFP-CaM-M13 with GO by phase contrast and fluorescence microscopy (**Figure 3.10**) and the reversible assembly of EGFP-CaM-M13 with GO controlled by Ca^{2+} ions (**Figure 3.11**) were detected as well.

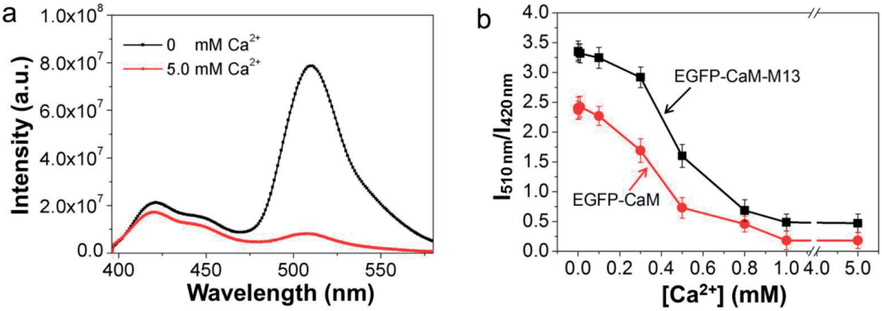

Figure 3.9. (a) Fluorescence emission spectra of the PFP/EGFP-CaM-M13 in the presence of GO with and without Ca^{2+}. (b) Fluorescence emission ratio of $I_{510 nm}/I_{420 nm}$ of the PFP/EGFP-CaM and PFP/EGFP-CaM-M13 in the presence of GO as a function of Ca^{2+} concentrations. [GO] = 25.0 µg/mL, [EGFP-CaM] = [EGFP-CaM-M13] = 1.0 µM, [PFP] = 7.5 µM in repeat units (RUs), [Ca^{2+}] = 0 ~ 5.0 mM. Measurements were performed in HEPES buffer solution (20.0 mM, pH 7.4). The excitation wavelength was 375 nm.

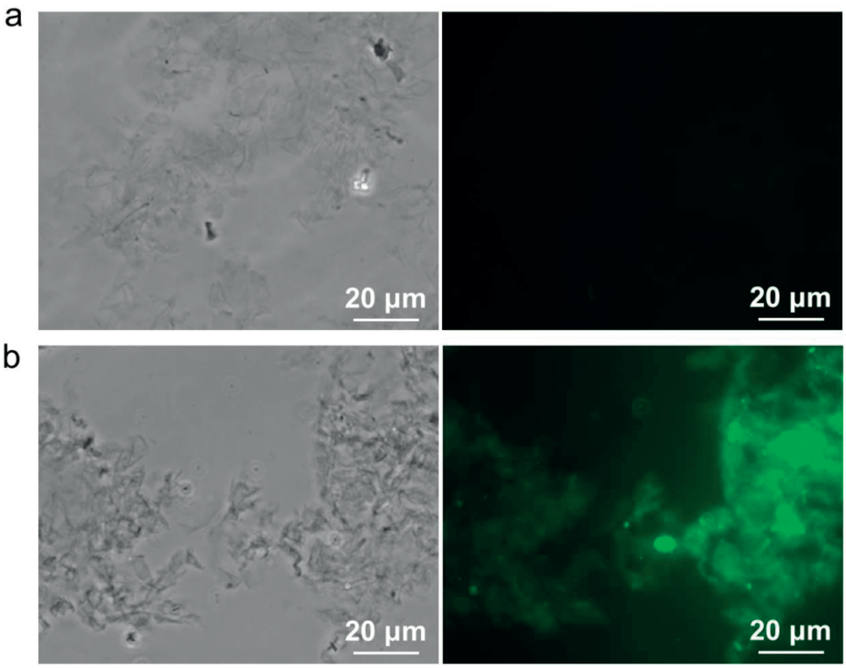

Figure 3.10. Phase contrast bright-field images and fluorescence image of EGFP-CaM-M13/GO (a) and EGFP-CaM-M13/Ca^{2+}/GO (b). Left: phase contrast bright-field images. Right: fluorescence images. Phase contrast images were taken at 20 ms exposure time and the fluorescence images were taken at 200 ms exposure time under EGFP filters. The false color of EGFP is green and the type of light filter is D470/40 nm exciter, 495 nm beamsplitter, and D525/50 nm emitter. The magnification of objective lens is 60 ×.

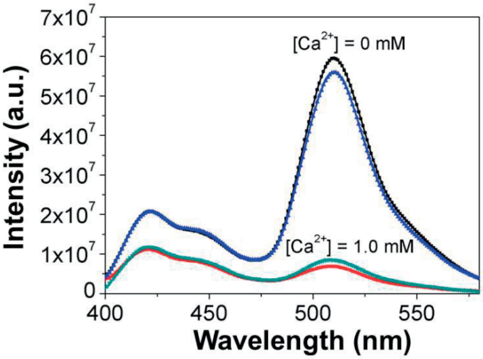

Figure 3.11. Fluorescence emission spectra of the PFP/EGFP-CaM-M13 in the presence of GO upon cycling the Ca^{2+} between 0 and 1.0 mM with Ca^{2+} and EGTA in HEPES buffer solution (20.0 mM, pH 7.4). [GO] = 25.0 µg/mL, [EGFP-CaM-M13] = 1.0 µM, [PFP] = 7.5 µM in repeat units (RUs). The excitation wavelength was 375 nm.

3.3 Conclusion

In summary, we have demonstrated a graphene oxide-cationic conjugated polymer hybrid probe for sensing the conformation transition of CaM with high signal-to-noise ratio. This new, simple, visualized and cost-effective assay has several significant features. First, the assembly of EGFP-CaM with GO is dominated by the electrostatic and hydrophobic interactions, without any covalent linkage of chemical ligands, which reduces complicated synthesis procedures. Second, the assembly of EGFP-CaM with GO is quantitatively and reversiblly controlled by Ca^{2+} ions. Third, the GO-PFP hybrid probe can be workable not only for calmodulin but also for calmodulin binding to target peptide which imitates the transformation *in vivo*. Furthermore, the transition of calmodulin is directly visualized with naked-eye by the fluorescence color changes under UV light. Thus, GO-PFP based assay for calmodulin by applying FRET technique exhibits high potential as diagnostic materials for sensing conformation changes in biomolecular process.

3.4 Experimental Section

Materials and Reagents

PFP was prepared according to a literature procedure.[54–57] Graphene oxide was prepared from natural graphitic powder according to Hummer's method and exfoliated into GO by sonication in water.[61,62] Graphite powder, sulfuric acid, hydrogen peroxide, potassium permanganate, potassium persulfate and phosphorus pentoxide were purchased from

Tianjin Guangfu Ltd.. Standard $CaCl_2$ (1.0 M), EGTA, HEPES and 96 well were purchased from Sigma. The others were obtained from Aladdin, Acros, or Alfa-Aesar and used as received. All solutions were prepared with Milli-Q water.

Characterizations of GO

As shown in **Figure 3.12**, the GO sheets were mostly single layered (topographic height ~1.4 nm, similar to earlier studies) and about 6000 nm in lateral width according to atomic force microscopy (AFM) characterization. The XPS spectra of the GO confirmed the presence of C, O and the carbon-to oxygen (C/O) atomic ratio is 2.8.

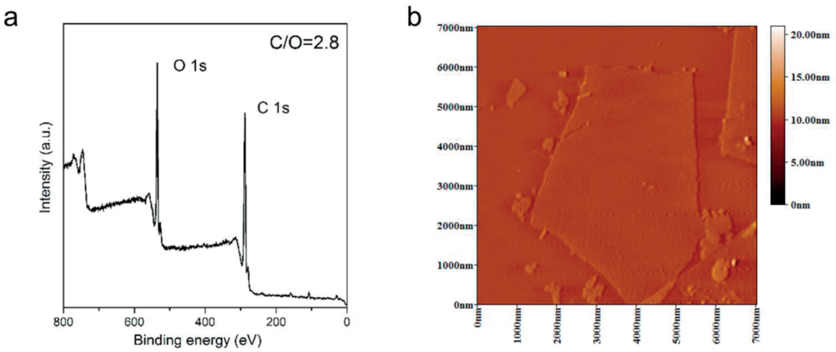

Figure 3.12. XPS spectra (a) and AFM image (b) of GO.

Instruments

Fluorescence measurements were measured on a SpectraMax i3 Multi-mode microplate detection platform (Molecular Devices, USA) with a Xenon lamp excitation source. Phase contrast bright-field and fluorescence images were taken on a fluorescence microscope (Nikon TiU) with a mercury lamp (100 W) as light source. The excitation wavelength was 470/40 nm for EGFP. Photographs were taken with a Canon EOS-600D digital camera. The morphologies of the EGFP-CaM on GO were observed on a JEOL JSM 4800F field-emission scanning electron microscope. AFM images were taken by CSPM 5000 scanning probe microscope in tapping mode. XPS data were taken by Perkin-Elmer PHI 1600 spectrometer. ζ potentials experiments were carried out on Nano-ZS90 (Malvern Instruments, UK).

EGFP-CaM and EGFP-CaM-M13 preparation

The cDNA of the EGFP was amplified by the polymerase chain reaction (PCR) with a sense primer containing Nde I site and a reverse primer containing Xho I site. M13 was synthesized by Takara Ltd.. The fusion DNA fragments of EGFP-CaM and EGFP-CaM-M13 were cloned into the pCold II plasmid, expressed in *Escherichia coli* (BL21 strain), purified, dialyzed and quantified finally according to a reported method.[63]

Preparation of HEPES buffer

For zero-Ca^{2+} buffer, the solution contained 20.0 mM HEPES and 20.0 µM EGTA was adjusted to pH 7.4 with NaOH. For high-Ca^{2+} buffer, the solution contained 20.0 mM HEPES, 20.0 µM EGTA and 100.0 mM $CaCl_2$ was adjusted to pH 7.4 with NaOH. Different concentrations of free Ca^{2+} solutions were made by mixing zero-Ca^{2+} and high-Ca^{2+} solutions according to the Ca-EGTA calculator (http://www.stanford.edu/~cpatton/CaEGTA -NIST. htm).

Detection of the conformation changes of calmodulin

5.0 µL of 40.0 µM EGFP-CaM stock solution was added in 200 µL of HEPES buffer with different concentrations of free Ca^{2+} (0 ~ 5.0 mM) respectively and incubated for 10 min, and then 10.0 µL of 0.5 mg/mL GO was added into the well and mixed gently. After the mixtures were incubated for 30 min at room temperature, PFP (7.5 µM in repeat units (RUs)) was added and incubated for 10 min. These samples were measured the fluorescence spectra in 96 well microplate through a multi-mode detection platform. The excitation wavelength was 375 nm.

Morphology study of EGFP-CaM with GO

25.0 µL of 40.0 µM EGFP-CaM stock solution was added in 1.0 mL of HEPES buffer with 0 mM and 5.0 mM Ca^{2+} respectively and incubated for 10 min, then 25.0 µg/mL GO was added into the well and mixed gently. After the mixtures were incubated for 30 min at room temperature, the samples was centrifuged for 15 min at 8000r, 4°C, and the supernate was removed. Then, the precipitates were resuspended in 20 µL sterile water. Phase contrast bright-field and fluorescence images were taken on a fluorescence microscope. The phase contrast images were taken at 20 ms and the fluorescence images were taken at 200 ms under EGFP filters. The false color of EGFP is green and the type of light filter is D470/40 nm exciter, 495 nm beamsplitter, and D525/50 nm emitter. The magnification of objective lens is 60 ×. SEM images were observed on a JEOL JSM 4800F field-emission scanning electron microscope, at an accelerating voltage of 10.0 kV.

Reversibility aassay of assembly of EGFP-CaM with GO

Ca^{2+} ions ($[Ca^{2+}] = 0–1.0$ mM) was added successively to a solution with EGFP-CaM (1.0 µM) and GO (25.0 µg/mL) in zero-Ca^{2+} buffer. When the concentration of Ca^{2+} increases to 1.0 mM, different volume of 10.0 mM EGTA were dropped into the wells to decrease the concentration of Ca^{2+}, then Ca^{2+} ions was recovered through added high-Ca^{2+} buffer. For cycling Ca^{2+} ions, the accurate concentration of Ca^{2+} was calculated according to the Ca-EGTA calculator, and the measurement of fluorescence spectra was same to the previous procedure.

Assay for detection limit of the system

To 200 µL of HEPES buffer with and without Ca^{2+} (1.0 mM) were added different concentrations of EGFP-CaM (0 ~ 1.0 µM) respectively and incubated for 10 min, and then 10.0 µL of 0.5 mg/mL GO was added into the well and mixed gently. After the mixtures were incubated for 30 min at room temperature, PFP (7.5 µM in repeat units (RUs)) was added and incubated for 10 min. The fluorescence spectra were measured in 96 well microplates by applying a multi-mode detection platform. The excitation wavelength is 375 nm. Fluorescence emission ratio of $I_{510\ nm}/I_{420\ nm}$ of the PFP/EGFP-CaM with and without Ca^{2+} were calculated and defined as R and R_0, respectively, and ΔFRET ratio is equal to $(R_0 - R)/R_0 \times 100\%$.

An approximate cost of per analysis

a). Graphene oxide (GO) was prepared from natural graphite powders. The product costs only ~ $50 per gram referring to our laboratory-scale preparation. Per analysis used ~ 5.0 µg GO and the cost of per analysis is ~ 0.025 cent.

b). PFP was prepared according to a literature procedure. The cost of 1.0 g of PFP is ~ $80. Per analysis used ~ 1.0 µg PFP and the cost of per analysis is ~ 0.008 cent.

In summary, the cost of per analysis is ~ 0.033 cent (the cost of the used solvent is negligible). Therefore, this is a cost-effective assay.

3.5 References

(1) Chin, D.; Means, A. R. *Trends in cell biol.* **2000**, *10*, 322.

(2) Clapham, D. E. *Cell* **2007**, *131*, 1047.

(3) Ogawa, Y.; Tanokura, M. *J. Biochem.* **1984**, *95*, 19.

(4) Meador, W. E.; Means, A. R.; Quiocho, F. A. *Science* **1993**, *262*, 1718.

(5) Kuboniwa, H.; Tjandra, N.; Grzesiek, S.; Ren, H.; Klee, C. B.; Bax, A. *Nat. Struct. Biol.* **1995**, *2*, 768.

(6) Ikura, M.; Clore, G. M.; Gronenborn, A. M.; Zhu, G.; Klee, C. B.; Bax, A. *Science* **1992**, *256*, 632.

(7) Zhang, M.; Tanaka, T.; Ikura, M. *Nat. Struct. Biol.* **1995**, *2*, 758.

(8) Babu, Y. S.; Bugg, C. E.; Cook, W. J. *J. Mol. Biol.* **1988**, *204*, 191.

(9) Sun, H.; Yin, D.; Squier, T. C. *Biochemistry* **1999**, *38*, 12266.

(10) Finn, B. E.; Forsen, S. *Structure* **1995**, *3*, 7.

(11) Vetter, S. W.; Leclerc, E. *Eur. J. Biochem.* **2003**, *270*, 404.

(12) Slaughter, B. D.; Unruh, J. R.; Allen, M. W.; Bieber Urbauer, R. J.; Johnson, C. K. *Biochemistry* **2005**, *44*, 3694.

(13) Novoselov, K. S.; Geim, A. K.; Morozov, S. V.; Jiang, D.; Zhang, Y.; Dubonos, S. V.; Grigorieva, I. V.; Firsov, A. A. *Science* **2004**, *306*, 666.

(14) Huang, X.; Qi, X.; Boey, F.; Zhang, H. *Chem. Soc. Rev.* **2012**, *41*, 666.

(15) Pumera, M. *Mater. Today* **2011**, *14*, 308.

(16) Yang, K.; Feng, L.; Shi, X.; Liu, Z. *Chem. Soc. Rev.* **2013**, *42*, 530.

(17) Kostarelos, K.; Novoselov, K. S. *Science* **2014**, *344*, 261.

(18) Kim, K. S.; Zhao, Y.; Jang, H.; Lee, S. Y.; Kim, J. M.; Kim, K. S.; Ahn, J.-H.; Kim, P.; Choi, J.-Y.; Hong, B. H. *Nature* **2009**, *457*, 706.

(19) Loh, K. P.; Bao, Q.; Eda, G.; Chhowalla, M. *Nat. Chem.* **2010**, *2*, 1015.

(20) Wang, Y.; Li, Z.; Wang, J.; Li, J.; Lin, Y. *Trends Biotechnol.* **2011**, *29*, 205.

(21) Dreyer, D. R.; Park, S.; Bielawski, C. W.; Ruoff, R. S. *Chem. Soc. Rev.* **2010**, *39*, 228.

(22) Kim, J.; Cote, L. J.; Kim, F.; Yuan, W.; Shull, K. R.; Huang, J. *J. Am. Chem. Soc.* **2010**, *132*, 8180.

(23) Chung, C.; Kim, Y.-K.; Shin, D.; Ryoo, S.-R.; Hong, B. H.; Min, D.-H. *Acc. Chem. Res.* **2013**, *46*, 2211.

(24) Deng, X.; Tang, H.; Jiang, J. *Anal. Bioanal. Chem.* **2014**, *406*, 6903.

(25) Dong, H.; Gao, W.; Yan, F.; Ji, H.; Ju, H. *Anal. Chem.* **2010**, *82*, 5511.

(26) Qi, J.; Lv, W.; Zhang, G.; Li, Y.; Zhang, G.; Zhang, F.; Fan, X. *Nanoscale* **2013**, *5*, 6275.

(27) Wang, Q.; Xu, N.; Lei, J.; Ju, H. *Chem. Commun.* **2014**, *50*, 6714.

(28) Morales-Narváez, E.; Merkoçi, A. *Adv. Mater.* **2012**, *24*, 3298.

(29) Liu, X.; Wang, F.; Aizen, R.; Yehezkeli, O.; Willner, I. *J. Am. Chem. Soc.* **2013**, *135*, 11832.

(30) Lu, C.-H.; Yang, H.-H.; Zhu, C.-L.; Chen, X.; Chen, G.-N. *Angew. Chem., Int. Ed.* **2009**, *121*, 4879.

(31) Li, X.; Ma, K.; Zhu, S.; Yao, S.; Liu, Z.; Xu, B.; Yang, B.; Tian, W. *Anal. Chem.* **2013**, *86*, 298.

(32) Lu, Z.; Zhang, L.; Deng, Y.; Li, S.; He, N. *Nanoscale* **2012**, *4*, 5840.

(33) Ryoo, S.-R.; Lee, J.; Yeo, J.; Na, H.-K.; Kim, Y.-K.; Jang, H.; Lee, J. H.; Han, S. W.; Lee, Y.; Kim, V. N. *ACS Nano* **2013**, *7*, 5882.

(34) Chang, H.; Tang, L.; Wang, Y.; Jiang, J.; Li, J. *Anal. Chem.* **2010**, *82*, 2341.

(35) Jang, H.; Kim, Y. K.; Kwon, H. M.; Yeo, W. S.; Kim, D. E.; Min, D. H. *Angew. Chem., Int. Ed.* **2010**, *122*, 5839.

(36) Pu, Y.; Zhu, Z.; Han, D.; Liu, H.; Liu, J.; Liao, J.; Zhang, K.; Tan, W. *Analyst* **2011**, *136*, 4138.

(37) He, Y.; Wang, Z.-G.; Tang, H.-W.; Pang, D.-W. *Biosen. and Bioelectron.* **2011**, *29*, 76.

(38) Liu, S.; Zeng, T. H.; Hofmann, M.; Burcombe, E.; Wei, J.; Jiang, R.; Kong, J.; Chen, Y. *ACS Nano* **2011**, *5*, 6971.

(39) Li, J.; Wu, L.-J.; Guo, S.-S.; Fu, H.-E.; Chen, G.-N.; Yang, H.-H. *Nanoscale* **2013**, *5*, 619.

(40) Wang, L.; Pu, K.-Y.; Li, J.; Qi, X.; Li, H.; Zhang, H.; Fan, C.; Liu, B. *Adv. Mater.* **2011**, *23*, 4386.

(41) Xu, Q.; Cheng, H.; Lehr, J.; Patil, A. V.; Davis, J. J. *Anal. Chem.* **2014**, *87*, 346.

(42) Wang, F.; Liu, Z.; Wang, B.; Feng, L.; Liu, L.; Lv, F.; Wang, Y.; Wang, S. *Angew. Chem., Int. Ed.* **2014**, *126*, 434.

(43) Feng, L. H.; Zhu, C. L.; Yuan, H. X.; Liu, L. B.; Lv, F. T.; Wang, S. *Chem. Soc. Rev.* **2013**, *42*, 6620.

(44) Xing, C.; Yuan, H.; Xu, S.; An, H.; Niu, R.; Zhan, Y. *ACS Appl. Mater. Interfaces* **2014**, *6*, 9601.

(45) Rochat, S.; Swager, T. M. *J. Am. Chem. Soc.* **2013**, *135*, 17703.

(46) Herland, A.; Nilsson, K. P.; Olsson, J. D.; Hammarstrom, P.; Konradsson, P.; Inganas, O. *J. Am. Chem. Soc.* **2005**, *127*, 2317.

(47) Nilsson, K. P. R.; Inganas, O. *Macromolecules* **2004**, *37*, 9109.

(48) Nystrom, S.; Psonka-Antonczyk, K. M.; Ellingsen, P. G.; Johansson, L. B.; Reitan, N.; Handrick, S.; Prokop, S.; Heppner, F. L.; Wegenast-Braun, B. M.; Jucker, M.; Lindgren, M.; Stokke, B. T.; Hammarstrom, P.; Nilsson, K. P. *ACS Chem. Biol.* **2013**, *8*, 1128.

(49) Yuan, H.; Xing, C.; An, H.; Niu, R.; Li, R.; Yan, W.; Zhan, Y. *ACS Appl. Mater. Interfaces* **2014**, *6*, 14790.

(50) Xing, X.-J.; Zhou, Y.; Liu, X.-G.; Tang, H.-W.; Pang, D.-W. *Analyst* **2013**, *138*, 6301.

(51) Xing, X.-J.; Liu, X.-G.; He, Y.; Lin, Y.; Zhang, C.-L.; Tang, H.-W.; Pang, D.-W. *Biomacromolecules* **2012**, *14*, 117.

(52) Geng, J.; Zhou, L.; Liu, B. *Chem. Commun.* **2013**, *49*, 4818.

(53) Wang, C.; Tang, Y.; Liu, Y.; Guo, Y. *Anal. Chem.* **2014**, *86*, 6433.

(54) Liu, B.; Wang, S.; Bazan, G. C.; Mikhailovsky, A. *J. Am. Chem. Soc.* **2003**, *125*, 13306.

(55) Xing, C.; Liu, L.; Shi, Z.; Li, Y.; Wang, S. *Adv. Funct. Mater.* **2010**, *20*, 2175.

(56) Pu, F.; Hu, D.; Ren, J.; Wang, S.; Qu, X. *Langmuir* **2010**, *26*, 4540.

(57) Duan, X.; Liu, L.; Feng, X.; Wang, S. *Adv. Mater.* **2010**, *22*, 1602.

(58) Seamon, K. B. *Biochemistry* **1980**, *19*, 207.

(59) Miyawaki, A.; Llopis, J.; Heim, R.; McCaffery, J. M.; Adams, J. A.; Ikura, M.; Tsien, R. Y. *Nature* **1997**, *388*, 882.

(60) Truong, K.; Sawano, A.; Mizuno, H.; Hama, H.; Tong, K. I.; Mal, T. K.; Miyawaki, A.; Ikura, M. *Nat. Struct. Biol.* **2001**, *8*, 1069.

(61) Park, S.; Ruoff, R. S. *Nat. Nano* **2009**, *4*, 217.

(62) Qi, J.; Lv, W.; Zhang, G.; Zhang, F.; Fan, X. *Polym. Chem.* **2012**, *3*, 621.

(63) Arndt, K. M.; Müller, K. M. *Protein engineering protocols*; Humana Press: Totowa, N.J., 2007.

CHAPTER 4

CONJUGATED POLYMER-BASED HYBRID MATERIALS FOR TURN-ON DETECTION OF CO_2 IN PLANT PHOTOSYNTHESIS

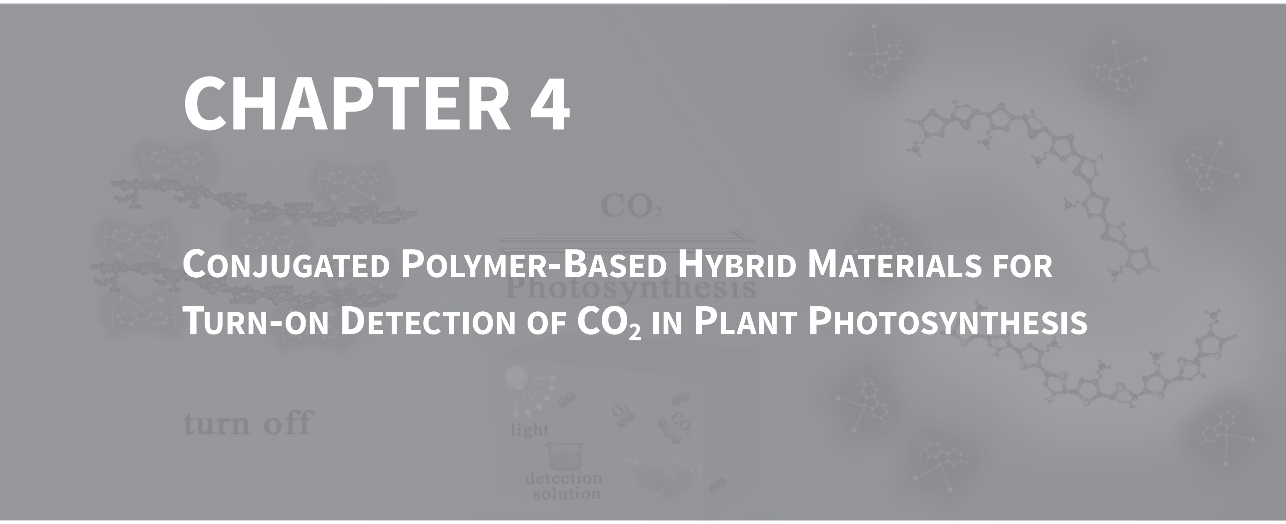

This chapter has been published in:
Yuan, H.;* Fan, Y.;* Xing, C.; Niu, R.; Chai, R.; Zhan, Y.; Qi, J.; An, H.; Xu, J., *Anal. Chem.* **2016,** *88*, 6593–6597.

*Equal contribution

Fan Y. and Niu R. are acknowledged for the synthesis and characterization of polymers. Chai R. and Dr. Qi J. performed CO_2 detection in the process of photosynthesis. Dr. Xu J. and Prof. An H. are acknowledged for discussions on the interpretation of the results. Prof. Xing C. and Prof. Zhan Y. supervised the project.

Abstract

Detection of carbon dioxide (CO_2) is of fundamental importance in diverse applications ranging from environmental analysis to agricultural production. In this work, a hybrid probe based on guanidinium-pendent oligofluorene (G-OF) and water-soluble conjugated polythiophene (PTP) has been developed for the turn on detection of CO_2 with low background signal, taking advantage of the efficient fluorescence quenching of the tight aggregate of G-OF/PTP. In the presence of CO_2, the electrostatic repulsion between G-OF and PTP can be effectively enhanced through protonation of the side chains, leading to the disaggregation and thus the "turn-on" fluorescence. The strategy allows for the light-up visible detection of CO_2 with high sensitivity. Importantly, this system is capable of sensitively monitoring the concentration changes of CO_2 in the process of the photosynthesis, which represents a concept to monitor the photosynthesis based on water-soluble conjugated polymers.

4.1 Introduction

Carbon dioxide (CO_2) is a greenhouse gas contributing immeasurably to the global climate change and acts as an asphyxiant with the maximal acceptable concentration defined as 3.0 %.[1–3] CO_2 also plays an essential role in plant photosynthesis. 90–95 % of the dry weight of plants derives from the assimilation of CO_2 during photosynthesis.[4,5] In this context, monitoring the photosynthesis of vegetation is not only crucial for raising the productivity of agriculture, but also important for the better fixation of CO_2. Therefore, the detection of CO_2, in particular during the process of photosynthesis, is of great significance for global warming monitoring,[6,7] medical diagnosis[8,9] and agricultural production.[10] Optical CO_2 detection methods have exhibited their advantages including convenience, low cost and fastness, over the traditional analytical methodologies such as near-infrared spectroscopy,[11] gas chromatography-mass spectrometry[12,13] and electrochemical techniques.[14] For example, several effective fluorescent probes based on aggregate-induced emission (AIE) have been recently developed for monitoring CO_2.[15–19] Yoon and co-authors realized colorimetric and fluorescent CO_2 detection by applying polydiacetylene in aqueous solution and in the solid state.[20] However, most of the established approaches have relatively high background fluorescence signal or require additional accessory molecules.[20] Moreover, to the best of our knowledge, very few examples of optical sensors have been reported to detect the changes of CO_2 in the process of photosynthesis, which is highly desirable.

Water-soluble conjugated polyelectrolytes are characterized by their delocalized π-electronic backbones and extraordinary light-harvesting capacities, exhibiting a signal amplification effect.[21–24] In the past few years, water-soluble conjugated polymers have been widely employed as an efficient platform for the detection of small molecules[25–27] and biomolecules such as DNA,[28–30] protein,[31–33] and enzymes,[34,35] with specificity and high sensitivity. They have been further developed into promising materials for broad biological applications in disease diagnosis,[36] drug screening and delivery,[37,38] cell imaging[39] and antimicrobial susceptibility testing.[40–42] Inspired by these studies, we illustrate here a fluorescent, visible and "turn-on" detection system for CO_2 in dissolved and gaseous states as well as in plant photosynthesis, by hybridizing the guanidinium-pendent oligofluorene (G-OF) and water-soluble conjugated polymer poly(3-(2'-*N, N*-di-propanoic acid-ethylamino)-2,5-thiophene) (PTP). As illustrated in **Scheme 4.1**, PTP is designed to be functionalized with one amino group and two carboxylate groups in each repeat unit, while G-OF has guanidinium groups in the side chains. In the absence of CO_2, the guanidinium group of G-OF is partly protonated and the polymer exhibits positive charges, interacting with anionic PTP by tight electrostatic and π-π stacking interactions, forming micrometer-sized supramolecularly assembled aggregates. These strong supramolecular interactions dramatically quenches (turn-off) the fluorescence of both polymers. When CO_2 is bubbled into the solution, the guanidinium groups of G-OF are completely protonated and the polymers become positively charged. At the same time, both the amino and the carboxyl groups of PTP are protonated, endows the polymer also with positive charges. Thus, the electrostatic repulsion between G-OF and PTP dominates and leads to the break of the G-OF/PTP aggregates, resulting in the fluorescence recovery of G-OF and PTP (turn-on). The system is so sensitive that it can be effectively applied to monitor the concentration changes of CO_2 in the process of plant photosynthesis, which continuously converts CO_2 into carbohydrate by the assimilation of sunlight and H_2O and converts.[43,44] The fluorescence of G-OF/PTP is gradually quenched as the plant photosynthesis is consuming the CO_2. Furthermore, the CO_2 detection can be visualized directly in view of color changes of G-OF/PTP in aqueous medium under UV light.

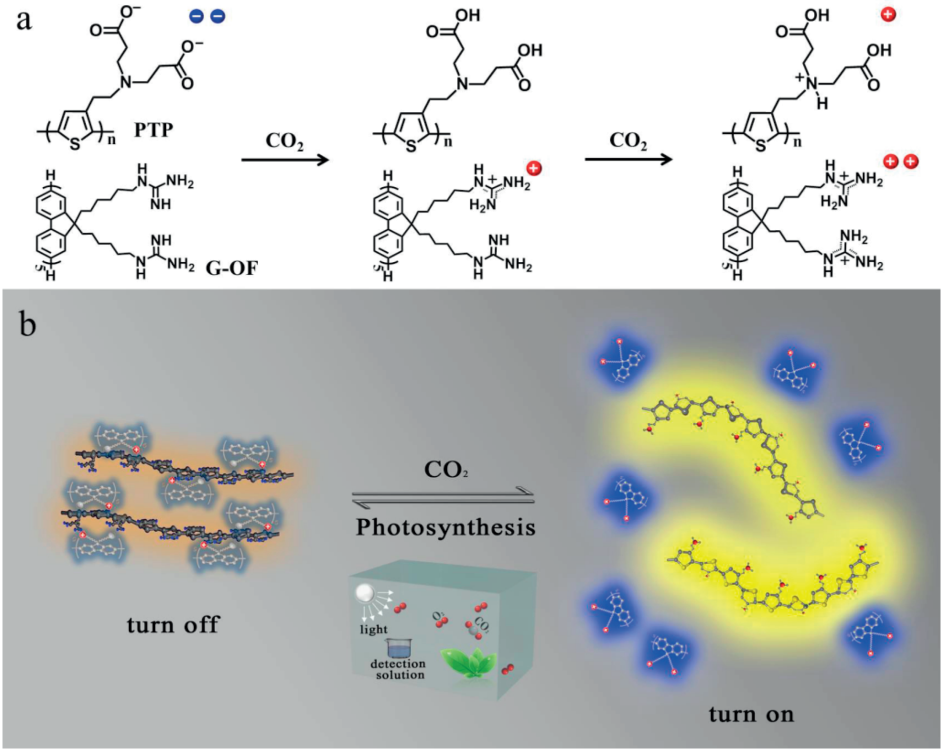

Scheme 4.1. (a) The charge changes of G-OF and PTP upon bubbling with CO_2.[a] (b) Schematic representation of G-OF/PTP hybrid probe for CO_2 detection in plant photosynthesis.[b] ([a] The charge changes of G-OF and PTP according to the different pK_a values of each side chain, the guanidinium, tertiary amine and carboxyl groups with pK_a values of 13.6, 9.54 and 2.2, respectively.[45,46b] The fluorescence of both polymers is quenched upon the formation of the tight aggregate of G-OF/PTP, but gets efficiently recovered in the presence of CO_2.)

4.2 Results and Discussion

PTP and G-OF were synthesized referring to the reported procedures.[46,47] The detection of CO_2 by the G-OF/PTP hybrid probe is based on the efficient fluorescence quenching of both polymers. G-OF emits bright blue light in aqueous solution with the fluorescence spectrum maximized at 420 nm, while PTP emits yellow fluorescence with a maximum at 560 nm. The fluorescence of G-OF ([G-OF] = 0.8 μM) was quenched upon addition of PTP ([PTP] = 0 – 875.0 nM in repeat units) in water. As shown in **Figure 4.1**a, the emission of G-OF was decreased gradually with successive addition of PTP and the fluorescence of G-OF was efficiently quenched by 97.2 % in the presence of PTP ([PTP] = 875.0 nM). The quenching efficiency was calculated by measuring the fluorescent changes of G-OF via the Stern-Volmer equation (eq 1):[48]

$$I_0/I = 1 + K_{SV}\,[Q] \qquad (1)$$

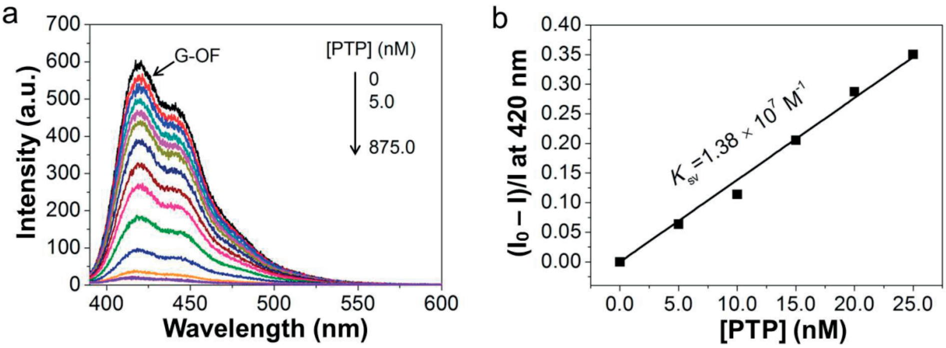

Figure 4.1. (a) Fluorescence spectra of G-OF in water with successive additions of PTP. (b) K_{SV} plot of G-OF in the presence of PTP. [G-OF] = 0.8 μM, [PTP] = 0 – 875.0 nM (in repeat units). I and I_0 represent the emission intensity of G-OF at 420 nm in the presence and absence of PTP. Measurements were performed at 4 ºC in sterile water. The excitation wavelength was 378 nm.

The Stern-Volmer constant (K_{SV}) value was deduced to be 1.38×10^7 M^{-1} from the linear Stern-Volmer plot with low concentrations of PTP (0 – 25.0 nM) (Figure 4.1b), indicating the superquenching of G-OF by PTP. The intense electrostatic and π-π stacking interactions between G-OF and PTP were attributed to drive the formation of the tight aggregation of G-OF/PTP complex, and to induce the super-quenching behaviour.

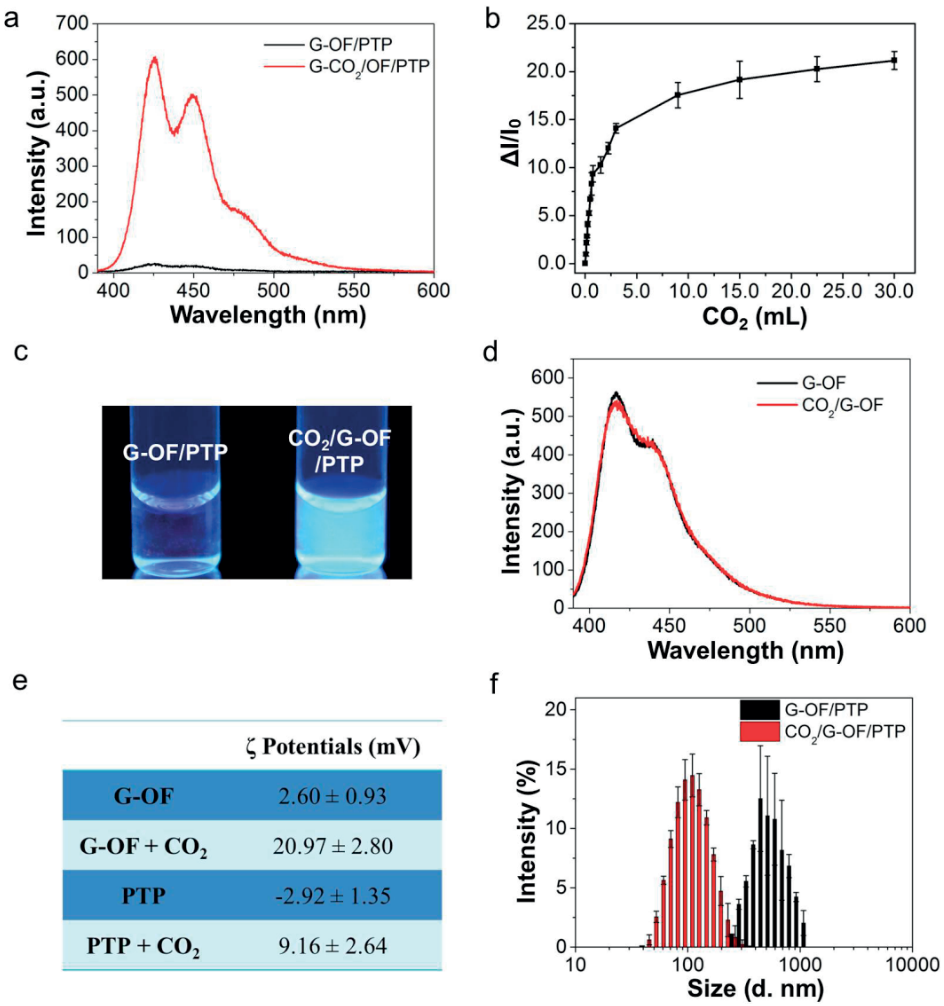

	ζ Potentials (mV)
G-OF	2.60 ± 0.93
G-OF + CO_2	20.97 ± 2.80
PTP	-2.92 ± 1.35
PTP + CO_2	9.16 ± 2.64

Figure 4.2. (a) Fluorescence spectra of G-OF in the presence of PTP with and without CO_2. (b) Fluorescence intensity of G-OF at 420 nm in the presence of PTP after bubbling with different volumes of CO_2 in water at 4 ºC. I_0 and I represent the emission intensity of G-OF at 420 nm in the presence of PTP without and with CO_2, respectively, and $\Delta I/I_0$ is equal to $(I - I_0)/I_0$. All data were presented as mean values ± standard deviation of three separate experiments. Error bars represent standard deviations of data from three separate measurements. (c) Fluorescence images of G-OF in the presence of PTP in water with and without CO_2, under UV light excitatiom (λ = 365 nm). (d) Emission spectra of G-OF in water with and without CO_2. (e) ζ Potentials of G-OF and PTP with and without CO_2 in water. (f) Size distribution histograms of G-OF in the presence of PTP with and without CO_2 resulting from dynamic light scattering measurement. [G-OF] = 0.8 µM, [PTP] = 875.0 nM (in repeat units), the bubbling volumes of CO_2 increase from 0 to 30.0 mL at a constant flow rate of 1.5 mL/min. Measurements were performed at 4 ºC in sterile water. The excitation wavelength was 378 nm.

The sensitivity of the assembled G-OF/PTP complex to CO_2 was firstly examined in the solution state, by bubbling CO_2 into the aqueous solution of G-OF in the presence of PTP, and the results are summarized in **Figure 4.2**. As shown in Figure 4.2a, the emission intensity of G-OF has been recovered by approximately 20 times after reacting with CO_2. The recovery rate is dependent on the bubbling volumes of CO_2. As shown in Figure 4.2b, the fluorescence intensity of G-OF/PTP at 420 nm increases with the amount of CO_2 bubbled and the detection limit can be as lower as 75.0 µL. Importantly, the detection of CO_2 can be directly visualized through the color changes of G-OF/PTP from dark blue to bright blue under UV irradiation upon bubbling with CO_2, as shown in the images in Figure 4.2c. Control experiments were carried out to check the effect of CO_2 on the emitting behaviors of G-OF and PTP. CO_2 was found to induce very little effect on the emission spectra of G-OF in the absence of PTP (Figure 4.2d), while the emission of PTP was decreased with the addition of CO_2. This is consistent with the working mechanism proposed in Scheme 4.1, where the net charges of PTP is decreased and the dominating inter-chain π-π stacking leads to the formation of aggregates, and results in the self-quenching of PTP, with the increasing amount of CO_2.[49]

The ζ potentials provide further evidence for the interactions between G-OF and PTP in the presence and absence of CO_2 (Figure 4.2e). ζ potentials of G-OF and PTP became more positive upon reaction with CO_2 because the guanidinium groups of G-OF and the amino and carboxylate groups of PTP became completely protonated. Additionally, the dynamic light scattering (DLS) measurements were also conducted. As shown in Figure 4.2f, the average hydrodynamic radius of G-OF/PTP aggregates is 842.2 nm, which is much larger than that in the presence of CO_2 (104.1 nm). This is a direct indication that the G-OF/PTP aggregates were separated due to the electrostatic repulsion between G-OF and PTP. In order to further study the mechanism of our system, the fluorescence recovery of the hybrid probe G-OF/PTP with other gases in water was measured. As illustrated in **Figure 4.3**, no fluorescence recovery was produced by N_2 or O_2, indicating little interference from other gases in atmosphere. Moreover, the interference of SO_2 was checked as well. As illustrated in **Figure 4.4**, the emission of G-OF/PTP can not be recovered in the presence of SO_2, possibly resulting from the total quenching of G-OF by SO_2 which is different from that in the presence of CO_2. Therefore, these results demonstrate a fluorescent, visible and turn-on detection for CO_2 with high sensitivity and selectivity.

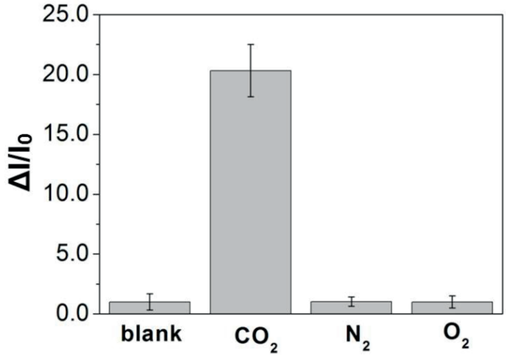

Figure 4.3. Fluorescence recovery of G-OF in the presence of PTP with various gases in water. All data were presented as mean values ± standard deviation of three separate experiments. Error bars represent standard deviations of data from three separate measurements. Measurements were performed at 4 ºC in sterile water. The excitation wavelength was 378 nm.

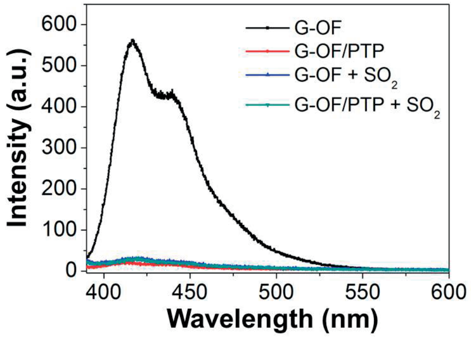

Figure 4.4. Fluorescence spectra of G-OF and G-OF/PTP with and without SO_2. [G-OF] = 0.8 µM, [PTP] = 875.0 nM (in repeat units). The excitation wavelength was 378 nm.

Taking the practicality into consideration, CO_2 is always present in the atmosphere and acts as an asphyxiant. Therefore the fluorescence spectra of the G-OF/PTP hybrid probe before and after bubbling with CO_2/N_2 with different ratios were examined. As illustrated in **Figure 4.5**, the emission was recovered gradually with the increasing ratio of CO_2 in a series of CO_2/N_2 mixtures and the detected minimum ratio of CO_2 was 1.0 % (Figure 4.5b). In practical terms, the maximal acceptable concentration was defined under 3.0 %.[3] Furthermore, the hybrid probe G-OF/PTP was also applied for solid-state sensing of CO_2. G-OF/PTP was sprayed onto a substrate of the cellulose ester film, and a dark blue to bright blue color change was observed under UV light upon exposure to CO_2 atmosphere, (**Figure 4.6**). Therefore, our probe system offers a CO_2 detection approach allows for the assessment of the asphyxial risk.

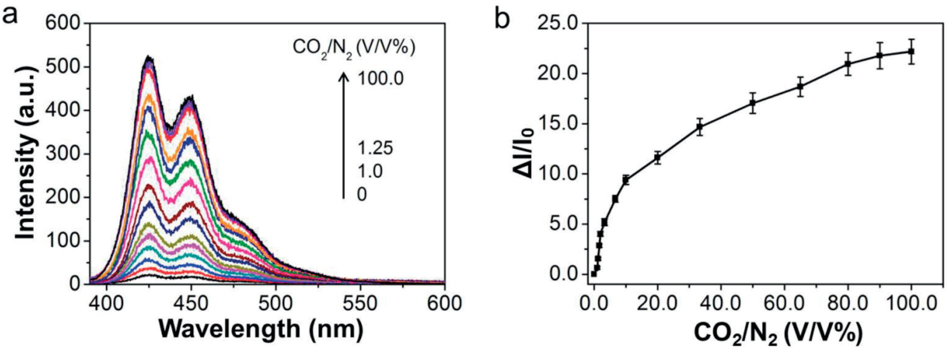

Figure 4.5. (a) Fluorescence spectra of G-OF in the presence of PTP before and after bubbling with CO_2/N_2 mixtures with different ratios for 2 minutes at a constant flow rate of 1.5 mL/min. (b) Plot of the fluorescence intensity of G-OF at 420 nm in the presence of PTP as a function of the ratio of CO_2 in CO_2/N_2 mixtures. [G-OF] = 0.8 µM, [PTP] = 875.0 nM (in repeat units), the volume ratios of CO_2/N_2 change from 0 to 100.0 %. Error bars represent standard deviations of data from three separate measurements. Measurements were performed at 4 ºC in water. The excitation wavelength was 378 nm.

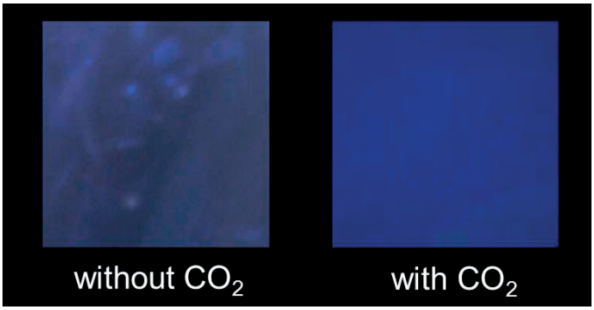

Figure 4.6. The color changes of G-OF/PTP and cellulose ester composite film with and without CO_2 atmosphere under UV light ($\lambda = 365$ nm).

Furthermore, the G-OF/PTP-based detection for CO_2 in gaseous phase was studied in confined spaces. As shown in **Figure 4.7**a, the detection solution of G-OF in water was placed in a confined chamber with CO_2 atmosphere (1.0 atm) for 12 hours, and then the emission spectra of the G-OF/PTP hybrid probe was measured. Figure 4.7b exhibits that the gaseous CO_2 induces the significant recovery of emission through the absorption to the detection solution. Additionally, the different volume ratios of CO_2/N_2 mixtures in confined spaces were also detected, and the detected minimum ratio of CO_2 was 1.0 % as well (**Figure 4.8**). In this way, the G-OF/PTP-based system allows for the detection of the gaseous CO_2 in confined spaces, which is extremely important for the workers in closed spaces to avoid the risk of asphyxia.

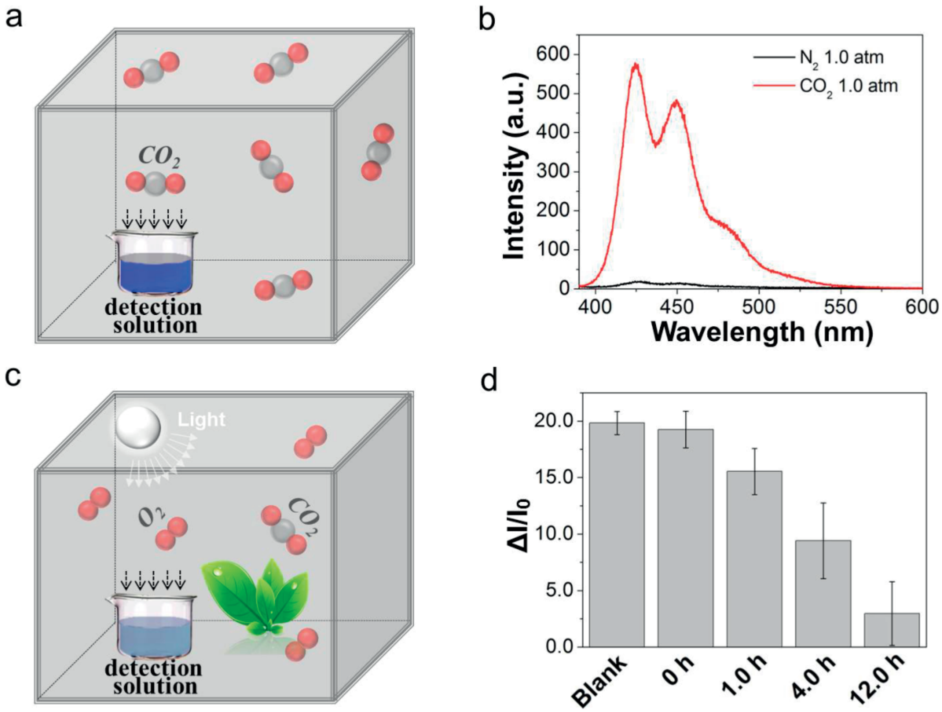

Figure 4.7. Scheme (a) and fluorescence spectra (b) of the G-OF with N_2 and CO_2 atmosphere in the presence of PTP. Scheme (c) and fluorescence intensities (d) of G-OF in CO_2 atmosphere in the presence of PTP versus different time of illumination. Blank represents the fluorescence intensities of G-OF in the presence of PTP in CO_2 atmosphere without photosynthesis. All data were presented as mean values ± standard deviation of three separate experiments. Error bars represent standard deviations of data from three separate measurements. [G-OF] = 0.8 µM, [PTP] = 875.0 nM (in repeat units). Measurements were performed at 4 ^{0}C in water. The excitation wavelength was 378 nm.

Finally, the CO_2 was monitored in the process of photosynthesis. It is well-known that plant photosynthesis converts CO_2 into carbohydrate by assimilation of sunlight and H_2O. Here, we employed *Zea mays*, a C_4-photosynthetic plant with high photosynthetic rate,[50,51] as a model system to study the response of the G-OF/PTP-based probe to monitor the CO_2 changes in plant photosynthesis. As exhibited in Figure 4.7c, *Zea mays* was placed in the confined chamber with light and CO_2, and the fluorescence intensity of the G-OF/PTP hybrid probe was decreased gradually with the increase of the illumination time (Figure 4.7d), indicating the assimilation of CO_2 by photosynthesis. Therefore, our CO_2 detection strategy can be applied to monitor CO_2 changes in plant photosynthesis.

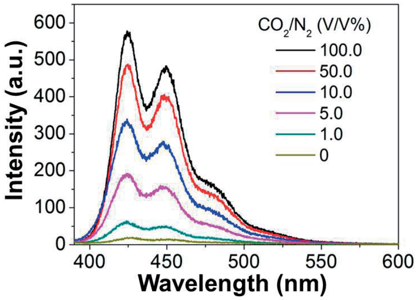

Figure 4.8. Fluorescence spectra of the G-OF with different volume ratios of CO_2/N_2 mixtures atmosphere in the presence of PTP. [G-OF] = 0.8 µM, [PTP] = 875.0 nM (in repeat units), the volume ratios of CO_2/N_2 change from 0 to 100.0%. Measurements were performed at 4 ºC in sterile water. The excitation wavelength was 410 nm.

4.3 Conclusions

In summary, we have designed a hybrid probe comprising guanidinium-pendent oligofluorene (G-OF) and water-soluble conjugated polythiophene derivative (PTP) for sensing CO_2 with very low background signal. This detection strategy takes advantage of the superquenching property of G-OF by PTP in the tight aggregates of G-OF/PTP, and the CO_2 controlled aggregation induces the turn-on signal of fluorescence. The new, simple and light-up visible CO_2 assay system has several unique characteristics. First, the G-OF/PTP-based hybrid probe realizes the quantitative detection of CO_2 in both gaseous and dissolved phase. Second, the strategy can be applied for assessment of asphyxial risk in confined spaces. Furthermore, our CO_2 optical detection system enables the monitoring of CO_2 in plant photosynthesis. Therefore, the G-OF/PTP-based turn-on approach for CO_2 detection provides meaningful applications in asphyxia diagnosis and monitoring plant photosynthesis.

4.4 Experimental Section

Materials and Measurements

G-OF and PTP were synthesized referring to the procedure reported in the literatures.[46,47] All chemicals were purchased from Acros, Aladdin or Alfa Aesar and used as received if not specially stated. All organic solvent were purchased from Tianjin Guangfu Ltd. CO_2, N_2 and O_2 were certified food grade (99.99% purity) and obtained from Tianjin Lianbo Ltd. All solutions were prepared with pre-cooling MilliQ water at 4 ºC. The fluorescence spectra were taken on a Hitachi F-4500 fluorimeter equipped with a Xenon lamp excitation source at 4 ºC which was controlled by Recirculating Chiller F-305 (BÜCHI). Dynamic light scattering (DLS) experiments and ζ Potentials were carried out on Nano-S90 (Malvern Instruments, UK).

Detection of CO_2 in water

To 400.0 µL of ddH_2O was added G-OF (0.8 µM) and bubbled with different volumes of CO_2 at a constant flow rate of 1.5 mL/min, and then 875.0 nM (in repeat units) of PTP was added and mixed gently. After 5.0 min of incubation, the fluorescence spectra were measured in quartz cuvettes by applying a Hitachi F-4500 fluorimeter at 4 ºC. The excitation wavelength was 378 nm.

Preparation for different ratios of CO_2/ N_2 mixtures

The flow rate of CO_2 and N_2 were controlled by standard flowmeter and mixed in a sampling bag.

Detection of CO_2 by composite film

10.0 µM of G-OF solution was sprayed on the cellulose ester film. After 5.0 min of exposure to a CO_2 atmosphere, the PTP (8.0 µM) was sprayed, and then the images were taken under UV light ($\lambda = 365$ nm).

Detection of CO_2 in photosynthesis

An airtight chamber (500 × 500 × 500 mm^3) was designed with an inlet, an outlet, lamps (300 W) and a delivery window. *Zea mays* were grown in vermiculite for 14 days in a greenhouse. We eliminated the air in chamber through the method of vacuum, and then filled with CO_2 to 1.0 atm. The 1.0 mL of detection solution contained with G-OF ([G-OF] = 0.8 µM) was put in the chamber after different time of illumination. After 12 hours of equilibrium, 875.0 nM (in repeat units) of PTP was added, and the fluorescence spectra were measured.

4.5 References

(1) Cox, P. M.; Betts, R. A.; Jones, C. D.; Spall, S. A.; Totterdell, I. J. *Nature* **2000**, *408*, 184.

(2) Leaf, D.; Verolme, H. J.; Hunt, W. F. *Environ. Int.* **2003**, *29*, 303.

(3) Guais, A.; Brand, G.; Jacquot, L.; Karrer, M.; Dukan, S.; Grévillot, G.; Molina, T. J.; Bonte, J.; Regnier, M.; Schwartz, L. *Chem. Res. Toxicol.* **2011**, *24*, 2061.

(4) Bassham, J. A. *Science* **1977**, *197*, 630.

(5) Zelitch, I. *Proc. Natl. Acad. Sci. U. S. A.* **1973**, *70*, 579.

(6) Gillett, N. P.; Arora, V. K.; Matthews, D.; Allen, M. R. *J. Clim.* **2013**, *26*, 6844.

(7) Frölicher, T. L.; Winton, M.; Sarmiento, J. L. *Nat. Clim. Change* **2014**, *4*, 40.

(8) Hassan, M. I.; Shajee, B.; Waheed, A.; Ahmad, F.; Sly, W. S. *Bioorg. Med. Chem.* **2013**, *21*, 1570.

(9) Geers, C.; Gros, G. *Physiol. Rev.* **2000**, *80*, 681.

(10) Gray, J. M.; Frolking, S.; Kort, E. A.; Ray, D. K.; Kucharik, C. J.; Ramankutty, N.; Friedl, M. A. *Nature* **2014**, *515*, 398.

(11) Neethirajan, S.; Jayas, D.; Sadistap, S. *Food Bioprocess Technol.* **2009**, *2*, 115.

(12) Amao, Y.; Nakamura, N. *Sens. Actuators. B* **2005**, *107*, 861.

(13) Oter, O.; Ertekin, K.; Derinkuyu, S. *Talanta* **2008**, *76*, 557.

(14) Dansby-Sparks, R. N.; Jin, J.; Mechery, S. J.; Sampathkumaran, U.; Owen, T. W.; Yu, B. D.; Goswami, K.; Hong, K.; Grant, J.; Xue, Z.-L. *Anal. Chem.* **2010**, *82*, 593.

(15) Wang, H.; Chen, D.; Zhang, Y.; Liu, P.; Shi, J.; Feng, X.; Tong, B.; Dong, Y. *J. Mater. Chem. C* **2015**, *3*, 7621.

(16) Liu, Y.; Tang, Y.; Barashkov, N. N.; Irgibaeva, I. S.; Lam, J. W.; Hu, R.; Birimzhanova, D.; Yu, Y.; Tang, B. Z. *J. Am. Chem. Soc.* **2010**, *132*, 13951.

(17) Ali, R.; Lang, T.; Saleh, S. M.; Meier, R. J.; Wolfbeis, O. S. *Anal. Chem.* **2011**, *83*, 2846.

(18) Ishida, M.; Kim, P.; Choi, J.; Yoon, J.; Kim, D.; Sessler, J. L. *Chem. Commun.* **2013**, *49*, 6950.

(19) Suresh, V. M.; Bonakala, S.; Roy, S.; Balasubramanian, S.; Maji, T. K. *J. Phys. Chem. C* **2014**, *118*, 24369.

(20) Xu, Q.; Lee, S.; Cho, Y.; Kim, M. H.; Bouffard, J.; Yoon, J. *J. Am. Chem. Soc.* **2013**, *135*, 17751.

(21) Feng, L. H.; Zhu, C. L.; Yuan, H. X.; Liu, L. B.; Lv, F. T.; Wang, S. *Chem. Soc. Rev.* **2013**, *42*, 6620.

(22) Rochat, S.; Swager, T. M. *J. Am. Chem. Soc.* **2013**, *135*, 17703.

(23) Wasilke, J.-C.; Obrey, S. J.; Baker, R. T.; Bazan, G. C. *Chem. Rev.* **2005**, *105*, 1001.

(24) Jo, J.; Pouliot, J. R.; Wynands, D.; Collins, S. D.; Kim, J. Y.; Nguyen, T. L.; Woo, H. Y.; Sun, Y.; Leclerc, M.; Heeger, A. J. *Adv. Mater.* **2013**, *25*, 4783.

(25) Liu, J.; Yee, K.-K.; Lo, K. K.-W.; Zhang, K. Y.; To, W.-P.; Che, C.-M.; Xu, Z. *J. Am. Chem. Soc.* **2014**, *136*, 2818.

(26) Xing, C.; Yuan, H.; Xu, S.; An, H.; Niu, R.; Zhan, Y. *ACS Appl. Mater. Interfaces* **2014**, *6*, 9601.

(27) Jia, Y.; Zuo, X.; Lou, X.; Miao, M.; Cheng, Y.; Min, X.; Li, X.; Xia, F. *Anal. Chem.* **2015**, *87*, 3890.

(28) Ho, H. A.; Boissinot, M.; Bergeron, M. G.; Corbeil, G.; Dore, K.; Boudreau, D.; Leclerc, M. *Angew. Chem., Int. Ed.* **2002**, *41*, 1548.

(29) Liu, X.; Ouyang, L.; Cai, X.; Huang, Y.; Feng, X.; Fan, Q.; Huang, W. *Biosens. Bioelectron.* **2013**, *41*, 218.

(30) Xing, X.-J.; Liu, X.-G.; He, Y.; Lin, Y.; Zhang, C.-L.; Tang, H.-W.; Pang, D.-W. *Biomacromolecules* **2012**, *14*, 117.

(31) Usmani, S. M.; Zirafi, O.; Muller, J. A.; Sandi-Monroy, N. L.; Yadav, J. K.; Meier, C.; Weil, T.; Roan, N. R.; Greene, W. C.; Walther, P.; Nilsson, K. P. R.; Hammarstrom, P.; Wetzel, R.; Pilcher, C. D.; Gagsteiger, F.; Faendrich, M.; Kirchhoff, F.; Munch, J. *Nat. Commun.* **2014**, *5*, 1962.

(32) Yuan, H.; Xing, C.; An, H.; Niu, R.; Li, R.; Yan, W.; Zhan, Y. *ACS Appl. Mater. Interfaces* **2014**, *6*, 14790.

(33) Yuan, H.; Qi, J.; Xing, C.; An, H.; Niu, R.; Zhan, Y.; Fan, Y.; Yan, W.; Li, R.; Wang, B. *Adv. Funct. Mater.* **2015**, *25*, 4412.

(34) Kumaraswamy, S.; Bergstedt, T.; Shi, X.; Rininsland, F.; Kushon, S.; Xia, W.; Ley, K.; Achyuthan, K.; McBranch, D.; Whitten, D. *Proc. Natl. Acad. Sci. U. S. A.* **2004**, *101*, 7511.

(35) Bai, J.; Liu, C.; Yang, T.; Wang, F.; Li, Z. *Chem. Commun.* **2013**, *49*, 3887.

(36) Yang, Q.; Dong, Y.; Wu, W.; Zhu, C.; Chong, H.; Lu, J.; Yu, D.; Liu, L.; Lv, F.; Wang, S. *Nat. Commun.* **2012**, *3*, 1206.

(37) Lee, S. H.; Kang, Y. Y.; Jang, H.-E.; Mok, H. *Adv. Drug delivery rev.* **2016**, *104*, 78.

(38) Shi, H.; Kwok, R. T.; Liu, J.; Xing, B.; Tang, B. Z.; Liu, B. *J. Am. Chem. Soc.* **2012**, *134*, 17972.

(39) Lee, K.; Lee, J.; Jeong, E. J.; Kronk, A.; Elenitoba-Johnson, K. S.; Lim, M. S.; Kim, J. *Adv. Mater.* **2012**, *24*, 2479.

(40) Bai, H.; Yuan, H.; Nie, C.; Wang, B.; Lv, F.; Liu, L.; Wang, S. *Angew. Chem., Int. Ed.* **2015**, *54*, 13208.

(41) Li, R.; Niu, R.; Qi, J.; Yuan, H.; Fan, Y.; An, H.; Yan, W.; Li, H.; Zhan, Y.; Xing, C. *ACS Appl. Mater. Interfaces* **2015**, *7*, 14569.

(42) Yan, W.; Yuan, H.; Li, R.; Fan, Y.; Zhan, Y.; Qi, J.; An, H.; Niu, R.; Li, G.; Xing, C. *Macromol. Chem. Phys.* **2015**, *216*, 1603.

(43) Moroney, J. V.; Jungnick, N.; DiMario, R. J.; Longstreth, D. J. *Photosynth. Res.* **2013**, *117*, 121.

(44) Busch, F. A.; Sage, T. L.; Cousins, A. B.; Sage, R. F. *Plant, Cell Environ.* **2013**, *36*, 200.

(45) Shimada, N.; Nakayama, M.; Kano, A.; Maruyama, A. *Biomacromolecules* **2013**, *14*, 1452.

(46) Chen, H.; Wang, B.; Zhang, J.; Nie, C.; Lv, F.; Liu, L.; Wang, S. *Chem. Commun.* **2015**, *51*, 4036.

(47) Xing, C.; Xu, Q.; Tang, H.; Liu, L.; Wang, S. *J. Am. Chem. Soc.* **2009**, *131*, 13117.

(48) Kim, O.-K.; Je, J.; Melinger, J. S. *J. Am. Chem. Soc.* **2006**, *128*, 4532.

(49) Yuan, H.; Xing, C.; Fan, Y.; Chai, R.; Niu, R.; Zhan, Y.; Peng, F.; Qi, J. *Macromol. Rapid Commun.* **2017**, *38*.

(50) Marino, B. D.; McElroy, M. B. *Nature* **1991**, *349*, 127.

(51) Crespo, H.; Frean, M.; Cresswell, C.; Tew, J. *Planta* **1979**, *147*, 257.

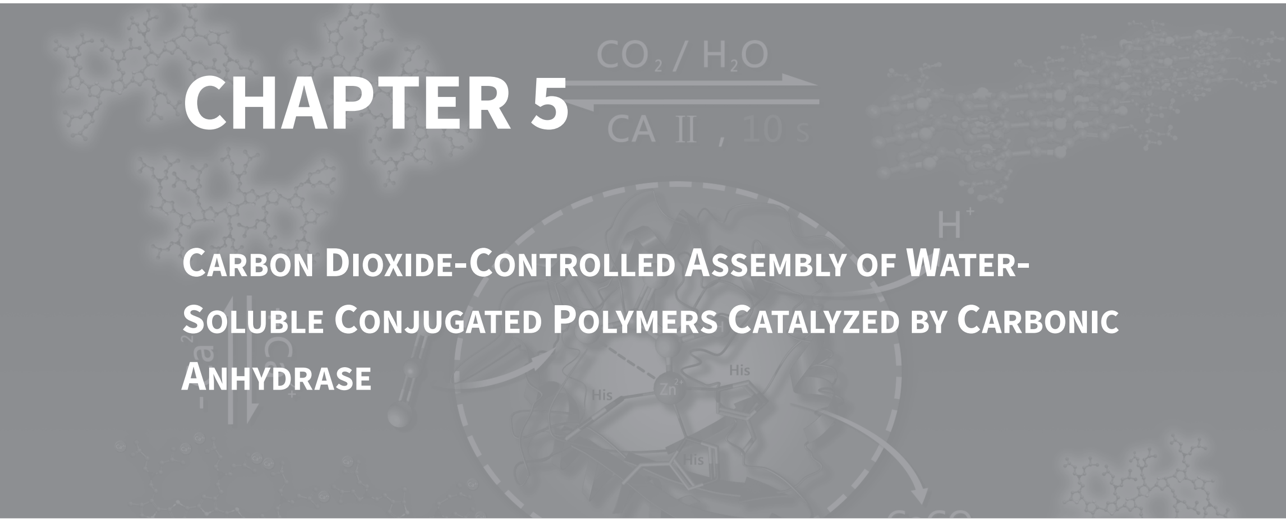

CHAPTER 5

CARBON DIOXIDE-CONTROLLED ASSEMBLY OF WATER-SOLUBLE CONJUGATED POLYMERS CATALYZED BY CARBONIC ANHYDRASE

This chapter has been published in:
Yuan, H.; Xing, C.; Fan, Y.; Chai, R.; Niu, R.; Zhan, Y.; Peng, F.; Qi, J., *Macromol. Rapid Commun.* **2017,** *38*. DOI: 10.1002/marc.201600726

Fan Y. and Niu R. are acknowledged for the synthesis and characterization of PTP. Chai R. and Peng F. preformed the AFM and SEM measurements. Dr Qi J. is acknowledged for discussions on the interpretation of the results. Prof. Xing C. and Prof. Zhan Y. supervised the project.

Abstract

The CO_2-responsive and biocatalytic assembly based on conjugated polymers has been demonstrated by combining the signal amplification property of the polythiophene derivative (PTP) and the catalytic actions of carbonic anhydrase (CA). CO_2 is applied as a new trigger mode to construct the smart assembly by controlling the electrostatic and hydrophobic interactions between the PTP molecules in aqueous solution, leading to the visible fluorescence changes. Importantly, the assembly transformation of PTP can be specifically and highly accelerated by CA based on the efficient catalytic activity of CA for the inter-conversion between CO_2 and HCO_3^-, mimicking the CO_2-associated biological processes that occurred naturally in living organisms. Moreover, the PTP-based assembly can be applied for biomimetic CO_2 sequestration with fluorescence monitoring in the presence of CA and calcium.

5.1 Introduction

CO_2 is an essential molecule in all the aerobic organisms possessing high membrane permeability and biocompatibility, which has been exploited as a new trigger mode to construct stimuli-responsive biocompatible systems.[1–3] Moreover, CO_2 emission acts a major contributor in the global warming,[4,5] and many efforts are being made to capture and store CO_2 by using porous structure materials,[6] carbonaceous adsorbents,[7] metal oxides[8,9] and metal–organic frameworks.[10,11] Recently, carbonic anhydrase (CA)-functionalized materials have been used for CO_2 sequestration by applying the biocatalytic activity of CA.[12–14] CO_2 hydrates to form a weak acid, namely the carbonic acid (H_2CO_3), and stabilizes the intracellular and body fluid pH value by virtue of the equilibrium with bicarbonate (HCO_3^-).[15,16] There is an effective barrier to the passive diffusion of HCO_3^- and H^+ in biological membranes, whereas CA is an enzyme that catalyzes the inter-conversion between CO_2 and HCO_3^- with a high catalytic activity in organisms,[17,18] and facilitates the transport of CO_2 and protons in the intracellular space and across the biological membranes.[19,20] Despite many efforts on the construction of CO_2-responsive polymer assemblies,[1–3,21,22] the examples of enzyme involved and catalyzed polymer assemblies regulated by CO_2 that mimic the CO_2-associated biochemical progress in organisms are still few but highly desired.

Water-soluble conjugated polymers (WCPs) have attracted much attention due to their excellent light harvesting and signal amplification properties.[23–25] In recent years, WCPs have been developed as ideal platforms for the biological applications such as high sensitivity sensing and detection,[26–31] as well as cell imaging,[32–35] disease diagnosis[36,37] and drug delivery.[38,39] In most cases, these WCPs-based biological applications take advantages of their responsive properties to the external signals including pH value,[40–43] electrical charge[44,45] and ligands[46–48] by changing their photophysical property, assembly and conformation. Recently, Yoon and colleagues developed polydiacetylene-based CO_2 detection system by applying the response of conjugated polymer to CO_2 in aqueous solution and in the solid state.[22] However, the exploration of the influence of CO_2 on the WCPs assemblies combining enzyme's actions is still a striking topic. Therefore, the construction of smart WCPs assemblies controlled by the new trigger of CO_2 and combining the catalytic effect of CA to mimic the biochemical process and sequester CO_2 are important and promising. In this work, we demonstrate the CO_2-controlled assembly of a polythiophene derivative that can be accelerated in aqueous medium by carbonic anhydrases based on its high-efficient catalytic activity and used as a biomimetic CO_2 sequestration platform. As illustrated in **Scheme 5.1**, we employ a polythiophene derivative (PTP) bearing a side chain with one amino and two carboxylate groups in each repeat unit. In neutral aqueous medium, the carboxylic acid groups of PTP are deprotonated and exhibit negative charges. Therefore, the intense electrostatic repulsion between the side chains of PTP keeps them well-separated with a randomly coiled configuration, and thus the polymer PTP exhibits intensive intrinsic greenish-yellow fluorescence. When CO_2 is bubbled into the solution, the CO_2 hydrates to form carbonic acid (H_2CO_3), which protonates both the carboxylate and amino groups of PTP. In this case, the electrostatic repulsion between neighbouring PTP that prevents the aggregation has been reduced, and therefore PTP forms tight aggregations driven by the π-π stacking of backbone, leading to the quenching of the fluorescence. Moreover, carbonic anhydrase II (CA II) can be involved by catalyzing the inter-conversion between CO_2 and HCO_3^-, which results in the accelerated assemblies of PTP that completes within 10 seconds owing to the high-efficient catalytic activity of CA II. Furthermore, the carboxylate groups in the side chains of PTP coordinate with calcium ions (Ca^{2+}) to form the chelate of PTP/Ca^{2+}, cross-linkingly assembling to the supramolecular network and producing the fluorescence quenching of PTP. Upon adding CA II and bubbling CO_2, the fluorescence of PTP was recovered immediately, resulting from the high catalytic activity of CA II and the subsequent precipitation of $CaCO_3$, releasing PTP and sequestering CO_2. Therefore, the CO_2-controlled PTP-based assembly catalyzed by CA can be used as a multi-functional platform for CO_2 monitoring and biomimetic sequestration.

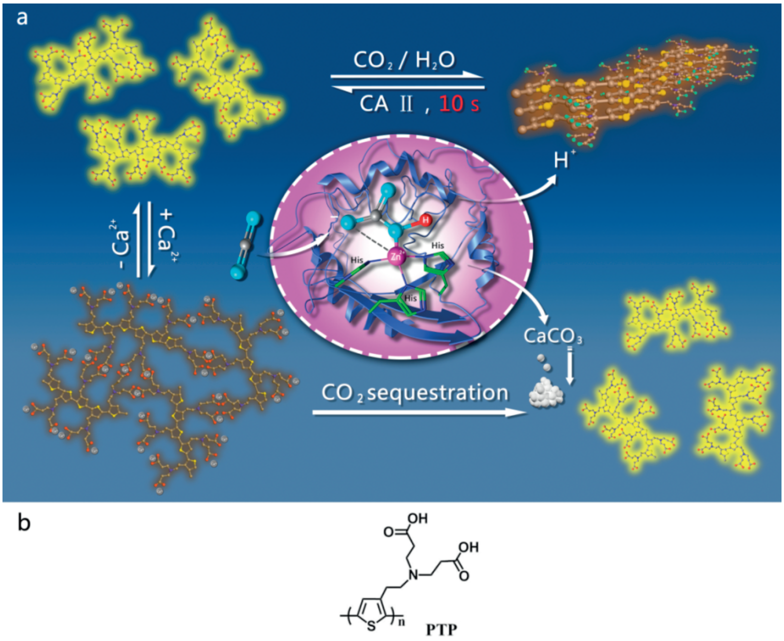

Scheme 5.1. (a) Schematic representation of the CO_2-responsive assembly and the CO_2-sequestration by PTP catalyzed by carbonic anhydrase (CA) in the presence of CO_2. (b) The chemical structure of PTP.

5.2 Results and Discussion

The polymer PTP has been synthesized referring to the reported procedures.[49] Spectroscopic studies suggest that PTP exhibits an absorption maximum at 410 nm and emits intensive greenish-yellow fluorescence with the maximum emission at 545 nm in aqueous solution, corresponding to the π–π* transition of the conjugated polythiophene's backbone.[44,50] In this contribution, CO_2 was used as a new trigger to construct the responsive assembly of PTP with one amino and two carboxylate groups in each repeating unit. As demonstrated in **Figure 5.1**a, the fluorescence of PTP with a constant concentration ([PTP] = 16.0 µM) was quenched gradually with successive bubbling of CO_2. The Stern-Volmer constant (K_{SV}) has been deduced to be 4.2×10^2 M^{-1}, indicating that PTP aggregated gradually with the increasing amount of CO_2 that hydrated to form H_2CO_3 and thus protonated the carboxylate groups of PTP. Moreover, the aggregation of PTP induced by CO_2 can be directly visualized through the color changes of PTP, from bright greenish-yellow to dark orange under the UV irradiation (Figure 5.1b). Therefore, the fluorescence properties of PTP are responsive to CO_2 directly and visually. Furthermore, the ζ potentials and dynamic light scattering (DLS) have been carried out to demonstrate the charge and size changes of PTP aggregates in the presence of CO_2 in aqueous solution. As shown in Figure 5.1c, d, PTP alone forms dispersed aggregates with an average diameter of about 100 nm, owing to the strong electrostatic repulsion between side chains. However, after bubbling CO_2, the ζ potential of PTP is very close to zero, resulting to PTP self-assemblies with an average diameter of about 800 nm. This makes sense considering that PTP is well-separated in abscence of CO_2 due to the deprotonation of carboxylic acid groups with negetive charges that prevent the PTP aggregation by electrostatic repulsion.

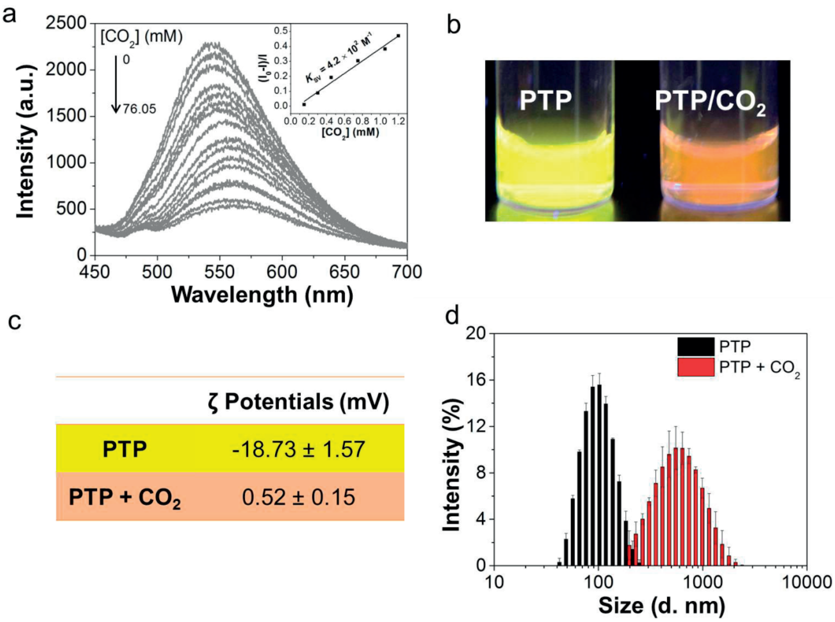

	ζ Potentials (mV)
PTP	-18.73 ± 1.57
PTP + CO_2	0.52 ± 0.15

Figure 5.1. (a) Fluorescence spectra of PTP in sterile water with successive addition of CO_2. Inset: K_{SV} plot of PTP fluorescence quenched by CO_2 in aqueous solution. [PTP] = 16.0 µM in repeat units; [CO_2] = 0 ~ 76.05 mM; Excitation wavelength: 410 nm. (b) Fluorescence images of the PTP in sterile water with and without CO_2 under UV light (λ_{max} = 365 nm). [PTP] = 25.0 µM in repeat units. (c) ζ Potentials of PTP with and without CO_2 in water. (d) Size distribution histograms of PTP with and without CO_2 resulting from DLS measurements.

In order to obtain further insight into the CO_2-responsive assembly of PTP, the fluorescence of PTP ([PTP] = 16.0 µM in repeat units) in PB buffer (10 mM) as a function of pH values were measured. As shown in **Figure 5.2**a, b, the emission intensity of PTP is gradually increased as the pH raises from 3.0 to 9.0 (**Figure 5.3**), indicating that PTP becomes more and more separated with the deprotonation of carboxylate groups which completes at pH 9.0. While the fluorescence intensity of PTP is slightly decreased as the pH raises from 9.0 to 12.0, which is tentatively attributed to instability of PTP under strong basic conditions. However, the emission of PTP is increased as the pH decreases from 3.0 to 1.0 (Figure 5.3a) and the emission of PTP was minimum at pH 3.0. This indicates that PTP starts to be positively charged with the protonation of amino groups and the complete protonation of the carboxylic acid groups, resulting in the most intense aggregation of PTP in aqueous solution. These results are according with the pK_a values of tertiary amine and carboxyl groups (9.54 and 2.2, respectively).[51] Furthermore, The emission maximum (λmax) of PTP shows the largest red-shift at pH 3.0, indicating a transformation from a random-coil conformation to a more planar and conjugated conformation due to the π−π stacking of the conjugated polythiophene's backbone. The cycling of the emission maximum of PTP between pH 3.0 and 11.0 demonstrates that the aggregation of PTP is highly reversible (**Figure 5.4**). Notably, the fluorescence images of PTP at different pH (from 1.0 to 12.0) under UV light excitation present a clearly visible color change from slight greenish-yellow to dark red and then brilliant greenish-yellow (Figure 5.2c). Such a pH-responsive aggregation behavior of PTP has been further studied in the Tris-HCl buffer (**Figure 5.5**), and the result is similar to that in PB buffer. Therefore, these results illustrate that the aggregation of PTP can be controlled by pH reversibly based on the protonation and deprotonation of the amino and carboxylate groups in the side chains.

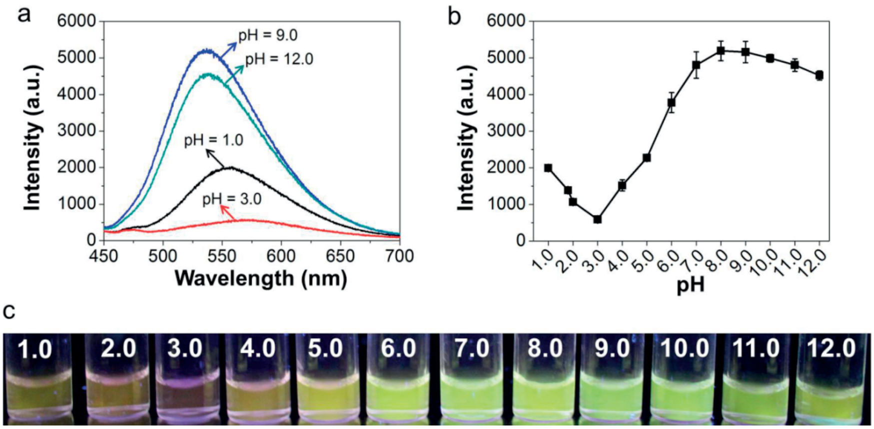

Figure 5.2. (a) Fluorescence spectra of PTP in PB buffer (10.0 mM) at pH 1.0, 3.0, 9.0 and 12.0. (b) Maximum fluorescence intensity of PTP as a function of pH values in PB buffer. The excitation wavelength was 410 nm. All data are presented as mean values ± standard deviation of three separate experiments. Error bars represent standard deviations of data from three separate measurements. (c) Fluorescence images of the PTP in PB buffer at different pH values under UV light (λ_{max} = 365 nm). [PTP] = 16.0 µM in repeat units. Measurements were performed in PB buffer solution (10.0 mM).

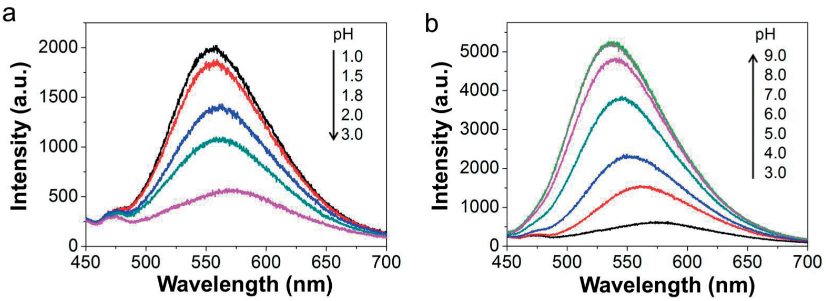

Figure 5.3. (a) Fluorescence spectra of PTP in PB buffer as the pH raised from 1.0 to 3.0. (b) Fluorescence spectra of PTP in PB buffer as the pH raised from 3.0 to 9.0. [PTP] = 16.0 µM in repeat units. Measurements were performed in PB buffer solution (10.0 mM). The excitation wavelength was 410 nm.

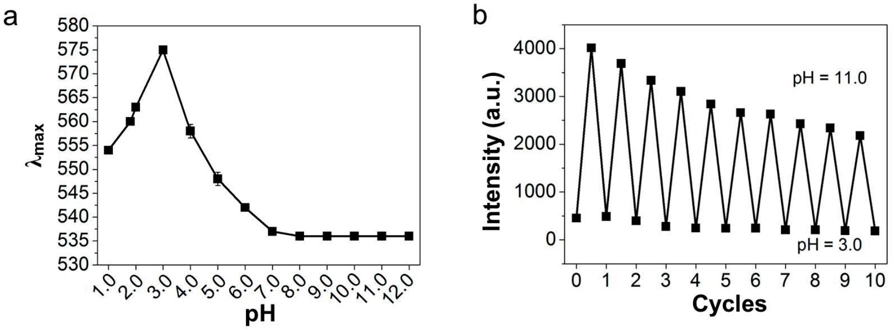

Figure 5.4. (a) Maximum wavelength of PTP emission as a function of pH values in PB buffer. (b) The maximum fluorescence intensity of PTP upon cycling the pH between 11.0 and 3.0 in PB buffer. [PTP] = 16.0 μM in repeat units. Measurements were performed in PB buffer solution (10.0 mM). The excitation wavelength was 410 nm. Error bars show the standard deviation of three separated experiments.

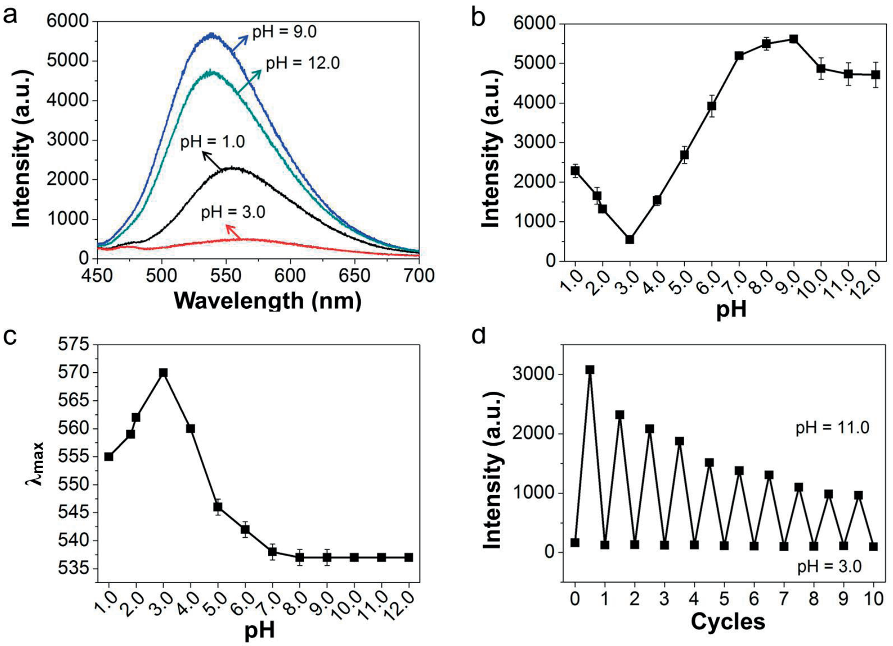

Figure 5.5. (a) Fluorescence spectra changes of PTP in Tris-HCl buffer (20 mM) at pH 1.0, 3.0, 9.0 and 12.0. (b) Maximum fluorescence intensity of PTP as a function of pH values in Tris-HCl buffer. (c) Maximum wavelength of PTP emission as a function of pH values in Tris-HCl buffer. (d) The maximum fluorescence intensity of PTP upon cycling the pH between 11.0 and 3.0 in Tris-HCl buffer. [PTP] = 16.0 μM in repeat units. Measurements were performed in Tris-HCl buffer solution (20.0 mM). The excitation wavelength was 410 nm. All data are presented as mean values ± standard deviation of three separate experiments. Error bars represent standard deviations of data from three separate measurements.

Moreover, dynamic light scattering (DLS) has been carried out to analyze the size distributions of PTP assemblies in aqueous solution at different pH. As shown in **Figure 5.6**, the average hydrodynamic diameter of PTP at pH 3.0 is about 871 nm, which is much larger than that at pH 12.0 (147 nm). At pH 1.0, the average hydrodynamic radius of PTP is about 289 nm, between those at pH 12.0 and 3.0, demonstrating the most intense aggregation of PTP at pH 3.0, which is consistent with the results of fluorescence measurements. In addition, the cycling of the average hydrodynamic radius of PTP between pH 3.0 and 12.0 further illustrates that the aggregation of PTP is highly reversible. (Figure 5.6b). Furthermore, in order to better understand the mechanism of the pH responsive aggregation of PTP, the ζ potentials of the assemblies have been measured to study the electrical charge changes of PTP with various pH. The ζ potentials of PTP changed from negative to positive as the pH decreased from 12.0 to 1.0 (**Table 5.1**) due to the gradual protonation of amino and carboxylate groups. At pH 3.0, the ζ potential of PTP is close to zero, indicating this pH is around the isoelectric point (pI) of PTP. Therefore, the electrostatic repulsion between neighboring side chains of PTP disappeared after bubbling CO_2, forming intense aggregation dominated by hydrophobic interaction.

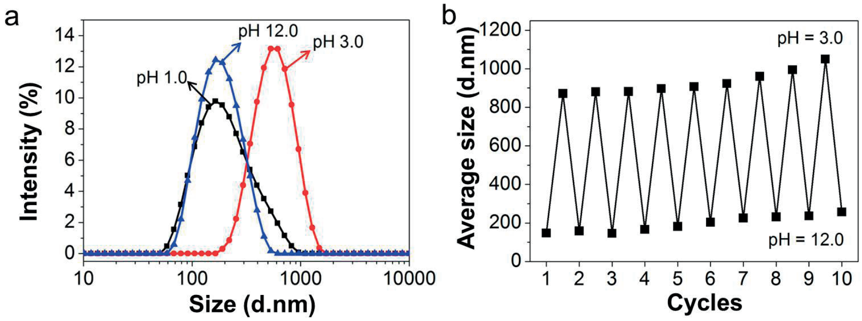

Figure 5.6. (a) Dynamic light scattering (DLS) analysis of PTP in PB buffer (10 mM) at pH 1.0, 3.0, and 12.0. [PTP] = 16.0 μM in repeat units. (b) The average hydrodynamic diameter of PTP upon cycling the pH between 12.0 and 3.0 in PB buffer (10 mM).

Table 5.1. ζ Potentials of PTP in PB buffer at pH 1.0, 3.0 and 12.0.

	ζ Potentials (mV)
pH 1.0	15.17 ± 3.13
pH 3.0	4.73 ± 0.22
pH 12.0	-28.73 ± 2.65

The formed assemblies of PTP induced by CO_2 have been further examined by atomic force microscopy (AFM) and scanning electron microscopy (SEM). As shown in **Figure 5.7**a, PTP forms well-dispersed spots with a topographic height of 1.0–2.0 nm, consistent with the size of single polymers. After bubbling CO_2 into the PTP aqueous solution, a significant increase in the height profiles of the assemblies of PTP has been observed (about 80.0 nm), which illustrates the formation of intense aggregation of PTP induced by CO_2 (Figure 5.7b). In addition, the morphologies of PTP before and after bubbling CO_2 were studied by SEM as well. As shown in Figure 5.7c, the PTP cross-linkingly assembles to the supramolecular networks upon CO_2-bubbling. These results are consistent with the DLS analysis demonstrating that PTP assembly can be controlled by CO_2.

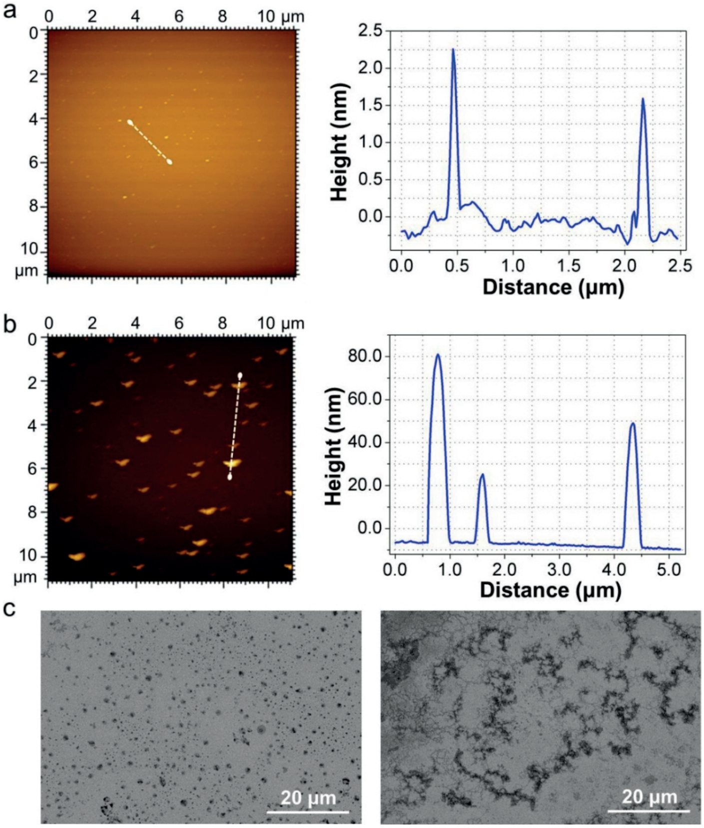

Figure 5.7. Atomic force microscopic (AFM) images of PTP without (a) and with (b) CO_2. The line profiles of the assemblies shown in (a) and (b) are presented in the right. (c) SEM images of PTP without (left) and with (right) CO_2. The accelerating voltage was 1.5 kV.

To obtain more biomimetic CO_2-responsive polymer assemblies, carbonic anhydrases (CA) has been used to catalyze the PTP self-assembly process by its high catalytic activity in the inter-conversion between CO_2 and HCO_3^-. The fluorescence emission of PTP in the presence of both CO_2 and carbonic anhydrase II (CA II) has been shown in **Figure 5.8**a. As easily noticed, the emission spectra of PTP in the presence of CO_2 were gradually decreased with the increasing amounts of CA II. Figure 5.8b exhibits that the quenching efficiency of PTP increases gradually with the increased amount of CA II, and reaches the plateau after about 0.5 U. To further validate the efficient catalysis of CA II in CO_2-responsive aggregation of PTP, we also compared the quenching rate of PTP in the presence of CO_2 with and without CA II. As exhibited in Figure 5.8c, the fluorescence intensity of the PTP with CO_2 in the presence CA II decreases by 60 % within 10 seconds, which is much quicker than that without CA II, indicating that the CA II catalyzed the aggregation of PTP by completing the inter-conversion between CO_2 and HCO_3^- efficiently. In order to further study the mechanism of our strategy, the fluorescence intensities of PTP with CO_2 in the presence of other enzymes were checked, showing a slight change relative to that of CA II, which demonstrated that the aggregation of PTP was specifically catalyzed by CA II (Figure 5.8d). Additionally, the control experiment shows that the CA II does not affect the emission spectra of PTP when adding CA II successively into the solution of PTP in the absence of CO_2 (**Figure 5.9**). Therefore, as a catalyst, the CA II accelerates specially the CO_2-responsive self-assembly of PTP.

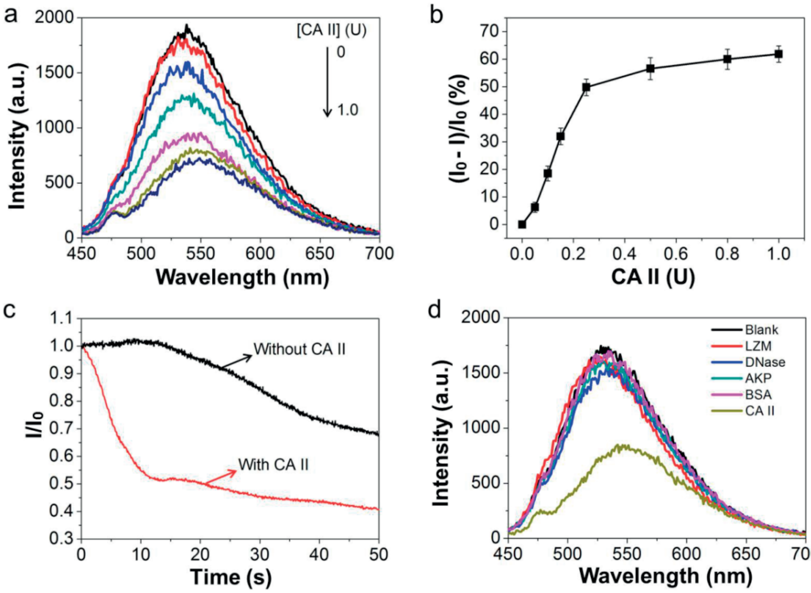

Figure 5.8. (a) Fluorescence spectra of the PTP in the presence of CO_2 as a function of CA II concentrations. (b) Fluorescence quenching efficiencies of PTP in the presence of CO_2 with different amounts of CA II, [CA II] = 0 ~ 1.0 U. Error bars show the standard deviation of three separated experiments. (c) Fluorescence intensities of the PTP with CO_2 in the presence and absence of CA II (1.0 U) versus time. (d) Fluorescence emission spectra of the PTP in the presence of CO_2 with different kinds of enzymes. [PTP] = 16.0 µM in repeat units, [CA II] = [other enzymes] = 1.0 U. The excitation wavelength was 410 nm.

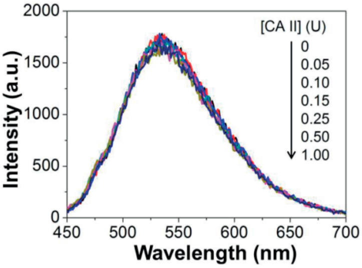

Figure 5.9. Fluorescence emission spectra of the PTP as a function of CA II concentrations. [PTP] = 16.0 µM in repeat units. The excitation wavelength was 410 nm.

Take practical applications into consideration, the CO_2-responsive PTP assemblies catalyzed by carbonic anhydrases can be applied for the CO_2 sequestration. The carboxylate groups in the side chains of PTP coordinate with Ca^{2+} to form the chelate of PTP/Ca^{2+}, cross-linkingly assembling to the supramolecular network and producing the fluorescence quenching of PTP. As shown in **Figure 5.10**a, the fluorescence of PTP/Ca^{2+} complex was totally quenched in Tris buffer, however, the fluorescence of PTP was immediately recovered upon adding CA II and bubbling CO_2 resulting from the high catalytic activity of CA II in the inter-conversion between CO_2 and HCO_3^- and the followed precipitation of $CaCO_3$, releasing PTP and sequestering CO_2. However, the fluorescence of PTP was recovered slightly upon CO_2-bubbling in the absence of CA II. Moreover, The PTP-based assembly can be applied for CO_2 sequestration for several times by replenishing Ca^{2+} (**Figure 5.11**) because CA II has no obvious interference on the fluorescence of PTP. Significantly, Figure 5.10b shows the CO_2 sequestration efficiency is 83.2 % within 2.0 min, which was evaluated based on the mass of the produced $CaCO_3$. Therefore, the PTP-based assemblies with carbonic anhydrases can be applied to storing CO_2 with high efficiency, good recycling and convenient fluorescence monitoring.

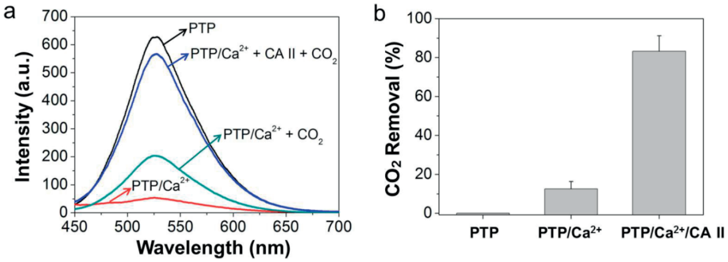

Figure 5.10. (a) Fluorescence spectra of PTP and PTP/Ca^{2+} complex with and without CO_2 in the absence and presence of CA II in Tris buffer. [PTP] = 20.0 µM in repeat units, [Ca^{2+}] = 1.0 mM, [CA II] = 1.0 U. The excitation wavelength was 410 nm. (b) CO_2 sequestration efficiency of PTP and PTP/Ca^{2+} complex in the absence and presence of CA II. [PTP] = 100.0 µM in repeat units, [Ca^{2+}] = 15.0 mM, [CO_2] = 12.7 mM, [CA II] = 5.0 U. All data were presented as mean values ± standard deviation of three separate experiments. Error bars represent standard deviations of data from three separate measurements.

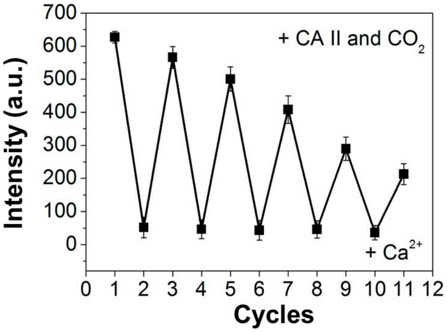

Figure 5.11. The maximum fluorescence intensity of PTP upon replenishing the Ca^{2+} and CO_2 in the presence of CA II. [PTP] = 20.0 µM in repeat units, $[Ca^{2+}]$ = 1.0 mM, [CA II] = 1.0 U. The excitation wavelength was 410 nm.

5.3 Conclusion

In conclusion, the CO_2-responsive assembly and CO_2-sequestration of PTP catalyzed by the enzyme carbonic anhydrase (CA) has been demonstrated taking advantage of the signal amplification property of PTP and the efficient catalytic activity of CA for the inter-conversion between CO_2 and HCO_3^-. CO_2 regulates the assembly of PTP by changing the electrostatic and hydrophobic interactions of the neighbouring PTP molecules, leading to visible fluorescence changes. Moreover, the CA can specifically and highly accelerate the assembly transformation of PTP owing to the efficient catalytic rate of CA, mimicking the biological processes that occurred naturally in living organisms. Furthermore, the PTP-based assembly is applied for biomimetic CO_2 sequestration with high efficiency in the presence of CA and calcium. Therefore, CO_2 is expected to be applied as a new trigger mode to construct smart conjugated polymer-based assemblies in combination with the actions of enzymes, offering a platform for biomimetic CO_2 sequestration with fluorescence monitoring.

5.4 Experimental Section

Materials and Measurements

PTP was obtained through oxidative polymerization according to the procedure reported in the literatures.[49] Carbonic anhydrase II (CA II) was purchased from Sigma. The chemicals were purchased from Acros, Aladdin or Alfa Aesar and used as received if not specially stated. All organic solvents were purchased from Tianjin Guangfu Ltd. CO_2 was certified food grade (99.99 % purity) and obtained from Tianjin Lianbo Ltd. All solutions were prepared with MilliQ water. The fluorescence spectra were taken on a Hitachi F-4600 fluorimeter equipped with a Xenon lamp excitation source. Dynamic light scattering (DLS) experiments and ζ Potentials were carried out on Nano-S90 (Malvern Instruments, UK). AFM images were taken by CSPM 5000 scanning probe microscope in tapping mode and SEM images were observed by a NOVA NANOSEM 450 (FEI, USA) field-emission scanning electron microscope. Photographs were taken with a Canon EOS-600D digital camera.

Preparation of CO_2 saturated ddH_2O

To 50.0 ml of pre-cooling ddH_2O were bubbled CO_2 (99.99 % purity) at a constant flow rate of 2.0 mL/min for no less than 30 minutes, perform this step and store the solution on ice. According to the Lange's Handbook of Chemistry, the concentration of CO_2 contained in the CO_2 saturated ddH_2O is 76.05 mM at 0 ºC.

Study for the CO_2-controlled assembly of PTP

Different concentrations of CO_2 solutions were made by mixing pre-cool MilliQ H_20 and saturated CO_2 solution. To a 400 µL of CO_2 solution with desired concentration was added 6.4 µL of 1.0 mM PTP. After 5 min of incubation, the fluorescence spectra were measured in 300 µL quartz cuvettes at 0 ºC. The solutions with different concentrations of CO_2 were prepared by mixing CO_2 saturated ddH_2O with pre-cooling ddH_2O quantificationally. The Hitachi F-4600 fluorimeter combining with a Recirculating Chiller F-305 (BÜCHI) controlled the temperature at 0 ºC. The scan speed was 1200 nm/min.

Study for the pH-responsive property of PTP

First, 10 mM PB buffer with a series of pH values by adjusting to the desired pH with HCl and NaOH were prepared. And then, to 400 µL of PB buffer with various pH values were added 16.0 µM of PTP (in repeat units), respectively. The fluorescence spectra were measured in quartz cuvettes at room temperature. The excitation wavelength was 410 nm.

Study for the morphology of PTP with and without CO_2

20.0 µL of 1.0 mM PTP was added in 100 µL of MilliQ H_2O. Next, CO_2 was bubbled into this solution for 30 minutes on ice. Each of 20 µL of the sample was placed on a mica wafer (for AFM) and silicon chips (for SEM) respectively, and then dried by vacuum freeze drying. AFM images were taken by CSPM 5000 scanning probe microscope in tapping mode and SEM images were observed by a NOVA NANOSEM 450 (FEI, USA) field-emission scanning electron microscope at an accelerating voltage of 1.5 KV. As the control experiments, the PTP without CO_2 was sampling using the same procedures.

Study for CO_2-controlled assembly of PTP catalyzed by carbonic anhydrase II (CA II)

First, 10 µL mixed solutions containing 6.4 nmol of PTP and various concentrations of carbonic anhydrase II (CA II) respectively were prepared. Next, the mixed solutions were added to 400 µL of CO_2 saturated ddH_2O respectively. Immediately following, the fluorescence spectra were measured. The temperature was controlled at 0 ºC and the scan speed was tuned to the maximum, 30000 nm/min.

Study for the CO_2 sequestration

PTP/Ca^{2+} complex were prepared by mixing 200 µM PTP and 30.0 mM $CaCl_2$ in ddH_2O. 1.5 mL of the PTP/Ca^{2+} solution was added to 1.0 mL of Tris buffer (1.4 M, pH 10.5) and mixed, and then 5.0 U of carbonic anhydrase II (CA II) and 0.5 mL of CO_2 saturated ddH_2O were added respectively. After the reaction mixture was incubated for 2 minute at 0 ºC, the sample was centrifuged for 2.0 minutes at 4000 rpm at 4 ºC, and the supernate was removed. Then the pellet was dried at 90 ºC for 24 hours and balanced. The mass of CO_2 removed was evaluated based on the mass of the produced $CaCO_3$.

5.5 References

(1) Jie, K.; Zhou, Y.; Yao, Y.; Shi, B.; Huang, F. *J. Am. Chem. Soc.* **2015**, *137*, 10472.

(2) Yan, Q.; Wang, J.; Yin, Y.; Yuan, J. *Angew. Chem., Int. Ed.* **2013**, *52*, 5070.

(3) Chen, Y.; Zhao, T.; Wang, B.; Qiu, D.; Ma, N. *Langmuir* **2015**, *31*, 8138.

(4) Cox, P. M.; Betts, R. A.; Jones, C. D.; Spall, S. A.; Totterdell, I. J. *Nature* **2000**, *408*, 184.

(5) Guais, A.; Brand, G.; Jacquot, L.; Karrer, M.; Dukan, S.; Grévillot, G.; Molina, T. J.; Bonte, J.; Regnier, M.; Schwartz, L. *Chem. Res. Toxicol.* **2011**, *24*, 2061.

(6) Banerjee, R.; Furukawa, H.; Britt, D.; Knobler, C.; O'Keeffe, M.; Yaghi, O. M. *J. Am. Chem. Soc.* **2009**, *131*, 3875.

(7) Samanta, A.; Zhao, A.; Shimizu, G. K.; Sarkar, P.; Gupta, R. *Ind. Eng. Chem. Res.* **2011**, *51*, 1438.

(8) Kim, T. K.; Lee, K. J.; Cheon, J. Y.; Lee, J. H.; Joo, S. H.; Moon, H. R. *J. Am. Chem. Soc.* **2013**, *135*, 8940.

(9) Harada, T.; Simeon, F.; Hamad, E. Z.; Hatton, T. A. *Chem. Mater.* **2015**, *27*, 1943.

(10) Beyzavi, M. H.; Klet, R. C.; Tussupbayev, S.; Borycz, J.; Vermeulen, N. A.; Cramer, C. J.; Stoddart, J. F.; Hupp, J. T.; Farha, O. K. *J. Am. Chem. Soc.* **2014**, *136*, 15861.

(11) Verdegaal, W. M.; Wang, K.; Sculley, J. P.; Wriedt, M.; Zhou, H. C. *ChemSusChem* **2016**.

(12) Uygun, M.; Singh, V. V.; Kaufmann, K.; Uygun, D. A.; de Oliveira, S. D.; Wang, J. *Angew. Chem., Int. Ed.* **2015**, *54*, 12900.

(13) Vinoba, M.; Bhagiyalakshmi, M.; Jeong, S. K.; Nam, S. C.; Yoon, Y. *Chem. Eur. J.* **2012**, *18*, 12028.

(14) Migliardini, F.; De Luca, V.; Carginale, V.; Rossi, M.; Corbo, P.; Supuran, C. T.; Capasso, C. *J. Enzyme Inhib. Med. Chem.* **2014**, *29*, 146.

(15) Chatterjee, M.; Ge, X.; Uplekar, S.; Kostov, Y.; Croucher, L.; Pilli, M.; Rao, G. *Biotechnol. Bioeng.* **2015**, *112*, 104.

(16) Tcherkez, G.; Boex-Fontvieille, E.; Mahé, A.; Hodges, M. *Curr. Opin. Plant Biol.* **2012**, *15*, 308.

(17) Ishiguro, H.; Naruse, S.; Kitagawa, M.; Suzuki, A.; Yamamoto, A.; Hayakawa, T.; Case, R.; Steward, M. *J. Physiol.* **2000**, *528*, 305.

(18) Hassan, M. I.; Shajee, B.; Waheed, A.; Ahmad, F.; Sly, W. S. *Bioorg. Med. Chem.* **2013**, *21*, 1570.

(19) Potter, C.; Harris, A. *Br. J. Cancer* **2003**, *89*, 2.

(20) Geers, C.; Gros, G. *Physiol. Rev.* **2000**, *80*, 681.

(21) Che, H.; Huo, M.; Peng, L.; Fang, T.; Liu, N.; Feng, L.; Wei, Y.; Yuan, J. *Angew. Chem., Int. Ed.* **2015**, *54*, 8934.

(22) Xu, Q.; Lee, S.; Cho, Y.; Kim, M. H.; Bouffard, J.; Yoon, J. *J. Am. Chem. Soc.* **2013**, *135*, 17751.

(23) Feng, L. H.; Zhu, C. L.; Yuan, H. X.; Liu, L. B.; Lv, F. T.; Wang, S. *Chem. Soc. Rev.* **2013**, *42*, 6620.

(24) Rochat, S.; Swager, T. M. *J. Am. Chem. Soc.* **2013**, *135*, 17703.

(25) Hou, H.; Chen, X.; Thomas, A. W.; Catania, C.; Kirchhofer, N. D.; Garner, L. E.; Han, A.; Bazan, G. C. *Adv. Mater.* **2013**, *25*, 1593.

(26) Yuan, H.; Fan, Y.; Xing, C.; Niu, R.; Chai, R.; Zhan, Y.; Qi, J.; An, H.; Xu, J. *Anal. Chem.* **2016**, *88*, 6593.

(27) Usmani, S. M.; Zirafi, O.; Muller, J. A.; Sandi-Monroy, N. L.; Yadav, J. K.; Meier, C.; Weil, T.; Roan, N. R.; Greene, W. C.; Walther, P.; Nilsson, K. P. R.; Hammarstrom, P.; Wetzel, R.; Pilcher, C. D.; Gagsteiger, F.; Faendrich, M.; Kirchhoff, F.; Munch, J. *Nat. Commun.* **2014**, *5*, 1962.

(28) Bai, J.; Liu, C.; Yang, T.; Wang, F.; Li, Z. *Chem. Commun.* **2013**, *49*, 3887.

(29) Li, R.; Niu, R.; Qi, J.; Yuan, H.; Fan, Y.; An, H.; Yan, W.; Li, H.; Zhan, Y.; Xing, C. *ACS Appl. Mater. Interfaces* **2015**, *7*, 14569.

(30) Yan, W.; Yuan, H.; Li, R.; Fan, Y.; Zhan, Y.; Qi, J.; An, H.; Niu, R.; Li, G.; Xing, C. *Macromol. Chem. Phys.* **2015**, *216*, 1603.

(31) Chai, R.; Xing, C.; Qi, J.; Fan, Y.; Yuan, H.; Niu, R.; Zhan, Y.; Xu, J. *Adv. Funct. Mater.* **2016**.

(32) Feng, L.; Liu, L.; Lv, F.; Bazan, G. C.; Wang, S. *Adv. Mater.* **2014**, *26*, 3926.

(33) Hu, W.; Lu, X.; Jiang, R.; Fan, Q.; Zhao, H.; Deng, W.; Zhang, L.; Huang, L.; Huang, W. *Chem. Commun.* **2013**, *49*, 9012.

(34) Zhu, S.; Zhang, J.; Janjanam, J.; Bi, J.; Vegesna, G.; Tiwari, A.; Luo, F.-T.; Wei, J.; Liu, H. *Anal. Chim. Acta* **2013**, *758*, 138.

(35) Xing, C.; Liu, L.; Tang, H.; Feng, X.; Yang, Q.; Wang, S.; Bazan, G. C. *Adv. Funct. Mater.* **2011**, *21*, 4058.

(36) Lv, F.; Qiu, T.; Liu, L.; Ying, J.; Wang, S. *Small* **2015**, *12*, 696.

(37) Shen, X.; Li, L.; Chan, M.; Chow, A.; Gao, N.; Yao, S. Q.; Xu, Q. H. *Adv. Opt. Mater.* **2013**, *1*, 92.

(38) Lee, S. H.; Kang, Y. Y.; Jang, H.-E.; Mok, H. *Adv. Drug delivery rev.* **2016**, *104*, 78.

(39) Shi, H.; Kwok, R. T.; Liu, J.; Xing, B.; Tang, B. Z.; Liu, B. *J. Am. Chem. Soc.* **2012**, *134*, 17972.

(40) Balamurugan, A.; Lee, H.-i. *Macromolecules* **2015**, *48*, 1048.

(41) Das, S.; Chatterjee, D. P.; Samanta, S.; Nandi, A. K. *RSC Adv.* **2013**, *3*, 17540.

(42) Xu, Q.; An, L.; Yu, M.; Wang, S. *Macromol. Rapid Commun.* **2008**, *29*, 390.

(43) Wen, Q.; Liu, L.; Yang, Q.; Lv, F.; Wang, S. *Adv. Funct. Mater.* **2013**, *23*, 764.

(44) Yuan, H.; Xing, C.; An, H.; Niu, R.; Li, R.; Yan, W.; Zhan, Y. *ACS Appl. Mater. Interfaces* **2014**, *6*, 14790.

(45) Yuan, H.; Qi, J.; Xing, C.; An, H.; Niu, R.; Zhan, Y.; Fan, Y.; Yan, W.; Li, R.; Wang, B. *Adv. Funct. Mater.* **2015**, *25*, 4412.

(46) Kwon, N. Y.; Kim, D.; Jang, G.; Lee, J. H.; So, J.-H.; Kim, C.-H.; Kim, T. H.; Lee, T. S. *ACS Appl. Mater. Interfaces* **2012**, *4*, 1429.

(47) Ho, H.-A.; Leclerc, M. *J. Am. Chem. Soc.* **2004**, *126*, 1384.

(48) Liu, B.; Wang, S.; Bazan, G. C.; Mikhailovsky, A. *J. Am. Chem. Soc.* **2003**, *125*, 13306.

(49) Xing, C.; Xu, Q.; Tang, H.; Liu, L.; Wang, S. *J. Am. Chem. Soc.* **2009**, *131*, 13117.

(50) Patra, S. K.; Ahmed, R.; Whittell, G. R.; Lunn, D. J.; Dunphy, E. L.; Winnik, M. A.; Manners, I. *J. Am. Chem. Soc.* **2011**, *133*, 8842.

(51) Shimada, N.; Nakayama, M.; Kano, A.; Maruyama, A. *Biomacromolecules* **2013**, *14*, 1452.

CHAPTER 6

STRETCHING THE CONFORMATION OF POLYTHIOPHENE BY A HELICAL POLYISOCYANIDE POLYMER

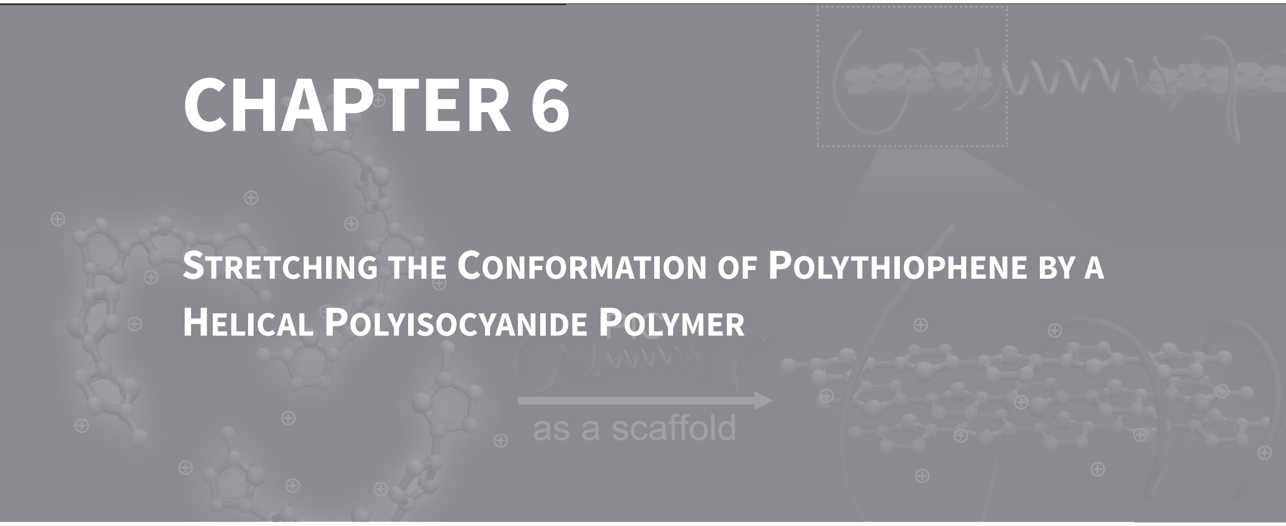

Manuscript in preparation

Abstract

Conformation changes of conjugated semiconducting polymers play an important role both in electronics and chemo/biosensor applications. In this report, we demonstrate an unusual assembly between a helical polyisocyanopeptides (PIC) host and a water-soluble PMNT guest. The PIC polymer serves as a scaffold to trap and stretch the PMNT into a highly ordered conformation, resulting in a tremendous red shift both in UV-vis and fluorescence spectra. The evidence suggests that the poorly defined extremities of PIC backbone serve as the target, and dominate the PMNT/PIC assembly. Moreover, the photophysical properties of PMNT/PIC are easily tuned by the length of PIC as a result of the small structure difference between long and short polymers. Considering the good biocompatibility and thermal responsive gelation properties of PIC, the PMNT/PIC hybrid material provides promising applications in both semiconductor and biosensor fields.

6.1 Introduction

Close control over the conformation and organization of macromolecules presents one of the best opportunities to fine-tune their physical and chemical properties.[1,2] Recently, conjugated semiconducting polymers have become an important class of electronic materials, because of their extraordinary light-harvesting and tunable electronic properties, resulting in a wide applicability in both organic electronics and chemo/biosensor applications. They find applications in, for example, light emitting diodes, photovoltaic devices, detection of small molecules, DNA and proteins, cell imaging, antibacteria and disease diagnosis.[3–7] In this regard, the ability to understand and control the molecular conformation and assembly of conjugated polymers into highly ordered structures at nanoscale has become increasingly important for the development of advanced materials with tunable properties.[8–10] In a more elongated conformation, their optoelectronic properties change because of the increasing delocalization of electrons, higher mobility of charge-carriers, and enhanced π-π stacking.[11,12] Despite the many efforts to self-assemble (or aggregate) conjugated polymers,[13–17] examples of host-guest assembly and stretching of conjugated polymers in aqueous environments are still rare but are highly desired.

Well-organized synthetic polymers are actively pursued for their unique architectures and their potential in the fields of supramolecular material sciences.[18,19] Among many artificial polymers, polyisocyanopeptides (PIC) are peculiar by virtue of their stable helical backbones with a high helix inversion barrier.[20–24] They adopt a ~4_1 (four repeats per turn) *β*-helical conformation stabilized by a *β*-sheet–like peptidic hydrogen bond network along the polymer backbone with a calculated diameter of about 16 Å, a helical pitch of 4.6 Å, and an average spacing between the side chains n and $n + 4$ of 4.7 Å, when functionalized with sterically demanding side chains preventing the kinetically formed helical polymer from unfolding.[25–27] Moreover, this helical structure plays a vital role in increasing the stiffness of the polymer chain.[28] Common believe, however, tells us that the termini of the PIC chains are less ordered than the rest of the chain, although direct experimental proof lacks. In our recent work, polyisocyanopeptides grafted with ethylene glycol side chains showed ultrasensitive mechanical responses in a biologically relevant stiffness regime, attributed to the assembly of single polymer chains into a bundled network.[29–31] In this work, we used the highly ordered host polyisocyanopeptides (PIC) as a scaffold to trap and stretch the guest material PMNT, a cationic water-soluble conjugated polythiophene derivative, resulting in a series of tunable photophysical properties. As illustrated in **Scheme 6.1**, PMNT was trapped and stretched in the extremities of the PIC chain to form the PMNT/PIC assembly by the strong hydrophobic interaction between the helical core and the polythiophene backbone, along with the electrostatic interactions between the cationic side chains of PMNT and the ethylene glycol of PIC. Consequently, the PMNT backbone is highly stretched to an extreme planar and conjugated conformation, exhibiting an unusually far red-shifted absorption and emission wavelength. Interestingly, the photophysical properties of PMNT/PIC are readily tuned by the polymer length of PIC.

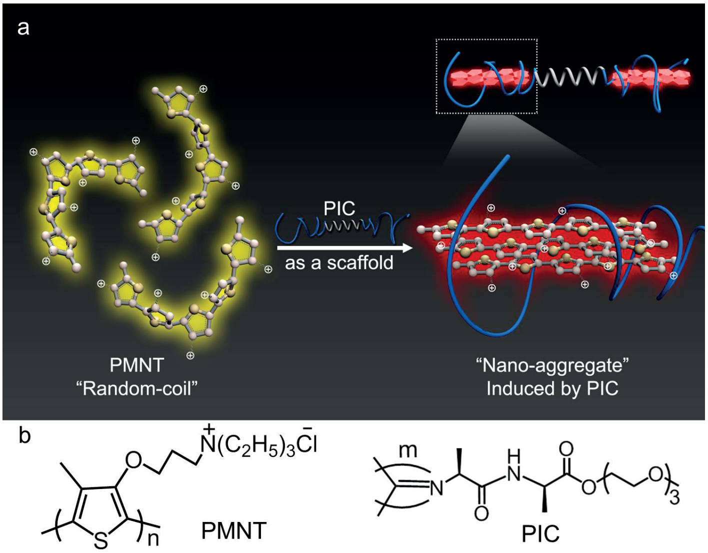

Scheme 6.1. (a) Schematic illustration of the assembly of PMNT/PIC. (b) Chemical structures of PMNT and PIC.

6.2 Results and Discussion

6.2.1 Materials

The host material is based on ethyleneglycol-functionalized polyisocyanopeptides (PIC). PIC polymers were synthesized and characterized according to the literature.[32] The length of the polymers can be controlled by changing the molar ratio of the catalyst over the monomer. In this way, a series of polymers with different lengths (PIC1–7) have been obtained (**Table 6.1**). Their molecular weights (M_v) and degree of polymerization (n) were determined by viscometry measurements based on the Mark-Houwink equation.[33] As a guest polymer, poly(3-(3′-*N,N,N*-triethylammonium-1′-propyloxy)-4-methyl-2,5-thiophene chloride) (PMNT), was synthesized and characterized following reported procedures.[34] The molecular weights were about 6–10 kDa with a poly dispersity index of about 1.2–2.9, indicating that PMNT polymers contain 20–40 thiophene repeat units in the backbone, which is in line with the results reported by Leclerc and co-workers.[34] The PMNT itself exhibits an absorption maximum at 410 nm in water, associated to the π-π* transition of the conjugated polythiophene backbone in a flexible and random-coil conformation.[35]

Table 6.1. Molecular weights M_v, and degree of polymerization (*n*) of the investigated PIC polymers.

	M_v (kg mol^{-1})	*n*
PIC1	86	272
PIC2	140	443
PIC3	195	617
PIC4	256	809
PIC5	339	1073
PIC6	451	1425
PIC7	563	1780

6.2.2 Photophysical properties of PMNT/PIC assemblies

Upon addition of PIC (2.0 mg/mL) to PMNT (25.0 µM in repeat units), two new sharp absorption bands at higher wavelengths appeared with λ_{max} = 543 and 589 nm (**Figure 6.1**a), which correspond to two vibronic levels of the π–π* transition.[13,36] This indicates that the PMNT assembles with PIC to form the nano-aggregates, and the backbones transform from a random-coil conformation to a highly coplanar and much more conjugated conformation. In addition, a corresponding red-shifted fluorescence band of PMNT/PIC at 598 nm (with a shoulder at 640 nm) was observed at an excitation wavelength at 543 nm, which closely agrees with the planar conformation observed by UV-vis (Figure 6.1b). As shown in Figure 6.1c, the assembly of PMNT/PIC can be visualized by the naked-eye via the color of the solution changing from light yellow to light red. Taking the thermal responsive properties of PIC into account,[31] we studied variable temperature UV-vis spectra of PMNT/PIC. The two new high wavelength absorption bands of PMNT/PIC decreased gradually with increasing temperature. On the contrary, the normal band at 410 nm increased (Figure 6.1d). A possible explanation is that a part of the PMNT was squeezed out of the complex due to the bundle formation of PIC polymer chains. Interestingly, a hybrid chromophoric hydrogel was obtained without changes in any other mechanical properties of the PIC gels, either in the linear or in nonlinear regime (**Figure 6.2**). Furthermore, the UV-vis spectra of PMNT with successive additions of PIC were examined. As shown in Figure 6.1e, the red-shifted bands of PMNT increased with increasing the PIC concentration, which means that the assembly of PMNT/PIC was strongly related to the amount of PIC. The red-shifted fluorescence bands of PMNT/PIC demonstrated a similar behavior (Figure 6.1f). Contrarily, the broad fluorescence band at λ_{max} = 525 nm associated to the emission of the random coil conformation, increased with decreasing the number of PIC polymers (**Figure 6.3**). It shows that most of the PMNT polymers were in a random-coil conformation at low PIC concentration. As a control, we studied the absorbance of PMNT in the presence of PEG$_{2000}$, tetraethylene glycol (TEG) and glycerol (**Figure 6.4**). All mixtures showed absorption spectra identical to those of PMNT in water, indicating that the large red shifit is not simply the result of the interaction of the cation with an ethylene glycol group. When the stongly negative charged poly(sodium 4-styrenesulfonate) (PSS) was added to the PMNT/PIC complex, electrostatic interactions between PMNT and PSS caused disassembly of the comlex and as a result of the random-coil conformation and corresponding UV-vis spectra of PMNT were retrieved (**Figure 6.5**).

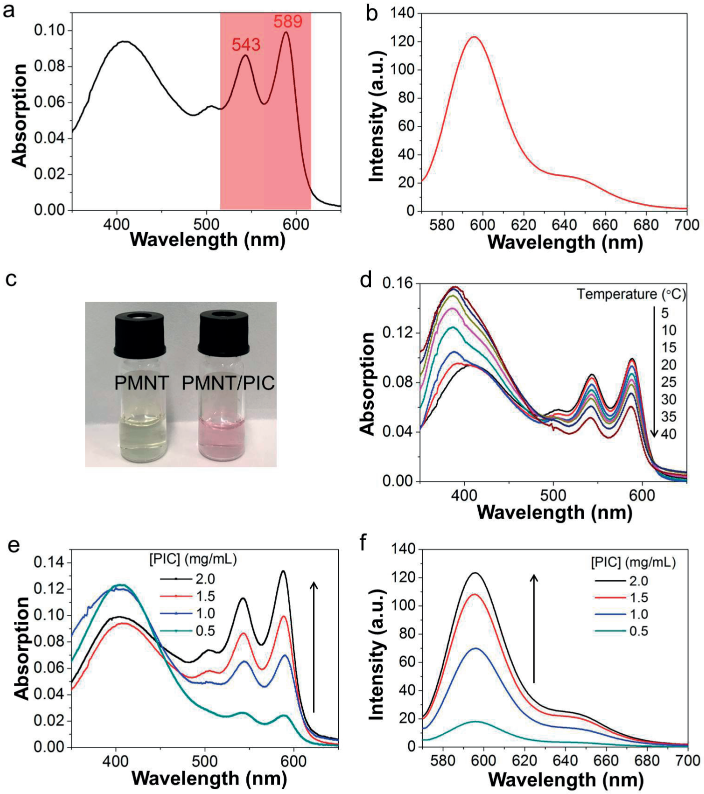

Figure 6.1. (a) UV-vis spectrum of the assembly of PMNT and PIC. (b) Fluorescence spectrum of PMNT/PIC. The excitation wavelength was 543 nm. (c) Photographs of PMNT and PMNT/PIC. (d) UV-vis spectra of PMNT/PIC as a function of temperature. (e) UV-vis spectra of PMNT/PIC as a function of PIC concentration. (f) Fluorescence spectra of PMNT/PIC as a function of PIC concentration. The excitation wavelength was 543 nm. In all spectra (unless indicated differently): [PMNT] = 25.0 µM in repeat units (RUs). PIC = PIC5 with *n* = 1073 and concentration *c* = 2.0 mg/mL. The measurements were performed at 5 °C.

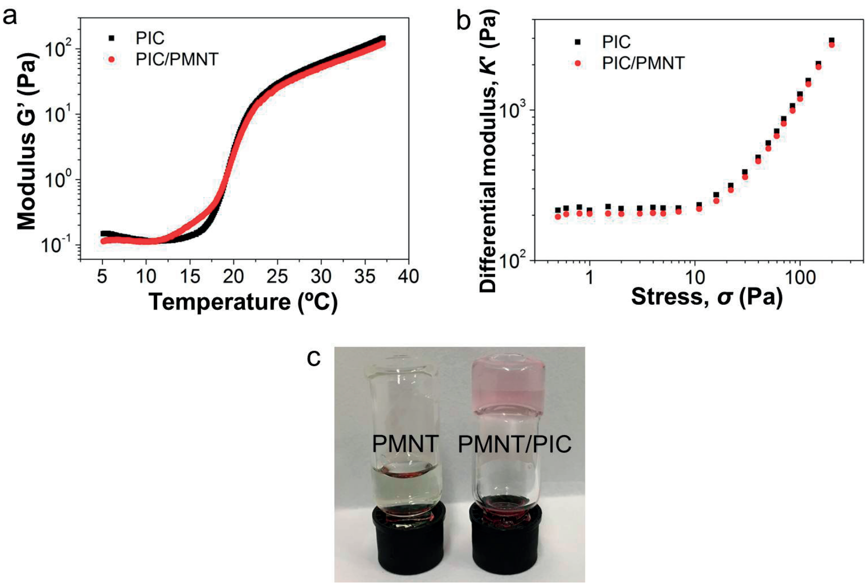

Figure 6.2. (a) Modulus *G′* of PIC and PIC/PMNT gels as a function of temperature. (b) Differential modulus *K′* against stress for the PIC and hybrid PIC/PMNT gels. (c) Photographs of PMNT and PMNT/PIC at room temperature. [PMNT] = 25.0 µM in repeat units (RUs). PIC = PIC5 with *n* = 1073 and concentration *c* = 2.0 mg/mL.

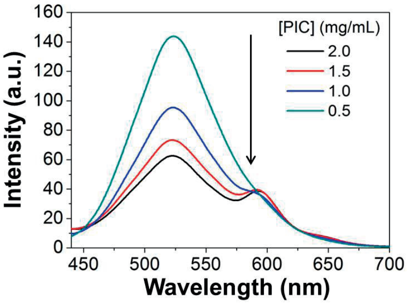

Figure 6.3. Fluorescence spectra of PMNT/PIC as a function of PIC concentration. The excitation wavelength was 410 nm. [PMNT] = 25.0 µM in repeat units (RUs). PIC = PIC5 with *n* = 1073.

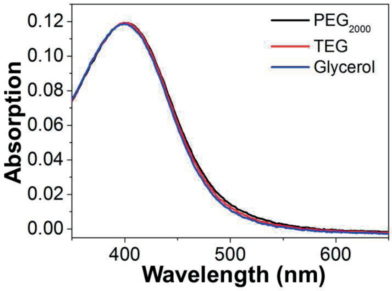

Figure 6.4. UV-vis spectra of PMNT in the presence of PEG_{2000}, tetraethylene glycol (TEG), and glycerol.

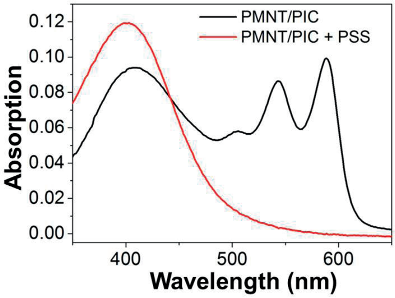

Figure 6.5 UV-vis spectra of the PMNT/PIC mixture in the absence and the presence of PSS. [PSS] = 1.0 µM in repeat units (RUs). [PMNT] = 25.0 µM in repeat units (RUs). PIC = PIC5 with n = 1073 and concentration c = 2.0 mg/mL.

6.2.3 Tuning the photophysical properties of PMNT/PIC with PIC polymer length

In an attempt to tune the assembly and photophysical response of PMNT/PIC complex more readily, a series of different length polymers were employed. **Figure 6.6**a shows UV-vis spectra of PMNT/PIC for different PIC molecular weights, but at identical concentrations, i.e. at the same concentration of repeating units. As the molecular weight goes down, the red shifit signal at 589 nm increases, implying that the conformational changes of PMNT backbone arise from the alterations in the template of host PIC material. Interestingly, both the intensities of absorption and the ratios between $A_{543\ nm}$ and $A_{589\ nm}$ strongly relate to n (**Figure 6.7**). For the longest PIC polymers, the spectrum of PMNT/PIC resembles that of PMNT itself with a broad absorption band at λ_{max} = 410 nm which corresponds to the random-coil conformation, indicating very few interactions between PMNT and the long PIC polymer. For intermediate length PIC scaffolds, the long wavelength absorption progressively increases, but the absorbance ratio $A_{543\ nm}/A_{589\ nm}$ remains small. We tentatively attributed this to the few PMNT polymers that were trapped into host PIC, that stretches and planarizes the thiophene backbone. The band at λ_{max} = 543 nm intensifies with further decreasing the polymer length, which ultimately becomes close to that of PMNT in solid state.[16] This indicates that the formation of PMNT/PIC assemblies with short PIC polymers leads to PMNT main chain aggregation. Furthermore, the fluorescent properties of the PMNT/PIC assemblies were studied as well. As shown in **Figure 6.6**b, the intensity of the two red-shifted fluorescence bands at 598 and 640 nm first rose and then dropped with increasing PIC length, while the band at 520 nm assigned to free PMNT increased continuously. We suggest that the stretching of PMNT polymer gradually increases with decreasing of PIC length (from PIC7 to PIC3), but PMNT polymers intensively form aggregation with the further shortening of PIC (from PIC3 to PIC1). These results support the UV-vis spectra completely: weak interaction with long PIC, a stretched comformation by the intermediate length PIC, and quenching by short PIC due to the aggregation. However, the aggregates of PMNT and PIC are so small that we could not observe them by either atomic force microscopy (AFM) in solid state or by dynamic light scattering (DLS) in solution (data not shown). The full fluorescence spectra of PMNT/PIC as a function of PIC polymer length are given in **Figure 6.8**. In addition, photoluminescence (PL) decay dynamics are dramatically impacted by the changes in chain planarity and coupling efficiency.[37,38] **Table 6.2** shows PL decay constants of PMNT and PMNT/PIC assemblies for different PIC lengths. Interestingly, lifetimes composed of two components (fast and slow) were observed for each assembly. The fraction of the fast one (τ_1) increased gradually with increasing PIC length, whereas the slower contribution (τ_2) decreased until to almost zero. The control experiment, however, shows that PMNT itself only displays the fast relation process in water. It is well-known that this fast component suggests a random conformation and the longer radiative lifetime arises from the aggregation,[37] which agrees markedly well to both the UV-vis and the fluorescence spectra.

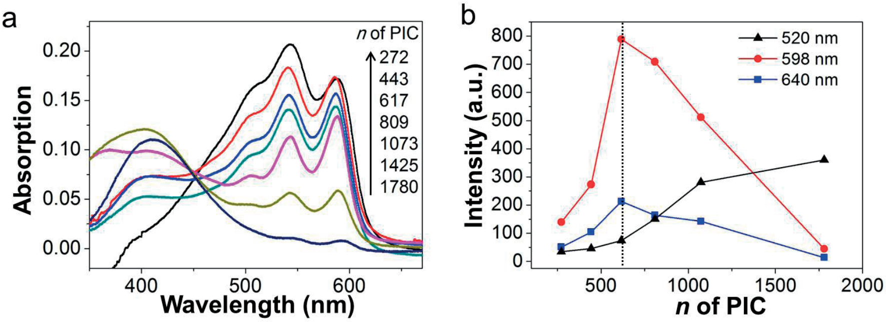

Figure 6.6. (a) UV-vis spectra of PMNT/PIC as a function of degree of polymerization of PIC. (b) Plot of the maximum fluorescence intensity (520, 598 and 640 nm) of PMNT/PIC with different polymer length. [PMNT] = 25.0 µM in repeat units (RUs). [PIC] = 2.0 mg/mL, *n* = 272–1780.

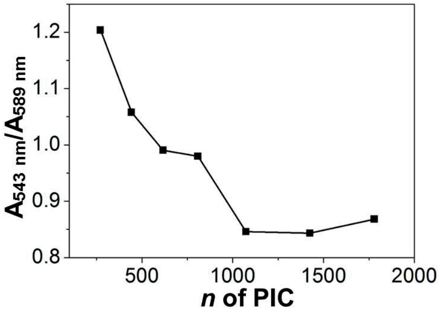

Figure 6.7. Plot of the absorption intensity ratio of $A_{543\,nm}/A_{589\,nm}$ of PMNT/PIC with different polymer length. [PMNT] = 25.0 µM in repeat units (RUs). [PIC] = 2.0 mg/mL, *n* = 272–1780.

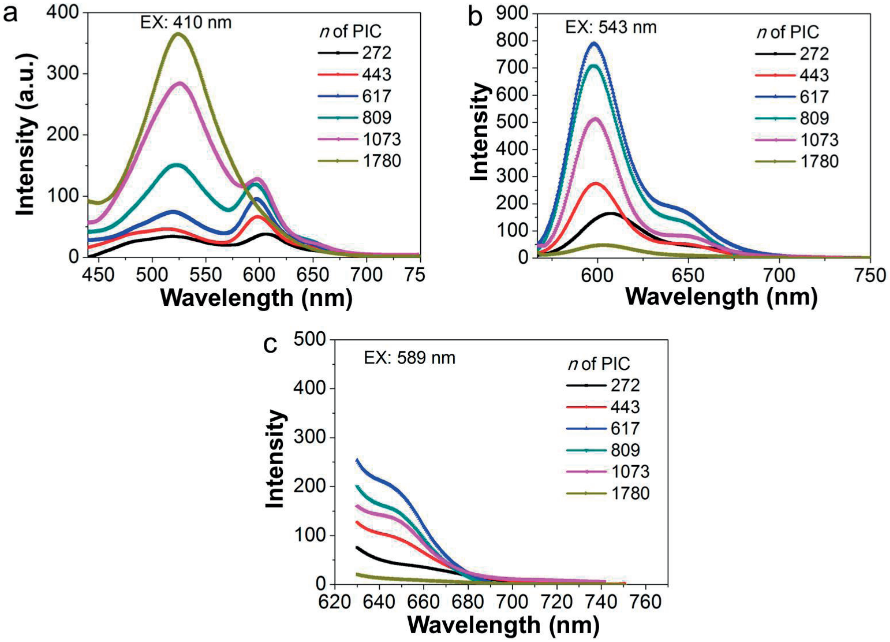

Figure 6.8. Fluorescence spectra of PMNT/PIC as a function of polymer length with different excitation wavelengths (a: 410 nm, b: 543 nm, c: 589 nm). [PMNT] = 25.0 µM in repeat units (RUs). [PIC] = 2.0 mg/mL, *n* = 272–1780.

Table 6.2: PL decay constants of PMNT and assemblies of PMNT/PIC with different length of PIC. [PMNT] = 25.0 µM in repeat units (RUs). [PIC] = 2.0 mg/mL, *n* = 272–1780.

PMNT with different length of PIC	τ (ns)	Rel (%)
PIC1, n = 272	τ_1 0.6262	86.51
	τ_2 1.6550	13.49
PIC2, n = 443	τ_1 0.5988	90.61
	τ_2 1.6561	9.39
PIC3, n = 617	τ_1 0.6329	97.77
	τ_2 2.5382	2.23
PIC4, n = 809	τ_1 0.6067	98.86
	τ_2 2.8417	1.14
PIC5, n = 1073	τ_1 0.5823	99.41
	τ_2 2.2383	0.59
PMNT only (control)	τ_1 0.2967	100
	τ_2 0	0

6.2.4 Mechanism of PMNT/PIC assembly

To better understand the PMNT/PIC assembly mechanism, we performed diffusion NMR which provides information on the molecular dimensions based on the diffusion coefficients. As demonstrated in **Figure 6.9,** the signals at 2.0 ppm were specifically assigned to PMNT, whereas, the signals at 3.5 ppm were attributed to the ethylene glycol side chains of PIC. Fitting the decay curve of the NMR intensity (2.0 ppm), the diffusion coefficient of the PMNT itself in D_2O was determined to be 6.1×10^{-7} cm^2/s (Figure 6.9b). When PMNT was trapped into PIC, however, the diffusion coefficient of the PMNT was 2.2×10^{-7} cm^2/s, which was close to that of PIC, 1.6×10^{-7} cm^2/s (Figure 6.9d). This is a clear indication that the PMNT performs a similar motion as PIC due to the close interaction.

Furthermore, the stoichiometry of the PMNT/PIC assembly was studied by means of continuous variation plots (Job plots) from UV-vis measurements. Interestingly, both the short and long PIC polymers, indeed, showed an interaction between the PMNT and PIC with a rough stoichiometry ratio of 2:1 PMNT:PIC, (**Figure 6.10**). Although the ratio between PMNT and PIC cannot be calculated accurately due to relatively high polydispersity indices (PDI) of the polymers, we can estimate that they are of the same order of magnitude. Circular dichroism (CD) spectroscopy only shows a characteristic Cotton effect at λ = 275 nm of the helical backbones of the PIC (**Figure 6.11**). Considering the facts that no characteristic CD signal of the polythiophene π-π^* transitions was observed, implying that PMNT backbones display an achiral conformation in the assembly of PMNT/PIC. Moreover, PMNT polymers are too big to insert into the groove of PIC with a helical pitch of only 4.6 Å.[26] Therefore, we suggest that PMNT interacts with the poorly organized extremities of the PIC polymer.

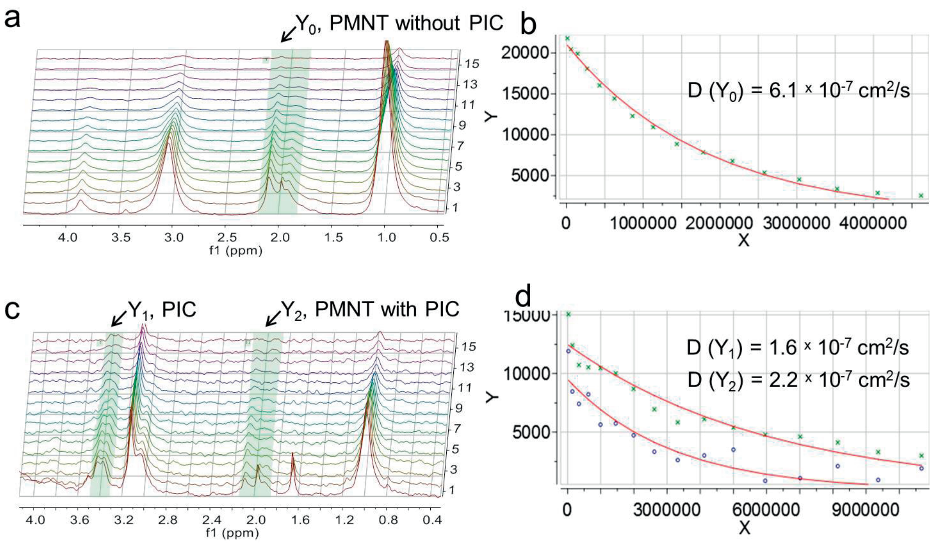

Figure 6.9 (a) Diffusion ^{1}H NMR spectrum of free PMNT (8 kDa, average) in D_2O. (b) Fitting curve of the diffusion coefficient (D) of free PMNT. (c) Diffusion NMR spectrum of PMNT/PIC in D_2O. (d) Fitting curve of the diffusion coefficient of PMNT/PIC. PMNT peaks at around 2.0 ppm, and PIC peaks at around 3.4 ppm were used for analysis. After fitting with the equation (mono-exponential fit, $B + \exp(-xF)$), D(Y_0) is the diffusion coefficient of PMNT; D(Y_1) is the diffusion coefficient of PIC; D(Y_2) is the diffusion coefficient of PMNT trapped in the assembly of PMNT/PIC. To avoid viscosity effects, the shortest PIC polymer (PIC1) was used and all measurements were performed at 5 °C.

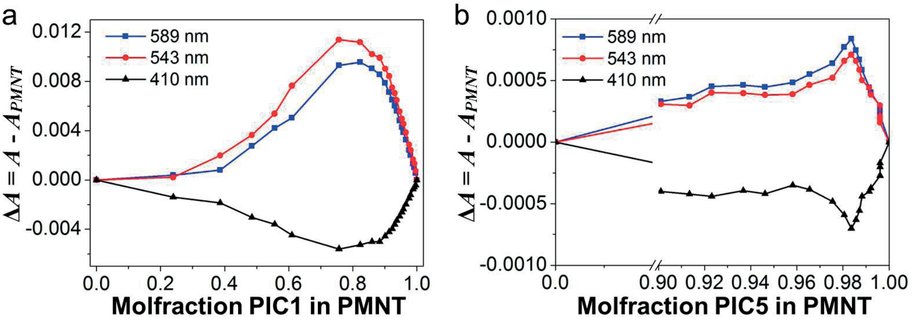

Figure 6.10. Job plot of PMNT and PIC (PIC1: a, PIC5: b) constructed from titration experiments with a constant PMNT concentration $c = 25.0$ μM in repeat units (RUs). The Job plot shows a minimum at the ratio PMNT:PIC roughly around 2:1. Job plots were created from three absorption maxima of the PMNT/PIC spectrum (at λ = 410, 543 and 589 nm).

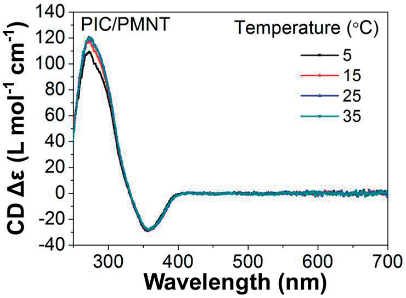

Figure 6.11. CD spectra of PMNT/PIC as a function of temperature. [PMNT] = 25.0 µM in repeat units (RUs). PIC = PIC5 with *n* = 1073 and concentration *c* = 2.0 mg/mL.

As mentioned before, assembly of PMNT/PIC is strongly related to both the concentrations and the polymer lengths of PIC. It is easy to understand the concentration dependence, however, what is the difference in structure between the short and long PIC polymers? To answer this question, powder X-ray diffraction (PXRD) measurements were carried out to obtain more information on the architecture of PIC. The diffraction patterns yield the average diameters of PIC single polymer chain.[27] They slightly decreased from 18.6 to 16.7 Å with increasing polymer length, indicating that the short PIC polymers display a larger helix than the long ones (**Figure 6.12**). The increase in diameters, are tentatively attributed to the high fraction of the poorly organized helical ends of the short polymers. At the same time, the CD signals of PIC decreased with decreasing polymer length, implying that the helical content of short PIC is lower than that of long polymer, which supports the PXRD results (**Figure 6.13a**). In this context, the poorly defined extremities of PIC seem the preferred assembly site for PMNT, resulting in a strong dependence on the polymer length.

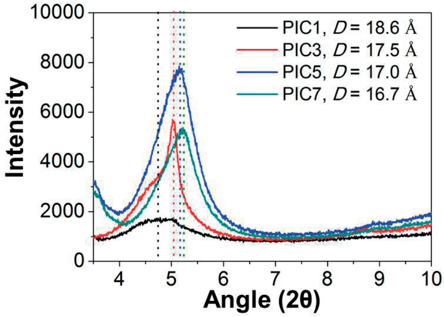

Figure 6.12. PXRD patterns of PIC with different polymer length obtained from a cast film.

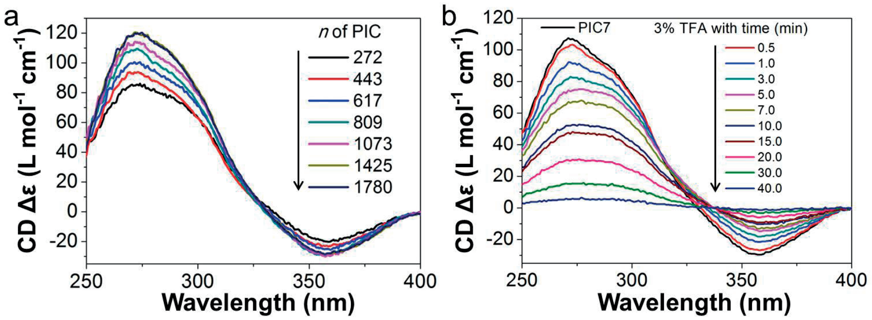

Figure 6.13. (a) CD spectra of PIC as a function of polymer length. (b) CD spectra of PIC7 (PIC = 1780) partly denatured by 3 % TFA as a function of time. Denaturation was carried out in the 3 % TFA in DCM. At the given time, an aliquot was taken from the reaction that was quenched by precipitation. After removal of the solvents, the partly denatured PIC samples were redissolved in H_2O at a 2.0 mg/mL concentration.

Table 6.3. The helix content of PIC with different denaturing time. $\Delta\varepsilon_0$ is the initial CD intensity of PIC7 at 275 nm, and Δε represents the CD intensity at 275 nm at the given denaturing time.

Time (min)	CD Δε at 275 nm	Helix content $\Delta\varepsilon/\Delta\varepsilon_0$ (%)
0	107.512	100
0.5	101.763	94.65269
1	92.0928	85.65816
3	81.5506	75.85256
5	74.3843	69.18697
7	67.1868	62.49237
10	51.989	48.35646
15	47.7713	44.43346
20	30.1719	28.06375
30	15.261	14.19469
40	5.3567	4.982421

In order to further prove the role of the extremities of PIC, the longest polymer (PIC7, *n* = 1780) was partly denatured by trifluoroacetic acid (TFA) to mimic the short polymers through building more “end like” poorly defined sections. We found that the Cotton effect disappeared gradually with time after the addition of 3 % (v/v) TFA (Figure 6.13b). Consequently, a series of long PIC polymers with different helical contents were obtained (**Table 6.3**). As expected, the assembly efficiency of PMNT/PIC dramatically increased with gently decreasing the helical content of long PIC polymer during the inception phase (**Figure 6.14**a). However, the absorption of red-shifted bands sharply decreased again after the helical content reduced below 60 %. We believe that the helical structures of PIC can not be maintained at such low helical content and the backbone no longer serves as a scaffold (Figure 6.14b). Although the fine structure of the less defined extremities of PIC could not be clearly illustrated by microscopy yet, we are in the process of uncovering it by theoretical modeling. This work is beneficial for understanding and designing of more stable helical polymers, since the extremities are commonly the onset point of degradation of the polymer structure.

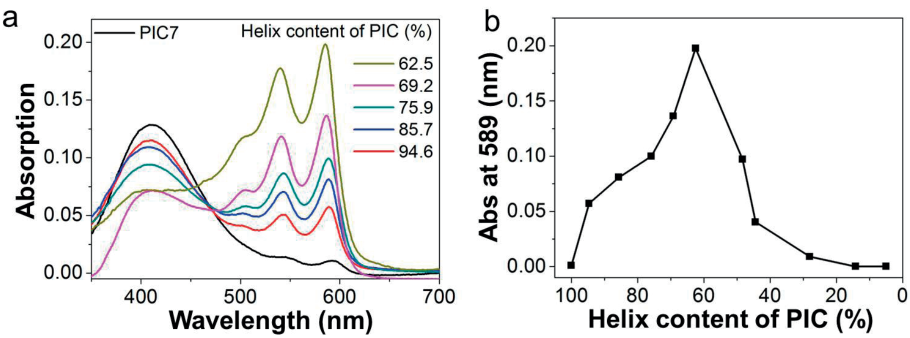

Figure 6.14. (a) UV-vis spectra of the PMNT/PIC with decreasing the helix content of PIC (partly denatured by TFA). (b) Plot of the maximum absorption intensity (589 nm) of PMNT/PIC with decreasing the helix content of PIC. [PMNT] = 25.0 µM in repeat units (RUs). PIC = PIC7 with *n* = 1780 and concentration *c* = 2.0 mg/mL.

6.3 Conclusions

In conclusion, we demonstrated an unusually specific assembly between a helical PIC host and a water-soluble PMNT guest. PIC served as a scaffold to trap and stretch the PMNT chain into a highly ordered conformation. A massive red shift in both the UV-vis and fluorescence spectra were observed, which is attributed to the coplanar polythiophene backbones imparted by stiff and helical PIC. Furthermore, the photophysical properties of PMNT/PIC are easily controlled by concentration and polymer length by virtue of the small structural differences between the long and short polymers. Importantly, the poorly defined extremities of PIC play a crucial role in the assembly, which was experimentally supported by partially denaturing a long PIC polymer. In addition, the PIC/PMNT supermolecular assembly does not infer with the gelation process of the PIC polymer and the mechanical properties in the linear and nonlinear regimes remain unchanged. In short, the complex exhibits promising applications in both semiconductor and biosensor fields to use well-defined helical architectures to initiate and tune the conformation and organization of water soluble conjugated polymers.

6.4 Experimental Section

Materials and Instrumentation

Triethyleneglycol-functionalized polyisocyanodipeptides (PIC) were synthesized and characterized according to the literature.[32] The lengths of the PIC polymers were controlled by different molar ratios of monomer over catalyst (30:1, 100:1, 500:1, 1,000:1, 3,000:1, 5,000:1, 8,000:1). Poly(3-(3′-*N,N,N*-triethylammonium-1′-propyloxy) -4-methyl-2,5-thiophene chloride) (PMNT), was synthesized and characterized following the reported procedures.[34] All chemicals were purchased from Sigma-Aldrich, Acros or Alfa Aesar and used as received unless specially stated. The absorption spectra were taken on a JASCO V-630 UV-Vis spectrophotometer, and the CD spectra were carried out on a JASCO J-810. The fluorescence spectra were carried out on a Hitachi F-4600 fluorimeter equipped with a Xenon lamp excitation source. Diffusion NMR spectra were recorded on Bruker Avance III 500 MHz. The PL decay constants were performed on an Edinburgh Analytical Instruments FLS980 spectrometer, equipped with a supercontinuum ultrafast fiber laser (Fianium). Powder X-ray diffraction (PXRD) measurements were studied on a Bruker D8 Advance X-ray powder diffractometer.

Spectroscopy study for the assembly of PMNT/PIC

To prepare the PIC host materials, 2.0 mg of polymer was dissolved in 1.0 ml of pre-cooled MilliQ water by stirring for 12 h at 4 ºC, resulting in a 2.0 g L^{-1} transparent PIC solution. Next, 5.0 µL of 1.0 mM guest polymer PMNT was added in 200 µL of PIC host samples prepared before. After 1 min of incubation, the UV-vis and fluorescence spectra were measured in 100 µL quartz cuvettes at 5 ºC. The same procedure applies to all polymer lengths.

Partially denaturing of the long PIC polymer

First, 20.0 mg of PIC7 ($n = 1780$) was dissolved in 10.0 ml of DCM and stirred at r.t. Next, 0.3 ml (3 %, v/v) of trifluoroacetic acid (TFA) was added to partiallly denature the PIC with time. The mixture was precipitated in excess isopropyl ether to remove the TFA and the partially denatured PIC polymer was obtained by filtration. The helix content (%) of PIC was determined by the ratio of $\Delta\varepsilon_0$ over $\Delta\varepsilon$. $\Delta\varepsilon_0$ is the initial CD intensity of PIC7 at 275 nm, and $\Delta\varepsilon$ represents the CD intensity of denatured PIC7 at 275 nm with denaturing time.

6.5 References

(1) Baker, C. O.; Huang, X.; Nelson, W.; Kaner, R. B. *Chem. Soc. Rev.* **2017**, *46*, 1510.

(2) Kim, J.; Swager, T. *Nature* **2001**, *411*, 1030.

(3) Zhang, J.; Zhang, Y.; Fang, J.; Lu, K.; Wang, Z.; Ma, W.; Wei, Z. *J. Am. Chem. Soc.* **2015**, *137*, 8176.

(4) Feng, L.; Zhu, C.; Yuan, H.; Liu, L.; Lv, F.; Wang, S. *Chem. Soc. Rev.* **2013**, *42*, 6620.

(5) Jiang, Y.; McNeill, J. *Chem. Rev.* **2016**.

(6) Yuan, H.; Fan, Y.; Xing, C.; Niu, R.; Chai, R.; Zhan, Y.; Qi, J.; An, H.; Xu, J. *Anal. Chem.* **2016**, *88*, 6593.

(7) Wang, B.; Wang, M.; Mikhailovsky, A.; Wang, S.; Bazan, G. C. *Angew. Chem., Int. Edit.* **2017**, *56*, 5031.

(8) Stupp, S. I.; Palmer, L. C. *Chem. Mater.* **2013**, *26*, 507.

(9) Kelly, J. A.; Giese, M.; Shopsowitz, K. E.; Hamad, W. Y.; MacLachlan, M. J. *Acc. Chem. Res.* **2014**, *47*, 1088.

(10) Benelli, T.; Mazzocchetti, L.; Mazzotti, G.; Paris, F.; Salatelli, E.; Giorgini, L. *Dyes Pigm.* **2016**, *126*, 8.

(11) Noriega, R.; Rivnay, J.; Vandewal, K.; Koch, F. P.; Stingelin, N.; Smith, P.; Toney, M. F.; Salleo, A. *Nat. Mater.* **2013**, *12*, 1038.

(12) Clark, J.; Silva, C.; Friend, R. H.; Spano, F. C. *Phys. Rev. Lett.* **2007**, *98*, 206406.

(13) Brustolin, F.; Goldoni, F.; Meijer, E.; Sommerdijk, N. A. *Macromolecules* **2002**, *35*, 1054.

(14) Apperloo, J. J.; Janssen, R. A.; Malenfant, P. R.; Fréchet, J. M. *J. Am. Chem. Soc.* **2001**, *123*, 6916.

(15) Risteen, B. E.; Blake, A.; McBride, M. A.; Rosu, C.; Park, J. O.; Srinivasarao, M.; Russo, P. S.; Reichmanis, E. *Biomacromolecules* **2017**, *18*, 1556.

(16) Li, C.; Numata, M.; Bae, A.-H.; Sakurai, K.; Shinkai, S. *J. Am. Chem. Soc.* **2005**, *127*, 4548.

(17) Cabanetos, C. m.; El Labban, A.; Bartelt, J. A.; Douglas, J. D.; Mateker, W. R.; Fréchet, J. M.; McGehee, M. D.; Beaujuge, P. M. *J. Am. Chem. Soc.* **2013**, *135*, 4656.

(18) Li, Q.; Barrett, D. G.; Messersmith, P. B.; Holten-Andersen, N. *ACS Nano* **2016**, *10*, 1317.

(19) Zhang, C.; Mcadams, D. A.; Grunlan, J. C. *Adv. Mater.* **2016**, *28*, 6292.

(20) Schwartz, E.; Koepf, M.; Kitto, H. J.; Nolte, R. J.; Rowan, A. E. *Polym. Chem.* **2011**, *2*, 33.

(21) Yashima, E.; Ousaka, N.; Taura, D.; Shimomura, K.; Ikai, T.; Maeda, K. *Chem. Rev.* **2016**, *116*, 13752.

(22) Maeda, K.; Wakasone, S.; Shimomura, K.; Ikai, T.; Kanoh, S. *Macromolecules* **2014**, *47*, 6540.

(23) Ihara, E. In *Encyclopedia of Polymeric Nanomaterials*; Kobayashi, S., Müllen, K., Eds.; Springer Berlin Heidelberg: Berlin, Heidelberg, 2015, 1851.

(24) Lifson, S.; Andreola, C.; Peterson, N.; Green, M. *J. Am. Chem. Soc.* **1989**, *111*, 8850.

(25) Millich, F.; Baker, G. K. *Macromolecules* **1969**, *2*, 122.

(26) Cornelissen, J. J.; Donners, J. J.; de Gelder, R.; Graswinckel, W. S.; Metselaar, G. A.; Rowan, A. E.; Sommerdijk, N. A.; Nolte, R. J. *Science* **2001**, *293*, 676.

(27) Cornelissen, J. J.; Graswinckel, W. S.; Rowan, A. E.; Sommerdijk, N. A.; Nolte, R. J. *J. Polym. Sci., Part A: Polym. Chem.* **2003**, *41*, 1725.

(28) van Buul, A. M.; Schwartz, E.; Brocorens, P.; Koepf, M.; Beljonne, D.; Maan, J. C.; Christianen, P. C.; Kouwer, P. H.; Nolte, R. J.; Engelkamp, H. *Chem. Sci.* **2013**, *4*, 2357.

(29) Jaspers, M.; Dennison, M.; Mabesoone, M. F.; MacKintosh, F. C.; Rowan, A. E.; Kouwer, P. H. *Nat. Commun.* **2014**, *5*.

(30) Jaspers, M.; Pape, A.; Voets, I. K.; Rowan, A. E.; Portale, G.; Kouwer, P. H. *Biomacromolecules* **2016**, *17*, 2642.

(31) Kouwer, P. H.; Koepf, M.; Le Sage, V. A.; Jaspers, M.; van Buul, A. M.; Eksteen-Akeroyd, Z. H.; Woltinge, T.; Schwartz, E.; Kitto, H. J.; Hoogenboom, R. *Nature* **2013**, *493*, 651.

(32) Koepf, M.; Kitto, H. J.; Schwartz, E.; Kouwer, P. H.; Nolte, R. J.; Rowan, A. E. *Eur. Polym. J.* **2013**, *49*, 1510.

(33) Mandal, S.; Eksteen-Akeroyd, Z. H.; Jacobs, M. J.; Hammink, R.; Koepf, M.; Lambeck, A. J.; van Hest, J. C.; Wilson, C. J.; Blank, K.; Figdor, C. G. *Chem. Sci.* **2013**, *4*, 4168.

(34) Ho, H. A.; Boissinot, M.; Bergeron, M. G.; Corbeil, G.; Dore, K.; Boudreau, D.; Leclerc, M. *Angew. Chem., Int. Edit.* **2002**, *41*, 1548.

(35) Tang, Y.; Feng, F.; He, F.; Wang, S.; Li, Y.; Zhu, D. *J. Am. Chem. Soc.* **2006**, *128*, 14972.

(36) Langeveld-Voss, B.; Janssen, R.; Meijer, E. *J. Mol. Struct.* **2000**, *521*, 285.

(37) Niles, E. T.; Roehling, J. D.; Yamagata, H.; Wise, A. J.; Spano, F. C.; Moulé, A. J.; Grey, J. K. *J. Phys. Chem. Lett.* **2012**, *3*, 259.

(38) Baghgar, M.; Labastide, J. A.; Bokel, F.; Hayward, R. C.; Barnes, M. D. *J. Phys. Chem. C* **2014**, *118*, 2229.

CHAPTER 7

SUMMARY AND PERSPECTIVE

7.1 Summary

Since the concept of signal amplification of conjugated polymers, known as the molecular wire effect, was firstly proposed by Swager in 1995, many groups have spent much attention on the design of optical sensors and photovoltaic devices based on the unique optoelectronic properties of CPs. In comparison to small molecule counterparts, the excitation energy along the whole backbone of CPs transferring to lower energy acceptor sites over long distances results in an amplified fluorescence signal. The readily decorated side chains offer the possibility of water solubility and many other functions to the CPs. As a consequence, water-soluble conjugated polymers (WCPs) have aroused scientists' great interest in biosensing, imaging, disease diagnosis and therapy. This thesis covers the efforts to fabricate composite materials and explore their potential applications in sensory technology based on water-soluble conjugated polymers.

In **Chaper 1**, we disscused and highligted recent advances and design principles in the biosensing from small molecules to biomacromolecules, detection of bacteria and antimicrobial applications of WCPs. In comparison to traditional methods, these strategies are sensitive, quick, simple, and do not need sophisticated instruments. Generally, signal transduction of water-soluble conjugated polymers are attributed to electron transfer, fluorescence resonance energy transfer (FRET) and analyte-induced aggregation or conformtional changes of the WCPs based on specific interactions including electrostatic attraction, π-π stacking, van der Waals forces, and hydrophobic effects, which are introduced by the side chains. These examples illustrate that water-soluble conjugated polymers are promising for highly sensitive biosensors, imaging and disease diagnostics, and will be incorporated into routine characterization protocols in molecular biology laboratories.

In **Chapter 2**, we showed a strategy for visualized detection of the conformation changes of calmodulin bound to target peptide (CaM-M13) by using a cationic polythiophene derivative (PMNT). Micrometer-sized supramolecular PMNT/CaM-M13 complexes were formed by strong electrostatic interactions, in which the PMNT backbone coiled around CaM and transformed from a random coil conformation to a more nonplanar and less conjugated conformation, exhibiting a blue-shifted absorption and emission wavelength. Upon addition of Ca^{2+} ions, the conformation of CaM-M13 changed from a closed form to a compact form of Ca^{2+}/CaM-M13, which induced the PMNT to return to its random-coil conformation. Because of the specific binding of Ca^{2+}, the assembly of PMNT/CaM-M13 can be applied to sense calcium as well. However, the PMNT-based assay was only sensitive to the hybrid CaM-M13 protein, and also exhibited high background signal arising from nonspecific interactions.

In order to obtain a platform with the ability for sensing all conformational changes of CaM and with a high signal to noise ratio, we explored hybrid materials composed of graphene-oxide (GO) and a conjugated polymer in a FRET-based approach in **Chapter 3**.

The conformational changes of CaM were quantitatively monitored through the FRET ratio between the conjugated poly(fluorene-*co*-phenylene) (PFP) and the enhanced green fluorescent protein (EGFP) at the N-terminus of CaM. Upon binding with Ca^{2+}, CaM/Ca^{2+} was strongly absorbed on the surface of GO, accounting for the stronger hydrophobic interactions and the weaker electrostatic repulsion compared to CaM in the absence of Ca^{2+}. This resulted in much farther distance between PFP and EGFP, and thus a much weaker FRET efficiency. Due to the efficient fluorescence quenching effect of GO and the noncovalent interaction with biomolecules, this platform can be applied not only for calmodulin but also for calmodulin binding to target peptides which imitate the transformations *in vivo*.

Chapter 4 described a hybrid probe for the "turn-on" detection of carbon dioxide (CO_2) based on a guanidinium-pendent oligofluorene (G-OF) and a water-soluble conjugated polythiophene (PTP). In this system, both the guanidinium groups of G-OF and the carboxylate moieties of PTP were CO_2 responsive, which reversibly dictates the assembly between PTP and G-OF. Upon exposure to CO_2, the electrostatic repulsion between G-OF and PTP can be effectively enhanced through protonation of the side chains, leading to the disaggregation and thus the "turn-on" fluorescence. The strategy allowed for a light-up visible detection of CO_2 with high sensitivity. Importantly, this system was capable of sensitively monitoring the concentration changes of CO_2 in a photosynthesis process.

Carbonic anhydrase (CA)-functionalized materials have been used for CO_2 sequestration by applying its high biocatalytic activity. Inspired by these studies, we demonstrated in **Chapter 5** the CO_2-responsive assembly and CO_2-sequestration of PTP catalyzed by the enzyme carbonic anhydrase, combining the signal amplifcation properties of PTP and the efficient catalytic activity of CA. The latter catalyzes the inter-conversion between CO_2 and HCO_3^-, and as such, controls the assembly of PTP by changing the electrostatic and hydrophobic interactions of neighboring PTP molecules, resulting in visible fluorescence changes. Furthermore, the carboxylate side chains of PTP coordinated with Ca^{2+} to form the chelate of PTP/Ca^{2+}, which can be employed for biomimetic CO_2 sequestration with fluorescence monitoring.

In **Chapter 6**, a helical polyisocyanide (PIC) was employed to stretch the backbone of the polythiophene derivative (PMNT). PMNT was trapped and stretched into a coplanar conformation by the extremities of the PIC chains to form the PMNT/PIC assembly through the strong hydrophobic interactions between the helical core and the polythiophene backbone, along with the electrostatic interactions between the cationic side chains of PMNT and the ethylene glycol of PIC. Complex formation resulted in a tremendous red shift in both UV-vis and fluorescence spectra. Interestingly, the poorly defined extremities of PIC backbone were primarily involed in the PMNT/PIC assembly, which was supported by the partially denaturing the PIC polymers. Moreover, the degree of stretching and aggregation of PMNT were easily tuned by the length of PIC, taking advantage of the small structural differences between long and short polymers.

7.2 Perspective

"We live in a materials-limited world," said by Alan G. MacDiarmid. Most, if not all, technologies are limited by the available materials. Any new advanced functional materials will arouse a profound revolution on technologies and our daily life. As demonstrated in Chapter 1, water-soluble conjugated polymers (WCPs) have been widely applied for miscellaneous emerging technologies such as sensing molecules ranging from small chemical molecules to biomacromolecules, detection of bacteria and antimicrobial applications, cell imaging, disease diagnosis and therapy. They combine their excellent light harvesting, signal amplification, unique optoelectronic properties, good water solubility and biocompatibility.

Although many applications of conjugated polymers have been explored extensively in the past decades, there are still some problems and challenges that should be addressed. For the design and synthesis of materials, most of currently reported conjugated polymers require complicated and long preparation procedures. And hence, materials are not always easily produced in bulk quantities. Developing a modular design to functionalize the plain polymer backbone will be much easier for commercialization. In addition, tuning the polymer backbone with higher quantum yields and narrow-band emission/NIR emissions is also in urgent need, especially for the polymers used in in-depth biological systems (cell or animal).

Inspired by the studies reported in this thesis, we hope to continue exploring the existing knowledge for multifunction systems based on conjugated polymers. In Chapter 2 and 3, we demonstrated two different strategies to detect the conformational changes of calmodulin (CaM). One is based on the flexible polymer backbone of polythiophene and the Ca^{2+}-controllable electrostatic interactions between PMNT and CaM. The second is a hybrid material composed of graphene oxide (GO) and poly(fluorene-*co*-phenylene) (PFP) for detection of the conformation transition of CaM by using a FRET technique. Like the others, however, it should be noted that most of these assays only work with purified samples or *in vitro* with few other components; nonspecific interactions between WCPs and various ingredients in blood and cells remain a big problem to be resolved. Therefore, improving the sensitivity and selectivity in complex environments will boost the real application *in vitro* and *in vivo* by optimization of chemical structures and the optical properties of WCPs. Taking advantage of ROS generation properties of WCPs, we speculate that WCPs can exhibit multiple functions in more sophisticated and more in-depth biological systems, which integrate with selective sensing, efficient imaging, high tissue penetration, diagnosis with high accuracy, and therapy with fewer side effects. There is still a good potential for WCPs-based approaches to be incorporated into routine biological assay protocols. Looking ahead, it is exciting that we can monitor our health in real time by using non-invasion approaches. So, we anticipate that wearable sensors based on conjugated polymers will be explored in the near future.

Optical sensors play an ever-increasing role in environmental monitoring, security, industrial safety control and so on. In Chapter 4 and 5, we explored the applications of conjugated polymers in detection and sequestration of CO_2. The polymers used in this works are functionalized with CO_2 responsive groups, for example, guanidinium, carboxylate and tertiary amines that react with CO_2, resulting in the changing of net electric charge of polymers. Subsequently, the optical signals are generated due to different assembly process way of the polymers. Beyoud what has been described in this thesis, polarity or viscosity changes can be used to induce and regulate of hydrophobicity and π-π stacking between conjugated main chains, which manipulates the aggregation state or the conformation of CPs, resulting in varying intrachain and interchain energy transfer efficiency or color changes in solution. In addition, intelligent responsive materials and fluorescent chemosensors will be developed by using the aggregation-induced fluorescence resonance energy transfer (FRET) strategy.

Chapter 6 described an unusual strategy for tuning the conformation of polythiophene derivative (PMNT) in nanoaggregates state. PMNT is trapped and stretched into the extremities of polyisocyanopeptides (PIC) to form a PMNT/PIC assembly with a strong optical signature. Meanwhile, the gelation properties of PIC including linear and nonlinear regimes remain unaffected. It would be interesting to study whether the polythiophene backbone can be further stretched by stressed PIC polymers when the external force is applied on PMNT/PIC gels where PMNT effectively acts as a force sensor. Furthermore, the relative red-shifted property of PMNT shows promising bioapplications for antibacterial and anticancer purposes.

Acknowledgements

“精诚所至，金石为开”是四年多的博士学习对科研以及生活最深刻的体会。2013年秋，带着对科研的憧憬选择了读博，与大多数人一样，博士生活是枯燥无味的，每天都有做不完的实验、看不完的文献；但也是充实快乐的，一个好的实验结果、一篇论文都足以让我开心很久。2015年，幸运地作为一名联合培养博士研究生来到荷兰奈梅亨（Nijmegen） Radboud大学。在这里，新的课题、文化差异以及语言障碍使我学会了独立与合作；良好的科研氛围、悠闲的生活节奏使我由最初的无感到慢慢地喜欢上这里，喜欢上这个小镇Nijmegen。博士论文付梓之际，我能够顺利完成学业离不开导师、同学、朋友和家人的支持和帮助，心里对他们充满了感激之情，在这里，我衷心地向他们表示感谢。

首先感谢我的导师展永教授（Prof. Yong Zhan），展老师品德高尚、思维活跃，从他身上我受到很多启发。展老师授予我的不仅是如何做科研，更重要的是如何做人，他总是教育我“做学问要先学会做人”，这些都让我以后受用不尽。展老师为人随和热情，治学严谨细心，对工作精益求精，对师生尽职尽责。清晰地记得他为我一字一句的斟酌修改稿件，也清晰记得他为卓老师作的那首祝寿诗，这些深深地打动了我。千言万语汇成一句话，衷心地感谢展老师对我的帮助，如果没有他的支持，我博士可能不会这么顺利地完成！另外，感谢于慧老师在生活上对我的关心，有时她还关心一下我的胖瘦，让我觉得特别亲切，她和蔼可亲的师长风范、孜孜不倦的工作精神让我终生难忘！

感谢执行导师邢成芬教授（Prof. Chengfen Xing），很荣幸在我博士的开始能遇上邢老师，是她把我带入了科研。邢老师知识渊博、学术思维活跃、治学态度严谨，对科研充满热情，有着忘我的工作精神。之前，我对共轭聚合物这一领域知之甚少，在对这个新兴的交叉领域充满好奇的同时也倍感压力。在邢老师的悉心指导下，完成了博士工作的选题、设计和实施，并在该过程中学到了许多做科研的理论知识和实验技能，在分析问题、解决问题等能力都得到了很大提升。在此，谨向邢老师致以衷心的感谢！此外，感谢徐加良副教授，徐老师为人友善，对科研有执着的追求以及自己独特的想法，感谢徐老师在我初到荷兰时对我生活和课题上的热心帮助！

I wish to thank both of my supervisors Prof. dr. Alan E. Rowan and Dr. Paul H. J. Kouwer at Radboud University. Thank you very much for giving me the opportunity to pursue my PhD study in your group. Here, I learnt the amazing world about strain-stiffening hydrogels. Alan, you are always full of ideas when we have meetings, your passion for scientific research created an inspiring working atmosphere. I wish you all the best in Australia. Paul, you are so kind and friendly, you always encourage my pursuits and give me a great space in allowing me to develop myself. I clearly remember that you accompanied with me to go to Amsterdam and had the meeting with Prof. Huib Bakker at AMOLF. On the train, it was probably our first long conversation which impressed me a lot. I knew you eat fruits everyday supervised by your dietician, your lovely wife. You did help me a lot during my PhD in Nijmegen. Thank you again! I hope we can be just as much in touch in the future.

Great thanks to the members of reading committee, Prof. dr. Roeland J. M. Nolte, Prof. dr. Johan Hofkens (KU Leuven) and Prof. dr. Qing Ji (Hebei University of Technology) for the evaluation of this thesis. I would like to express my admiration and appreciation to Prof. Nolte again, thanks for your valuable suggestions during our group meeting.

感谢聚合物小分队的齐俊杰副教授、柴燃、牛瑞民、范一冰、孟凡凡、严文敏、李瑞华、赵林飞、王波、郭靖琦等全体成员同甘共苦、一起奋斗的实验室生活，谢谢你们给予我的鼓励和帮助！感谢柴燃在许多事情上的帮助，祝你科研一切顺利！感谢生物物理研究所的安海龙教授、纪青教授、赵同军教授、王永宏教授、张素花教授、陈娅斐副教授、柳辉副教授、耿金鹏副教授、李军委副教授、韩英荣副教授、曹天光副研究员、庞春丽副教授、袁常青副教授、任树喜老师、张玉红老师等老师们的支持和帮助！感谢李谨博士、李多芳博士、王徐朝、郭帅、莫莉等同学的关心和帮助！

感谢中科院化学所有机固体实验室王树研究员在课题上的建议和帮助！

Next, I would like to thank all the group members during the second part of my PhD in Nijmegen: Joan, Pim, Maarten, Daniël, Paula, Kaizheng (开政), Zhaobao (召宝), Ying (张英), Hans, Onno, Emilia, Kathleen, Noel, Sarah, Vincent, Martin, Kim, Erik, Roel and Tom. Joan, thank you for your kind helps with column chromatography and PIC synthesis at that super embarrassed moment. Paula, thank you for the Feijoada, it’s really nice. Bao, we are brother with happiness and sadness, you always happily take side person. Ying, thanks for teaching me the basic chemical knowledge. Kaizheng, cut the crap, thanks, man. I wish you all the best in all your current PhD study and future business endeavors.

Of course, I also want to thank all the people from Wing 8 where I worked: Yongjun (永军), Yingfeng (盈锋), Fei (彭飞), Wei (李巍), Jiawei (家维), Shauni, Jelle, Moti, Toni, Loai, Marlies, Alaa, Serena, Denise, Maria, Niels, Guo and all others. Thanks for the great working atmosphere. In addition, I wish to thank the other colleagues from the Institute for Molecular and Materials (IMM): Hui (赵辉), Min (包敏), Jing (谢静), Nannan (楠楠), Lifei (立飞), Yulong (玉龙), Yali (雅丽), Henan (鹤楠), Abbas, Dion, Petri, Arjan, Bob, Shaji and all others. 感谢每次帮我剪头发的曲洁琼(Jieqiong)，留学生活培训了大厨，也造就了理发师！

I would like to thank the people who I collaborated with them. For the imaging of PIC polymers, I want to thanks Roel Hammink in RIMLS, you helped me a lot and always gave me some useful advice. From the AMOLF in Amsterdam, I would like to thank Eliane, Giulia, Dr. Yves and Prof. Huib for your professional knowledge on FTIR & 2D-IR fields. In addition, I wish to thank Susana at University of Leuven for the high resolution imaging. Hope we can do more and keep in touch in the future.

I also owe many thanks to Paula Willems, thank you a lot for the daily matters, you did me a big favor for my tax problem. Great thanks to Peter, you are so kind and humorous, I did enjoy very much your funny jokes and enthusiasm, thank you a lot for all your help in ordering, repairing, posting etc… I want to thank Paul, thanks for your professional suggestions and helps in NMR measurements.

感谢好友崔瑞飞，很高兴能有你这样的朋友，谢谢你特别是最后一段时间的照顾，祝你家宝宝茁壮成长！感谢边子健，让我了解更多足球，Liverpool, you will never walk along! 感谢刘荣兵，谢谢你经常带我们去德国，祝你在ABN Bank工作顺利！

感谢我的父母和家人，感谢你们从小到大对我的无私关爱和默默支持！你们辛苦了一辈子，以后要多为自己着想，祝你们健康幸福！

感谢我的未婚妻张瑶，谢谢你从本科、硕士、一直到博士的陪伴！你发来的每一个表情，我看着那都是你，一样的调皮、可爱，让我感觉暖暖的。有一幅画“总有一个傻瓜无条件对你好”。我想说你我都是彼此的傻瓜！ Forever！

Hongbo Yuan
袁宏博
2017秋
Nijmegen

Curriculum Vitae

Hongbo Yuan was born on the 10th of July 1988 in Henan province, China. After finishing high school at Huixian in 2006, he moved to Tianjin to study Biotechnology, and he obtained his Master's degree from the School of Science, Hebei University of Technology in 2013. He then started as a PhD student in School of Materials Science and Engineering under the supervision of Prof. dr. Yong Zhan and Prof. dr. Chengfen Xing at the same university. While pursuing his PhD, he moved to Nijmegen in 2015 as a joint PhD student in the Molecular Materials group under the supervision of Prof. dr. Alan E. Rowan and Dr. Paul H. J. Kouwer at Radboud University, The Netherlands. During his PhD, he focused on the fabrication of hybrid materials and studied their applications based on water-soluble conjugated polymers. The results of this research are described in this thesis.

List of Publications

1. **Yuan, H.;** Xing, C.; Zhan, Y.; Kouwer, P.; Rowan, A., Stretching the Conformation of Polythiophene by a Helical Polyisocyanide Polymer. *Manuscript in preparation*
2. **Yuan, H.;** Xu, J.; Dam, E.; Giubertoni, G.; Rezus, Y.; Hammink, R.; Bakker, H.; Zhan, Y.; Rowan, A.; Xing, C.; Kouwer, P., Strategies to Increase the Thermal Stability of Truly Biomimetic Hydrogels: Combining Hydrophobicity and Directed Hydrogen Bonding. *Macromolecules* **2017**, *Accepted*
3. **Yuan, H.**; Xing, C.; Fan, Y.; Chai, R.; Niu, R.; Zhan, Y.; Peng, F.; Qi, J., Carbon Dioxide-Controlled Assembly of Water-Soluble Conjugated Polymers Catalyzed by Carbonic Anhydrase. *Macromol. Rapid Commun.* **2017,** *38* (5) DOI: 10.1002/marc.201600726
4. **Yuan, H.**;* Fan, Y.;* Xing, C.; Niu, R.; Chai, R.; Zhan, Y.; Qi, J.; An, H.; Xu, J., Conjugated Polymer-Based Hybrid Materials for Turn-On Detection of CO2 in Plant Photosynthesis. *Anal. Chem.* **2016,** *88* (12), 6593-6597.
5. **Yuan, H.**; Qi, J.; Xing, C.; An, H.; Niu, R.; Zhan, Y.; Fan, Y.; Yan, W.; Li, R.; Wang, B., Wang, S., Graphene-Oxide-Conjugated Polymer Hybrid Materials for Calmodulin Sensing by Using FRET Strategy. *Adv. Funct. Mater.* **2015,** *25* (28), 4412-4418. (Back cover)
6. **Yuan, H.**; Xing, C.; An, H.; Niu, R.; Li, R.; Yan, W.; Zhan, Y., Ca^{2+}-Controlled Assembly for Visualized Detection of Conformation Changes of Calmodulin. *ACS Appl. Mater. Interfaces* **2014,** *6* (17), 14790-14794.
7. Fan, Y.; Xing, C.; **Yuan, H.**; Chai, R.; Zhao, L.; Zhan, Y., A Conjugated Polyelectrolyte-Based New Strategy for In Situ Detection of Carbon Dioxide. *ACS Appl. Mater. Interfaces* **2017**. DOI: 10.1021/acsami.7b05410
8. Chai, R.; Xing, C.; Qi, J.; Fan, Y.; **Yuan, H.**; Niu, R.; Zhan, Y.; Xu, J., Water-Soluble Conjugated Polymers for the Detection and Inhibition of Protein Aggregation. *Adv. Funct. Mater.* **2016,** *26* (48), 9026-9031.
9. Yan, W.; **Yuan, H.**; Li, R.; Fan, Y.; Zhan, Y.; Qi, J.; An, H.; Niu, R.; Li, G.; Xing, C., Conjugated Polythiophene/Porphyrin Complex for Rapid and Simple Detection of Bacteria in Drinking Water. *Macromol. Chem. Phys.* **2015,** *216* (15), 1603-1608.
10. Li, R.; Niu, R.; Qi, J.; **Yuan, H.**; Fan, Y.; An, H.; Yan, W.; Li, H.; Zhan, Y.; Xing, C., Conjugated Polythiophene for Rapid, Simple, and High-throughput Screening of Antimicrobial Photosensitizers. *ACS Appl. Mater. Interfaces* **2015,** *7* (27), 14569-14572.
11. Xing, C.; **Yuan, H.**; Xu, S.; An, H.; Niu, R.; Zhan, Y., Nucleobase-Functionalized Conjugated Polymer for Detection of Copper (II). *ACS Appl. Mater. Interfaces* **2014,** *6* (12), 9601-9607.

Patents

1. Xing, C.; **Yuan, H.**; Zhan, Y.; An, H.; Qi, J., Method for Detecting Carbon Dioxide Content or Carbon Dioxide Conversion Through Conjugated Polymers Based on Stimulus Response, CN 104865233A [P]. **2015**.
2. Zhan, Y.; Xing, C.; **Yuan, H.**; An, H.; Li, R.; Niu, R., Biomacromolecule Conformation Change Detecting Method Based on Graphene Oxide and Conjugated Polymer Composite Material, CN 104749148A [P]. **2015**.
3. Xing, C.; Niu, R.; Li, R.; Qi, J.; Zhan, Y.; **Yuan, H.**; An, H., Method for High-Throughput Screening of Photosensitizers, CN104862373A [P]. **2015**.